Friedrich-Alexander-Universität
Naturwissenschaftliche Fakultät

Master's Thesis
in Physics

A Decade of air shower detection with LORA: Integration into NuRadioReco and evaluating the performance stability

Stuti Sharma

Supervisor: Prof. Dr. Anna Nelles

Erlangen Centre for Astroparticle Physics

Submission date: 01-10-25

Acknowledgements

First and foremost, I would like to thank my supervisor, **Prof. Dr. Anna Nelles** for her continuous guidance, support, and encouragement throughout my journey. Her expertise, patience, and constructive feedback were crucial in my progress. I also appreciate the opportunities she provided to me, which helped me gain valuable experience and expand my professional network.

I would also like to thank the members of my group **Karen, Sjoerd, and Philipp** at the Erlangen Centre for Astroparticle Physics (ECAP) for their support, helpful discussions, and for providing the tools and guidance essential to this research. I am also grateful to **Dr. K.B. Mulrey** and **Lucas** from Radboud University for their valuable input. In addition, I would like to thank **Dr. Satyendra Thoudam** whose PhD thesis formed a key foundation for my work.

A heartfelt thank you goes to my friends and colleagues for their continued motivation, companionship, and perspective during the ups and downs of this journey.

Finally, I am deeply grateful to my family for their unwavering love, support, and belief in me. Without their encouragement, this achievement would not have been possible.

Declaration of Originality

I, Stuti Sharma, student registration number: 23271671, hereby confirm that I completed the submitted work independently and without the unauthorized assistance of third parties and without the use of undisclosed and, in particular, unauthorized aids. This work has not been previously submitted in its current form or in a similar form to any other examination authorities and has not been accepted as part of an examination by any other examination authority.

Where the wording has been taken from other people's work or ideas, this has been properly acknowledged and referenced. This also applies to drawings, sketches, diagrams and sources from the Internet.

In particular, I am aware that the use of artificial intelligence is forbidden unless its use an aid has been expressly permitted by the examiner. This applies in particular to chatbots (especially ChatGPT) and such programs in general that can complete the tasks of the examination or parts thereof on my behalf.

Any infringements of the above rules constitute fraud or attempted fraud and shall lead to the examination being graded "fail" ("nicht bestanden").

Erlangen, 03.09.2025	*Stuti Sharma*
Place, Date	Signature

Abstract

This thesis investigates the long-term stability of the LOfar Radboud Air Shower Array (LORA), a network of ground based particle detectors essential for triggering and calibrating cosmic-ray detection with LOFAR (Low-Frequency Array). These detectors are distributed across northern Europe, with a dense core in the Netherlands.

To support this analysis, a streamlined data pipeline was developed to integrate more than a decade (2011–2021) of ground-particle measurements into the NuRadioReco framework. The pipeline converts raw ROOT files into unified *.nur* files for efficient processing. The analysis investigates the stability of the LORA detectors for long-term performance monitoring over the period 2011–2021.

The LORA mean energy spectrum lies 20–50% above the Pierre Auger reference with its 5–95% uncertainty band. Within the 150 m fiducial circle, the mean detection efficiency increased from approximately 0.44 to 0.63 after applying quality cuts, indicating improved and more uniform coverage over time. Additionally, the coefficient of variation (CV) of daily trigger rates for individual detectors between 2011 and 2021 remains stable for most of the detectors, indicating only minor year-to-year fluctuations and stable long-term performance.

Overall, the results confirm LORA's effectiveness as a reliable hybrid trigger and calibration system for LOFAR's cosmic-ray program, and support its continued role in upcoming developments such as LOFAR2.0.

Contents

1 Introduction

1.1 Overview

This thesis presents a study of cosmic ray detection and analysis using the LOfar Radboud Air Shower Array (LORA). LORA is a network of plastic scintillator detectors integrated with the Low-Frequency Array (LOFAR) radio telescope.

Cosmic rays are high energy particles originating from space. Understanding their properties provides crucial insight into astrophysical phenomena. When these rays enter Earth's atmosphere they initiate extensive air showers (EAS) composed of secondary particles, which can be studied using detector arrays like LORA [1].

1.2 Scope of This Thesis

A primary goal of this thesis, lies a unified framework described in Section 4.2 for handling and analysing LORA data within the NuRadioReco (NRR) framework [2]. Chapter 4 describes how ROOT format files, once cumbersome to deal with are converted and validated against LOFAR's existing radio pipelines.

This effort simplifies data access and ensures that future studies can easily reproduce and use the results. With the dataset ready, Chapter 5 examines detector performance from 2011 to 2021.

This analysis is important because stable, long-term detector performance is crucial in astroparticle physics. The last detailed studies of LORA's detectors were done over ten years ago. The stability of the detectors has not been investigated since then. By examining data from the past eleven years, this work updates the array's reliability. This is key for confirming past results and building trust in future measurements using LORA data.

Looking ahead, this thesis opens up several directions for future research [3]. A main goal is to use the new NuRadioReco pipeline to combine LOFAR's radio data with LORA's particle measurements allowing for more accurate reconstruction of cosmic ray composition and energy.

Furthermore, the methods developed here can be applied to other cosmic ray detector arrays, supporting a more unified and consistent analysis approach across different experiments in astroparticle physics. Finally, a systematic stability monitoring program drawing on the tools and best practices outlined in this work can ensure that LORA remains a reliable component of LOFAR's cosmic ray studies. This work will also prepare the array for the enhanced capabilities of the LOFAR2.0 upgrade and future projects like the Square Kilometre Array (SKA) [4], in the years to come.

1.3 Thesis Structure

The remainder of this thesis is organized as follows:

- **Chapter 2** introduces the physics of cosmic rays, including their sources, composition, and the mechanisms behind extensive air showers. It also presents the cosmic ray energy spectrum and its key spectral features such as the Knee, Ankle, and GZK cutoff. Additionally, it introduces important reconstruction tools like the Nishimura–Kamata–Greisen (NKG) function, whose parameters are important to the analysis in this thesis.
- **Chapter 3** introduces the concept of Cosmic Ray Key Science Projects. The chapter further discusses detection methods, focusing on ground based arrays and the specific setup and functionality of the LORA scintillator array. This includes its role in triggering and calibration of LOFAR's radio observations.
- **Chapter 4** discusses the data pipeline, from the raw ROOT files to processed formats using the NuRadioReco framework. It highlights how LORA's particle detector data is structured, processed, and integrated with the radio pipeline.
- **Chapter 5** presents the main analysis. This includes LORA detector stability over time, event reconstruction criteria, energy calibration, differential flux measurement, and comparison to reference benchmarks such as the Pierre Auger Observatory data.
- **Chapter 6** concludes with a discussion of the results, current pipeline limitations, and suggestions to improve data processing, detector reliability, and long-term monitoring.
- **Appendix A** provides a list of tables used throughout the thesis, offering a quick reference for key numerical results and calibration summaries.
- **Appendix B** contains supplementary plots and additional visualizations that support the core analysis but are too detailed for the main text.

2 Physics of Cosmic Rays

2.1 What is Cosmic Radiation?

High energy charged particles that come from outer space and move close to the speed of light are referred to as cosmic radiation or cosmic rays. These particles originate from a range of astrophysical sources. At low energies, cosmic rays mainly come from the Sun and from supernova explosions in our Galaxy [1]. At higher energies, the sources are uncertain but likely extragalactic. These can be possibly linked to active galactic nuclei, gamma-ray bursts, or other energetic cosmic events [5]. The majority of cosmic rays are protons and heavier nuclei. Although electrons and other subatomic particles also contribute [1].

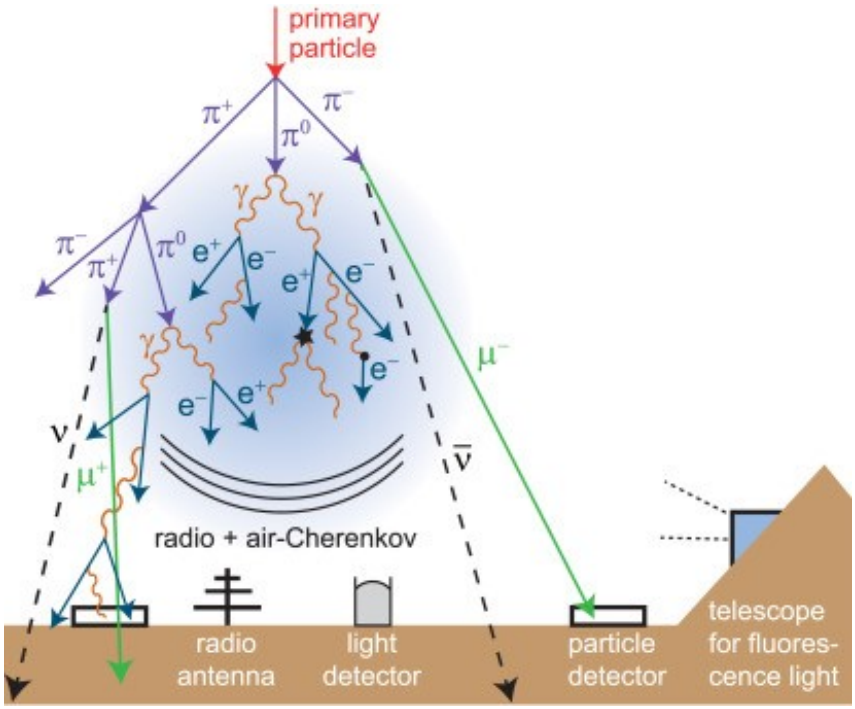

Figure 2.1: Schematic of an extensive air shower triggered by a high energy cosmic ray. Secondary particles are detected by ground based instruments: radio antennas, light detectors, particle detectors and fluorescence telescopes. These complementary techniques enable precise reconstruction of the primary particle's energy, direction, and core position [6].

2.2 Constituents of Cosmic Radiation

Cosmic rays are generally classified into two categories: Primary and Secondary.

Primary Cosmic Rays are those that originate directly from astrophysical sources. These include protons (constituting about 74%), helium nuclei, and heavier atomic nuclei such as carbon, oxygen, and iron [7]. This composition is well constrained at low energies, but at higher energies the proton fraction and overall composition are less certain. These particles are thought to be accelerated by processes such as supernova shock waves, magnetic reconnection events, and other extreme astrophysical environments.

Secondary cosmic rays are produced when primary cosmic rays interact with matter or radiation fields as they travel through the Galaxy or intergalactic space [8]. When a cosmic-ray particle enters the Earth's atmosphere, it is called the *primary particle* of an extensive air shower (EAS) [9]. This incoming particle collides with nuclei in the air and produces many new *secondary particles*. Most of these are pions and kaons, which quickly decay into muons, electrons, neutrinos, and photons as shown in figure 2.1. Together these particles form the air shower that reaches the ground.

2.3 Extensive Air Showers and Their Components

Extensive air showers (EAS) are large cascades of secondary particles produced when high energy cosmic rays interact with atoms in the Earth's atmosphere. These showers are crucial for detecting cosmic rays indirectly, since the primary particles don't reach the ground [10].

Ground based detector arrays such as LOFAR (radio antennas) and LORA (particle detectors), observe the secondary particles described above to study the properties of the original cosmic rays. This is achieved by recording the arrival times and densities of secondary particles at multiple detector stations on the ground [11]. The spatial and temporal patterns of these signals allow reconstruction of the primary cosmic ray's direction, core position, and energy. In addition to radio antennas and particle detectors like those used in LOFAR and LORA, modern observatories include a variety of complementary ground based instruments, as illustrated in figure 2.1.

EAS can be broadly divided into three components [10]:

- **Electromagnetic Component:** This component is produced from the decay of neutral pions ($\pi^0 \rightarrow 2\gamma$), producing high energy photons that initiate electromagnetic cascades. This component consists mainly of electrons, positrons, and photons that propagate through the atmosphere via the mechanisms of bremsstrahlung and pair production. In

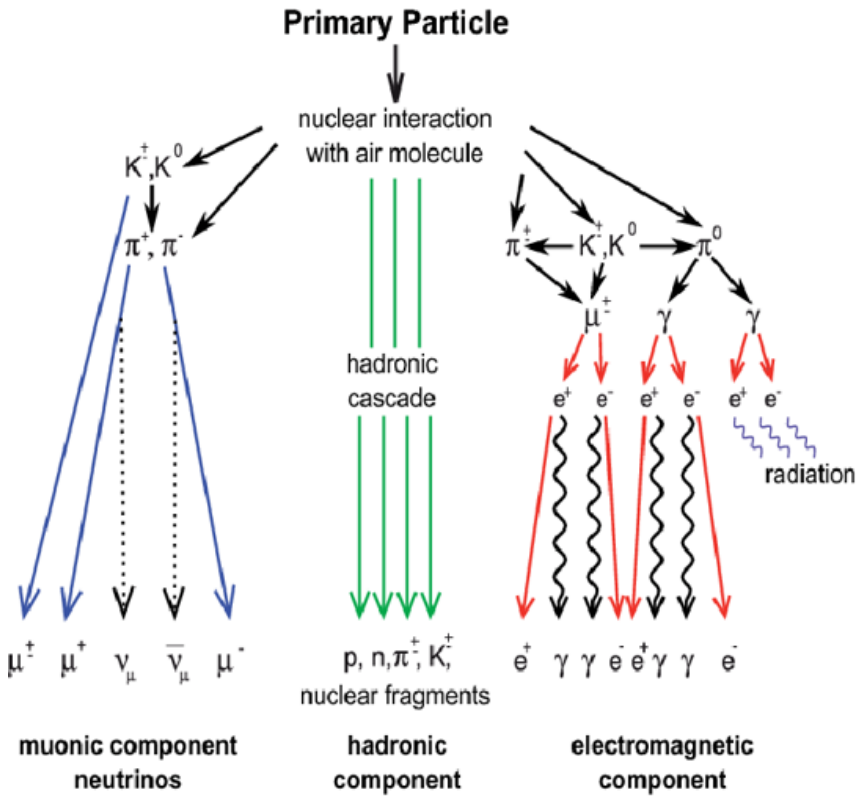

Figure 2.2: Schematic view of the hadronic, muonic, and electron components of an EAS[13].

bremsstrahlung, high energy electrons or positrons are deflected by the electric fields of atomic nuclei, emitting photons as a result of their deceleration.

These high energy photons pass through the electromagnetic field of a nucleus and can produce an electron-positron pair if their energy is greater than 1.022 MeV[12]. The newly created charged particles then emit more photons through bremsstrahlung, repeating the process and creating a cascade of particles as seen in figure 2.2. This cycle continues until the energies of the secondary particles fall below the critical threshold at which point energy losses due to ionization become dominant and the shower gradually attenuates.

- **Hadronic Component:** These come from charged pions decaying into muons (μ) and neutrinos (ν). Muons can travel far before decaying, while neutrinos escape and carry away energy, influencing the shower's particle composition. Charged pions can also interact further to sustain the cascade.
- **Muonic Component:** Produced primarily by the decay of charged pions and kaons ($\pi^{\pm}/K^{\pm} \rightarrow \mu^{\pm} + \nu_{\mu}$). Muons can travel long distances and often reach the ground.

Building on these concepts, this thesis focuses on a set of key parameters used to reconstruct the properties of extensive air showers. This ultimately enables the reconstruction of the cosmic ray energy spectrum from LORA's experimental data. These properties include:

- **NKG function:** The Nishimura–Kamata–Greisen (NKG) function describes the lateral distribution of charged particles in an extensive air shower. It characterizes how the particle density decreases with distance from the shower axis reflecting the spread of the shower as it develops through the atmosphere. This function is given as [14]:

$$\rho(r) = N_{\mathrm{ch}}\, C_s \left(\frac{r}{r_m}\right)^{s-2} \left(1 + \frac{r}{r_m}\right)^{-(4.5-s)} , \tag{2.1}$$

  with the normalization constant

$$C_s = \frac{\Gamma(4.5 - s)}{2\pi\, r_m^2\, \Gamma(s)\, \Gamma(4.5 - 2s)} , \tag{2.2}$$

  where r is the distance from the shower axis, s the age parameter, and r_m the Molière radius. The age parameter quantifies the developmental stage of the air shower. Lower s values indicates a younger, more compact cascade and higher s values a later, more spread out shower. The age parameter is fixed to 1.7 in the work of this thesis to represent a stable shower stage beyond its maximum development. This simplifies the analysis by reducing uncertainties in the lateral distribution fit.

- $\boldsymbol{r_m}$: The Molière radius defines the typical width of the electromagnetic part of the air shower.

- $\boldsymbol{N_{\mathrm{ch}}}$: The shower size, i.e. the total number of charged particles at ground level. This is the primary observable in LORA and serves as the proxy for the cosmic-ray energy.

- **Zenith angle $\boldsymbol{\theta}$**: The angle between the shower axis and the vertical.It determines how deep the shower travels through the atmosphere, influencing particle densities at the ground and how well detectors can observe it (see equation (5.6)).

For this thesis, the emphasis is not on modeling individual particle processes in the shower but on using the data collected from such showers to perform a long-term stability analysis of the LORA detector array and to construct the cosmic ray energy spectrum. Knowing the basic structure of air showers helps to understand the particle densities and observed arrival times, which are key to the reconstruction and analysis methods used in this work.

2.4 The Cosmic Ray Energy Spectrum

The discovery of cosmic rays was a key moment in astrophysics, starting with Victor Hess's balloon experiments in 1912 [15]. By carrying electrometers to high altitudes (5 km), Hess observed that ionizing radiation increased with altitude. This was contrary to the expectation if the radiation originated only from Earth. This was the first clear proof that cosmic rays come from outside Earth and started a century of advancing experiments which finally led to detailed energy spectrum measurements shown in figure 2.3.

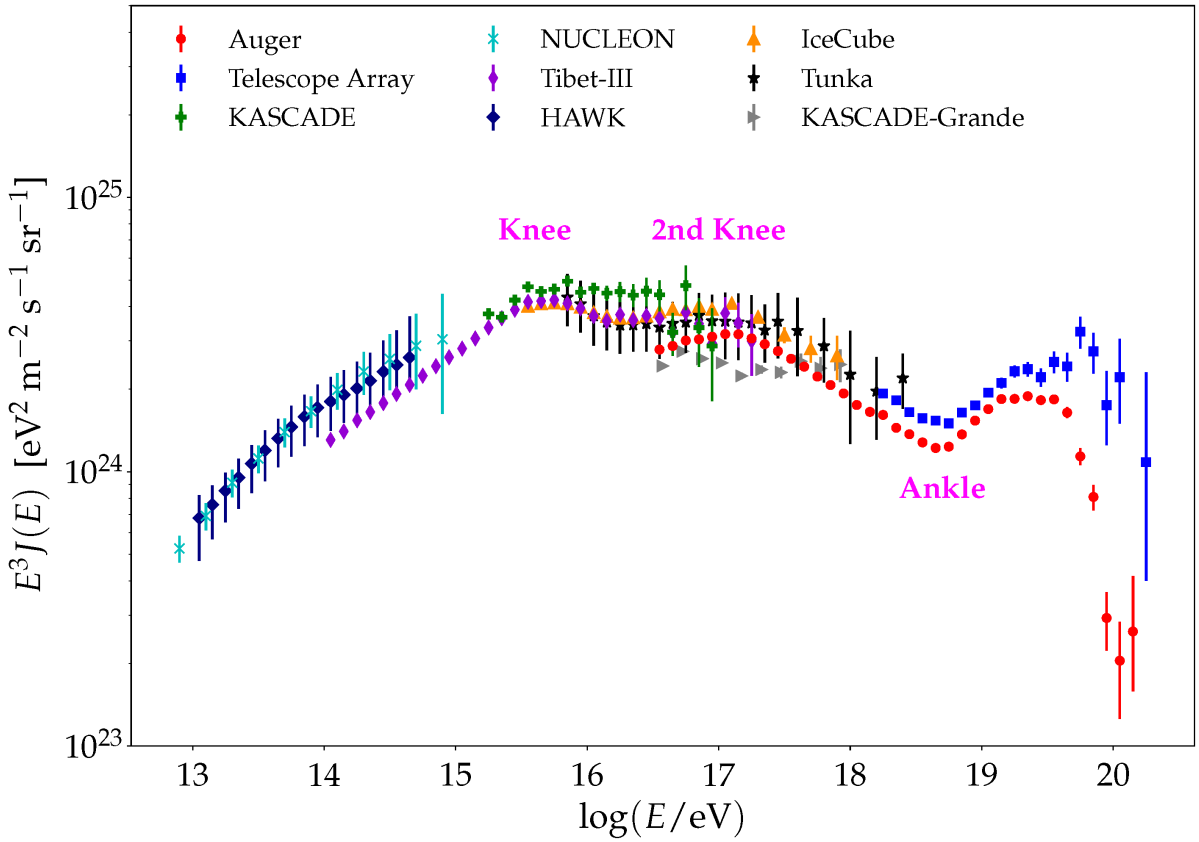

Figure 2.3: Compilation of cosmic ray energy spectrum measurements from various experiments. The plot shows $E^3J(E)$ vs. log(E/eV) from a wide range of detectors: Auger [16], Telescope Array [17], KASCADE [18], NUCLEON [19], Tibet-III [20], HAWK [21], IceCube [22], Tunka [23], and KASCADE-Grande [24]. Distinct spectral features such as the *Knee*, *2nd Knee*, and *Ankle* are labeled. Figure taken from "Determination of the Cosmic-Ray Chemical Composition: Open Issues and Prospects" [25]. The code used to generate the plot is by C. Evoli [26].

A helpful tool in understanding cosmic rays is the *cosmic ray energy spectrum* which displays the flux of cosmic rays as a function of their energy [27]. When plotted in the form $E^3J(E)$ (as in figure 2.3), the spectrum reveals several key features [28]:

- **The Knee** (10^{15} eV): A sudden drop in the spectrum, usually seen as the limit of how much supernova remnants and other Galactic sources can accelerate particles.
- **The Second Knee** (10^{17} eV): Possibly associated with a transition in the composition of cosmic rays from lighter to heavier nuclei.
- **The Ankle** (10^{18} eV): A flattening of the spectrum is often associated with the transition from Galactic to extragalactic sources.
- **The Cutoff** ($10^{19.5}$–10^{20} eV): A suppression in flux, potentially caused by the Greisen–Zatsepin–Kuzmin (GZK) effect. This effect is a result of ultra high energy cosmic rays interacting with the photons of the cosmic microwave background.

These spectral features illustrate the important transition from Galactic to Extragalactic cosmic rays. The highest energy particles observed reach energies far beyond the capabilities of the Large Hadron Collider (LHC) at CERN [29], implying that they are accelerated by extremely powerful astrophysical sources which remain largely mysterious.

Measurements by LOFAR in the transition region around 10^{17} eV indicate that below this threshold most cosmic rays originate within our own galaxy, while above it their origin is predominantly extragalactic. The LORA energy spectrum which will be discussed further in this thesis, spans approximately 10^{16} to 10^{18} eV. It provides critical coverage of the sub-ankle region allowing us to probe the Galactic component with high precision. By combining observations from multiple experiments, we can precisely determine the sources and acceleration mechanisms responsible for these ultra high energy cosmic rays. While these spectral interpretations provide essential astrophysical context, the primary aim of this thesis is to assess the long-term stability and performance of the LORA detector system itself.

3 Detection of Cosmic Rays

3.1 Cosmic Rays Key Science Project

The LOFAR (Low Frequency Array) telescope is one of the largest low frequency radio observatories in the world. It is designed and constructed by ASTRON, the Netherlands Institute for Radio Astronomy [30].

Key Science Projects (KSPs) are scientific initiatives that both guide and benefit from LOFAR's technical development. Each KSP brings together a team of scientists collaborating closely with ASTRON to ensure that LOFAR's design and capabilities meet their demanding scientific objectives. LOFAR is used for various Key Science Projects: Ultra High Energy Cosmic Rays, Cosmic Magnetism of the Nearby Universe, Epoch of Reionisation (EoR), Solar Physics, Deep Extragalactic Surveys, and Transients and Pulsars [30].

One of LOFAR's six flagship KSPs is the *Ultra High Energy Cosmic Rays*. Its primary goal is to explore the origin and composition of high energy cosmic rays by detecting the radio emission generated when these particles produce extensive air showers (EAS) in the Earth's atmosphere.

Unlike traditional techniques, LOFAR provides high resolution radio measurements of these showers by using hundreds of antennas operating in the 10–240 MHz range [31]. This allows to reconstruct properties such as the shower direction, energy, and mass composition with high precision.

3.2 The Role of Ground Based Detectors

Ground based detectors play a crucial role in cosmic ray research because the Earth's atmosphere interact with primary cosmic rays. As the flux decreases significantly with energy of ultra high energy cosmic rays, direct detection via satellites or balloon borne experiments is not feasible. Instead, ground based observatories observe the EAS that form when cosmic rays interact with the atmosphere.

The radio emission from EAS primarily arises from two physical mechanisms: the *geomagnetic effect* and the *Askaryan effect* (charge excess) [32]. The dominant contribution comes from the geomagnetic effect where charged particles in the air shower are deflected by the Earth's magnetic field. This induces a transverse current that emits coherent radio waves. This emission is linearly polarized in the direction of the Lorentz force ($\vec{v} \times \vec{B}$), where $\vec{v}$ is the shower axis and $\vec{B}$ is the geomagnetic field.

The Askaryan effect provides a secondary contribution and is caused by a charge excess in the shower front due to the knock out of electrons from air molecules. This creates a changing net negative charge which gives off coherent radio waves. Together, both of these effects produce a distinct radio pattern on the ground which LOFAR can detect in detail with its dense antenna grid and wide bandwidth.

While radio telescopes like LOFAR detect radio signals from air showers alongside other observations, ground based particle detectors like LORA add important supporting data. Their main role is to trigger the radio detectors since triggering only on radio signals is difficult because of many background sources. Particle detector signals are much clearer. These particle detectors measure the arrival time, lateral particle distribution, and particle content at the ground level, helping to calibrate the transient buffer of the radio observations.

3.3 The LOFAR Radio Telescope

The Low Frequency Array (LOFAR), [33] is a digital radio interferometer spread across multiple countries in northern Europe, with its dense core in the Netherlands as seen in figure 3.1.

Figure 3.1: The Low Frequency Array (LOFAR) Superterp near Exloo, Netherlands.[30]

Each LOFAR station includes arrays of low-band antennas (LBAs, 10–90 MHz) and high-band antennas (HBAs, 110–240 MHz) [31]. The central area, known as the *Superterp* hosts a high density of antennas providing fine spatial resolution that is crucial for cosmic-ray detection. The LBAs are particularly well suited for detecting the short, coherent radio pulses produced by extensive air showers. Thus they are used as the primary instrument. Although a broader frequency band would generally be preferable, LBA data are used because HBA observations are currently beamformed and not yet suitable for analysis.

What makes LOFAR unique for is its ability to perform cosmic-ray observations in parallel with astronomical observations. This is made possible by the use of *Transient Buffer Boards* (TBBs) which constantly record data and can be read out when LORA triggers an event. These boards save short bursts of raw radio signals from many antennas, keeping detailed timing information. This process is vital to precisely reconstructing air showers.

Due to its dense antenna layout in the Superterp and wide frequency range, LOFAR offers higher spatial resolution than earlier cosmic-ray radio detectors. This enables detailed checks of emission models for each event and precise measurements of shower geometry and primary energy.

3.4 LORA: A scintillator array for LOFAR

This thesis focuses on the LOfar Radboud Air Shower Array (LORA), a particle detector array situated at the Superterp and extended beyond the dense core as part of an upgrade to the LOFAR radio telescope. Both the LOFAR and LORA stations are plotted in figure 3.2. Station coordinate data were obtained from JSON configuration files provided within NuRadioReco which will be discussed in detail in Section 4.2.[1] LORA plays a crucial role in hybrid cosmic ray detection as it:

- acts as the triggering system for LOFAR's radio readout by identifying extensive air shower events in real time and initiating storage of raw radio data from the antennas,
- provides essential air shower parameters within nanosecond precision including the arrival direction, core position, and lateral particle density distribution on the ground.

These parameters are critical for reconstructing the geometry and energy of the primary cosmic ray and for cross validating the radio based measurements. In particular, LORA's particle data helps identify the shower's axis and size which are crucial to understanding the radio signal. Combining both measurements allows for accurate event-by-event comparisons and makes composition sensitive results more reliable in hybrid analyses.

[1] NuRadioReco is a reconstruction framework for radio detectors of high energy neutrinos and cosmic rays.

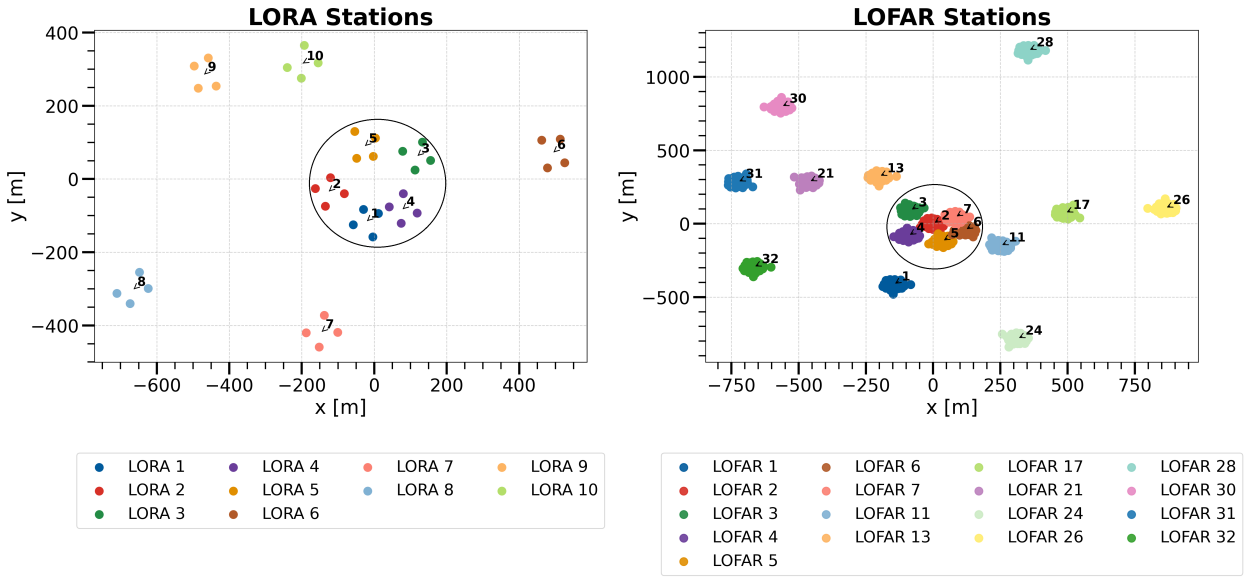

Figure 3.2: Left: Configuration of the 40 LORA detectors grouped into 10 stations, each consisting of 4 detectors. The central black circle in both panels indicates the location of the Superterp.
Right: Layout of the LOFAR stations.

3.4.1 Layout and Experimental Design of LORA

LORA consists of 20 plastic scintillation detectors arranged over a circular area of approximately 320 meters in diameter. These detectors are grouped into five sub-arrays, each containing four scintillators as shown in figure 3.3 connected to local electronics and a GPS synchronized clock system. Each scintillator unit comprises two sheets of NE114 plastic scintillator coupled to photomultiplier tubes (PMTs) via wavelength shifter bars. These are enclosed in weatherproof housing. The detector signals are digitized at a 2.5 ns time resolution and time-stamped with approximately 10 ns precision [34].

LORA is designed to detect extensive air showers (EAS) induced by primary cosmic rays with energies above 10^{16} eV. It records full signal traces (2 µs pre-trigger and 8 µs post-trigger), along with energy deposition and arrival times for each triggered detector. A typical coincidence trigger condition requires 3 out of 4 detectors in a sub-array to fire within a 400–500 ns window, resulting in an array wide trigger rate of about 0.15 Hz [35].

3.4.2 Role of LORA in LOFAR's Readout System

LORA functions as a ground based particle detector that triggers LOFAR's transient buffer boards (TBBs) to store raw radio data corresponding to cosmic-ray events. This enables time synchronized hybrid measurements.

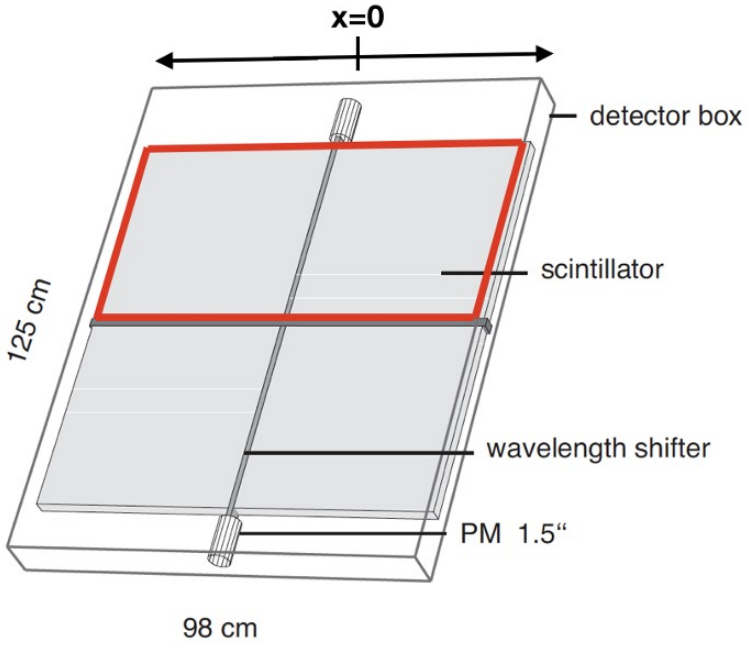

Figure 3.3: Schematic diagram of the LORA scintillators. A single PMT detects light from two panels connected via a wavelength shifter which is highlighted in red [34].

While LOFAR reconstructs the radio footprint, LORA provides key shower parameters such as the arrival direction, core location, and lateral particle distribution. These measurements are essential for validating emission models and improving composition analyses through radio-particle correlation studies [35]. Since only the radio data is currently available in NuRadioReco, this thesis advances the goal of a comprehensive analysis by adding the particle data to NuRadioReco.

3.4.3 LORA Expansion and Improved Triggering

To increase the number and quality of detected events, particularly for showers above 10^{17} eV, LORA underwent a major expansion in 2019. Twenty additional scintillators were added to the array which effectively doubled the array size from 20 to 40 detectors, thus increasing the trigger area. This extension resulted in a 45% increase in usable high energy events with strong radio signals [34]. Moreover, the expansion reduced trigger bias that depends on particle type by making it easier to detect showers from heavier particles like iron, especially at inclined angles.

The upgrade also advanced systematic calibration efforts. These include [34]:

- Muon response characterization using dedicated detectors at the Karlsruhe Institute of Technology (KIT)
- Geant4-based simulations of spatial signal dependence in each scintillator

- Assessment of signal reflection effects in coaxial cables to refine the trigger and energy reconstruction algorithms

Such efforts aim to reduce uncertainties in the energy scale and ensure long-term stability of the detector response.

3.4.4 Toward Data Usability and Analysis

A main goal of this thesis is to make LORA data easier to access and use for long-term studies. Although the next chapter covers the new data processing pipeline in detail, it's important to note here that LORA's raw ROOT formatted output data makes smooth analysis difficult.

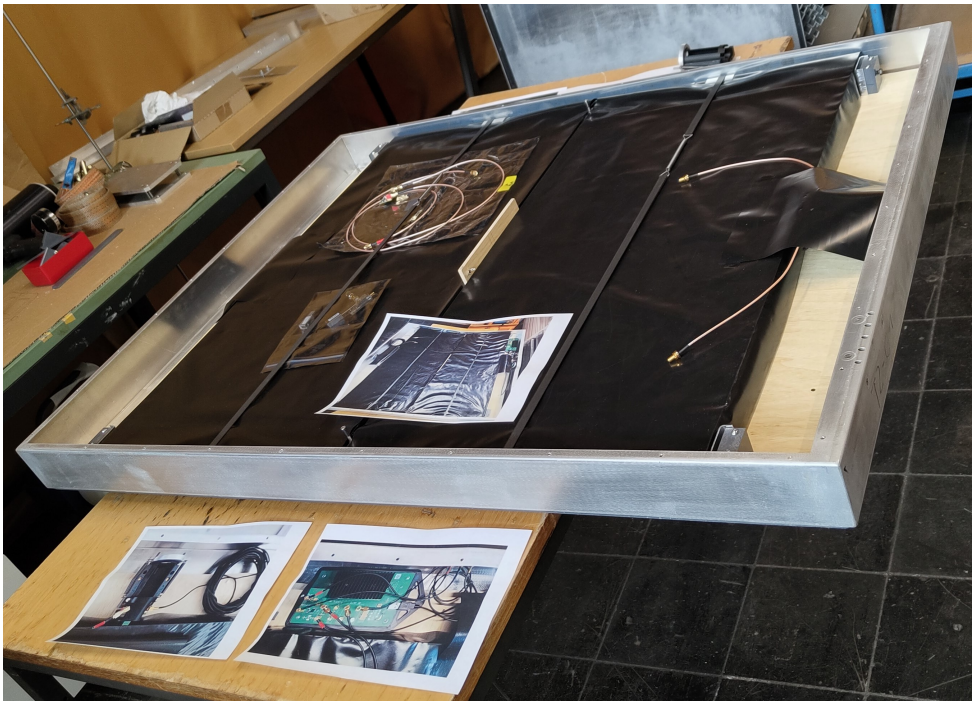

Figure 3.4: Photograph taken at the Karlsruhe Institute of Technology (KIT), Germany. It shows a plastic scintillator module originally used in the KASCADE-Grande experiment [24]. These scintillators have been repurposed for use in current projects such as LORA (LOfar Radboud Air shower array). They are also intended for future applications, such as the Muon Tower component of the Square Kilometre Array (SKA), which will be the world's largest radio telescope [4].

To address this, the next chapter introduces the integration of LORA data into the *NuRadioReco* framework, originally developed for radio reconstruction as a key step toward enabling multiyear hybrid studies. This integration lets LORA's particle data be processed using the same system as LOFAR's radio data, helping with energy spectrum reconstruction and long-term detector monitoring.

4 Data Pipeline

4.1 Raw Data - ROOT files

The raw data for LORA (LOFAR Radboud Air Shower Array) is stored in **ROOT** files which is a widely used data format in high energy astroparticle physics. ROOT is an object oriented data analysis framework developed at CERN to handle large volumes of complex data produced by particle physics experiments. It allows for efficient data storage, complex hierarchical structures (trees and branches), and fast input/output operations [36].

These files contain structured trees representing the detector output and event-level metadata, with branches storing variables such as detector IDs, GPS timestamps, signal amplitudes, and trigger information. The flexibility of ROOT's tree structure enables easy access to both event-level and detector-level information. The raw ROOT data can be accessed on the COMA01 cluster using SSH [37].

In this thesis, all ROOT file processing and data extraction have been performed using *Python*, via the *PyROOT* and *uproot* libraries. The analysis environment was set up using *conda*, which allows for the installation of ROOT and its Python bindings in a way that is modular and reproducible. The structure of the LORA ROOT files evolved over time, with a significant format change introduced in 2020 with additional 20 detectors. The subsections below describe the old and new formats in detail and a visual representation of both the structures is shown in figure B.3.

4.1.1 Old ROOT structure - 2011 to 2019

It is important to note that each ROOT file contains multiple trees and a lot of metadata beyond what is required for this specific analysis. As shown in figure 4.1, trees like *Tree_sec*, *Tree_log*, and *Tree_noise* are also present in the ROOT files but are not used in this work. The focus of this thesis is limited to the information necessary for event reconstruction and detector-level analysis, primarily GPS timestamps and basic trigger related parameters. While only a subset of the available branches and trees is discussed here, the ROOT files offer much more data that could be valuable for further studies such as detector performance characterization, calibration, or noise analysis.

For data collected between 2011 and 2019, the ROOT files used the **Tree_event** structure. In this format, each detector had its own branch (e.g., *Det1*, *Det2*, ..., *DetX*)[1]. These branches stored detector-specific parameters, the most important being the GPS timestamp, available as *DetX.GPS_time_stamp*. This structure is *detector-centric*, meaning the event-level data is reconstructed by reading individual detector branches. A visual representation of **Tree_event** structure can be seen in figure B.1 and it's key characteristics include:

- Tree: **Tree_event**
- Per-detector branches: *Det1*, *Det2*, ..., *Det20*, each representing one scintillator detector in the LORA array.
- Each *DetX* branch contains multiple sub-branches, typically including:
  - *GPS_time_stamp*, the local timestamp for each detector, which is primarily used in this analysis.
  - Other detector-specific parameters such as energy deposition, thresholds, and trigger status (depending on the configuration).
- Accessing data requires looping through each detector branch (*Det1* to *Det20*) individually, making the structure verbose but clear. .

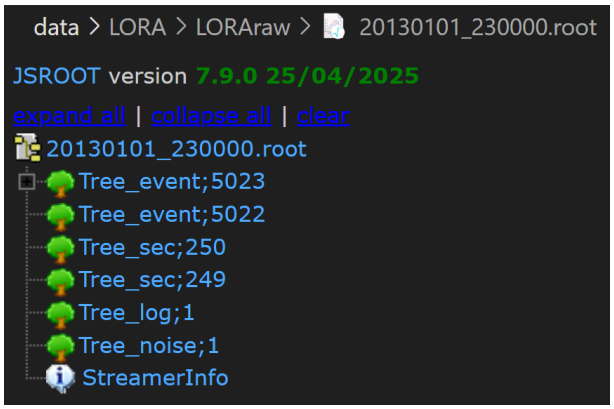

Figure 4.1: LORA ROOT file from 2013 as seen in JSROOT, showing various trees including *Tree_event*, *Tree_sec*, *Tree_log*, and *Tree_noise*. Only selected parts of the data are used in this analysis [38].

4.1.2 New ROOT structure - 2020 to 2021

In the new ROOT structure used from 2020 onwards (figure 4.2), detector-level information is no longer stored in separate branches like *Det1*, *Det2*, etc.

[1] where *X* ranges from *1-20*

Instead, the data is organized per event in a more flexible format within the **Tree_Event** tree. Each event contains arrays (or vectors) of detector-related values, such as *Detector*, *Charge_Corrected*, *Peak_Height_Raw*, and *Channel_Passed_Threshold* among others as seen in figure B.2.

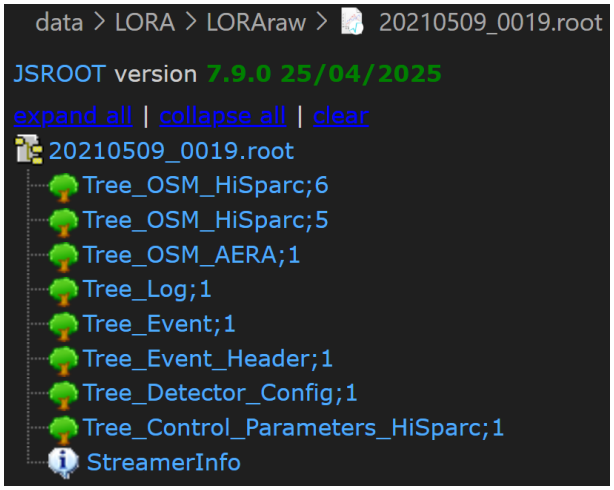

Figure 4.2: Overview of the new ROOT file structure used for LORA data from 2020 onwards. The data is split across multiple trees providing a more modular and hierarchical organization. Each tree contains specific categories of metadata, detector readouts, or event-level parameters.The data used for this thesis is solely extracted from **Tree_Event** [38].

To extract data for each detector, the analysis code goes through the arrays stored in the ROOT file and matches values such as signal time, particle density, and trigger information with their corresponding detector IDs. For each detector found in an event, a detector object is created and filled with these values. This method allows the code to automatically handle a different number of active detectors in each event, making the structure flexible and ready for future detector upgrades or changes [39][2]. A concise comparison of the old and new data formats is summarized in table 4.1 for quick reference.

4.2 NuRadioReco

NuRadioReco is an open source, modular Python framework developed for reconstructing signals from ultra high energy neutrinos and cosmic rays [2]. Although originally designed for in-ice radio detectors, it has since been adapted for ground based detectors like LOFAR and SKA due to its flexible and modular design. The framework clearly separates detector descriptions, event data, and processing modules, making it easy to extend and customize.

[2]private git repository

Table 4.1: Structural comparison between the old (2011–2019) and new (2020–2021) ROOT file formats used in LORA. The table highlights key differences in data organization, access patterns, and flexibility, emphasizing the transition from a detector-centric to an event-centric architecture.

Feature	**Old-Format (2011–2019)**	**New-Format (2020–2021)**
Primary tree used	*Tree_event*	*Tree_Event*
Detector data organization	One branch per detector (e.g., *Det1*, *Det2*, ...)	Arrays of detector values per event
Access pattern	Loop over individual detector branches	Iterate over detector arrays in each event
Flexibility	Fixed structure with up to 20 detectors	Dynamic with 40 detector data; supports varying number of detectors per event
Example variables	*DetX.GPS_time_stamp*, energy, thresholds	*Detector*, *Charge_Corrected*, *Peak_Height_Raw*
Data model orientation	Detector-centric	Event-centric
Scalability	Limited; requires structural changes for detector upgrades	Highly scalable; accommodates future expansions

Data in NuRadioReco is organized hierarchically as shown in figure 4.3. Each *Event* contains one or more *Stations*, which in turn include *Channels* representing voltage traces from antennas.

Reconstructed shower properties are stored in optional *Shower* objects. Detector descriptions are stored separately in JSON format and can include time-dependent configurations. This separation allows updates to detector models without modifying the original event data [40].

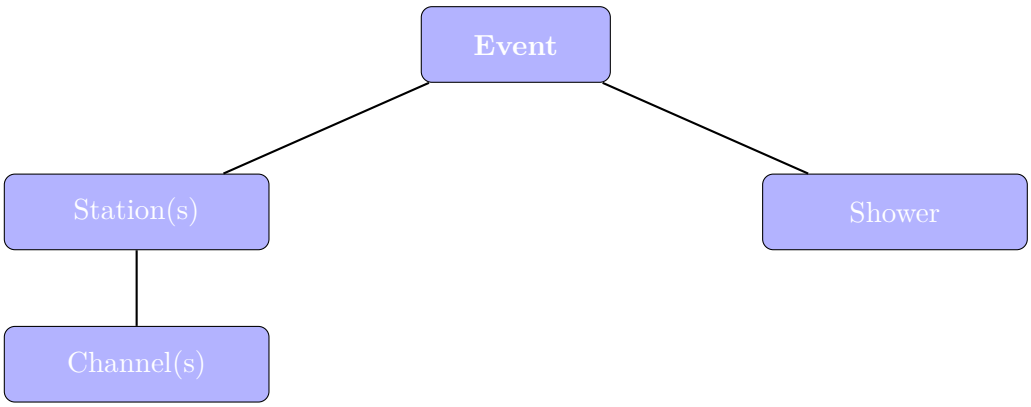

Figure 4.3: Schematic structure of an event, with associated stations, channels, and reconstructed shower information.

The framework uses a custom binary format (.nur) to store all relevant information, such as waveforms, geometry, and shower parameters. It can be installed via *pip* and is supported by detailed documentation, examples, and continuous integration for code quality. Recent updates which is an integral part of this thesis include support for particle detector data from LORA, enabling combined radio and particle data analysis within a single structure.

4.2.1 Available Data: Radio versus Particle Measurements

LOFAR radio measurements are processed natively by NuRadioReco modules. LORA provides particle based measurements, including detector trigger status, signal amplitudes, particle densities, and reconstructed core position, direction, and energy. These particle observables are complementary to radio data in a hybrid air shower analysis. To incorporate LORA information, the particle observables are added into NuRadioReco as a hybrid station within the **.nur** event structure. This enables subsequent joint analyses, such as cross-calibration of energy estimates and combined core or direction reconstruction. Radio data is available on NuRadioReco. This thesis addresses the integration of particle based data from ROOT files to .nur files, as detailed in the following sections.

4.2.2 Processing LORA ROOT Data to .nur files

Initially, LORA ROOT data was converted into intermediate files to validate particle based processing like human readable *.dat* tables and array based *.h5* datasets. NuRadioReco employs the **.nur** file format as a unified event container. Each .nur file encapsulates all relevant event information such as station geometry, channel parameters, waveforms, and shower-level results within a single, structured object. This eliminates separate .dat and .h5 I/O[3] and reduces processing overhead. It also enables efficient checkpointing and supports modular, reproducible workflows.

The function **ProcessEventV2** is used to process LORA ROOT files. It begins by identifying valid events with at least 9 active detectors. For each event, it loads the required detector data, such as position, signal, and gain, and reconstructs important shower parameters. These parameters include the core position, arrival direction, energy, and particle density. If an event passes all quality checks, the results are saved as a .nur file. The .nur file includes shower and detector parameters and allows further analysis within the NuRadioReco framework. A short code snippet of the core operations in this analysis is shown below. For full code, refer to the project repository [41],[39].

In this snippet:

[3] I/O stands for input/output, i.e. operations that read from or write to storage.

- **Reading ROOT data and quality cuts:** Timestamps and active detector counts are read from the *Tree_Event* branch using *read_all_events_from_root*. Events with fewer than 9 active detectors are discarded.

```
read.all_events_in_root(root_name, data_dir)
mask = n_active_dets >= 9
timestamps = timestamplist[mask]

```

- **Detector setup:** Detectors are initialized and populated with geometry, signal, and calibration data.

```
detectors = [detector.Detector(f'Det{i+1}') for i in range(n_det)]
detector.load_positions(detectors)
detector.load_signal(detectors)
detector.load_gain(detectors)

```

- **Computing event observables:** Arrival times, core position, direction, densities, and energy are derived and stored in an *Event* object.

```
ev = event.Event(...)
event.find_counts(det)
event.do_arrival_direction(detectors, ev)
event.NKG_fit_trial(detectors, ev)

```

- **Write valid events to .nur files:** If the event passes all criteria, it is serialized into a NuRadioReco compatible *.nur* file.

```
if ev.event_flag == 0:
    evt = nr_event.Event(run_number, event_id)
    write_nur(evt, detectors, ev, outputdir, run_number, j)

```

4.2.3 Writing NuRadioReco *.nur* Files

Once an event passes all quality checks, it is stored in NuRadioReco's hybrid format by encoding the reconstructed shower and detector-level information. The function **write_nur** is responsible for converting the processed LORA event into a structured *.nur* file for downstream analysis.

The process includes:

1. Creating a **HybridShower** object with parameters such as core position, arrival direction, and energy, derived from LORA fits.
2. Initializing a **HybridStation** and populating it with **HybridChannel** objects that hold per-detector observables like signal time and particle density.

3. Using the NuRadioReco **eventWriter** module to serialize the event and write it to save in *.nur* format.

A short code snippet:

```
shower = hybrid_shower.HybridShower('LORA')
shower.set_parameter(parameters.showerParameters.core, (ev.x_core, ev.y_core, 0.0))
shower.set_parameter(parameters.showerParameters.energy, ev.energy * 1e15)
# ...

station = hybrid_station.HybridStation(0)
for i, det in enumerate(detectors):
    channel = hybrid_channel.Channel(i)
    channel.set_parameter(parameters.hybridChannelParameters.signal_time, float(det.gps))
    # ...
    station.add_channel(channel)

evt.add_shower(shower)
evt.set_station(station)

writer = eventWriter.eventWriter()
writer.begin(output_path)
writer.run(evt)
writer.end()
```

This ensures that the final output is compatible with NuRadioReco's hybrid event analysis pipeline. For the full implementation, refer to the project repository [41], [39].

5 Analysis

5.1 Accounting for the stability of LORA over the years

This section examines different methods to assess the stability of LORA between 2011 and 2021. These methods include constructing the cosmic-ray energy spectrum, analyzing efficiency maps, and performing detailed statistical analysis using trigger count rates.

5.1.1 Data Selection for the Analysis

To investigate seasonal variations in the detection of cosmic ray air showers, data from the months of May and November representing summer and winter conditions, respectively, are selected. This allows a comparison of how LORA performs under different atmospheric and environmental conditions.

A cut criterion requiring a minimum of 9 triggered detectors is applied for event reconstruction. This ensures that only events with sufficient spatial information are used, providing reliable reconstruction quality. Although an alternative script exists in the project repository that uses LOFAR-triggered events as the selection criterion, it was not used in this analysis [39][1].

The dataset used in this analysis is limited to data collected up to and including the year 2021. Although the detector continued to trigger with some reliability until spring 2024, overall conditions were suboptimal. Several newly installed LORA stations experienced firmware related issues, while multiple older stations were non-functional due to hardware failures. As the full removal of the system was planned for the LOFAR2.0 upgrade, comprehensive repairs were not performed. As a result, data acquired after 2021 was collected under degraded conditions and was excluded from the analysis.

Between 2011 and 2021, the availability and quality of data varied across different years. In 2011, data collection only began on 17 May and the overall dataset for that year is notably inconsistent. Similarly in 2012, the May dataset includes data only up to the 20th of the month. No data was recorded in November 2017 resulting in a gap in the seasonal comparison for that year.

[1] private communication

Additionally, a change in the ROOT file data structure was introduced in November 2019 and the old ROOT structure was active till 15 November 2019. Due to this transition, the remainder of the 2019 dataset with the new ROOT structure i.e. from 16 November became corrupted and could not be used in the analysis. These limitations were taken into account during data selection to ensure consistency and reliability in the final dataset.

5.1.2 Core Position Distributions

The distribution of reconstructed core positions provides valuable insights into the spatial coverage and performance of the LORA detector array. To investigate this, all reconstructed air shower events were analyzed for a selected month and year. Each event file was parsed to extract the core coordinates in the local detector reference frame, along with the reconstructed primary energy.

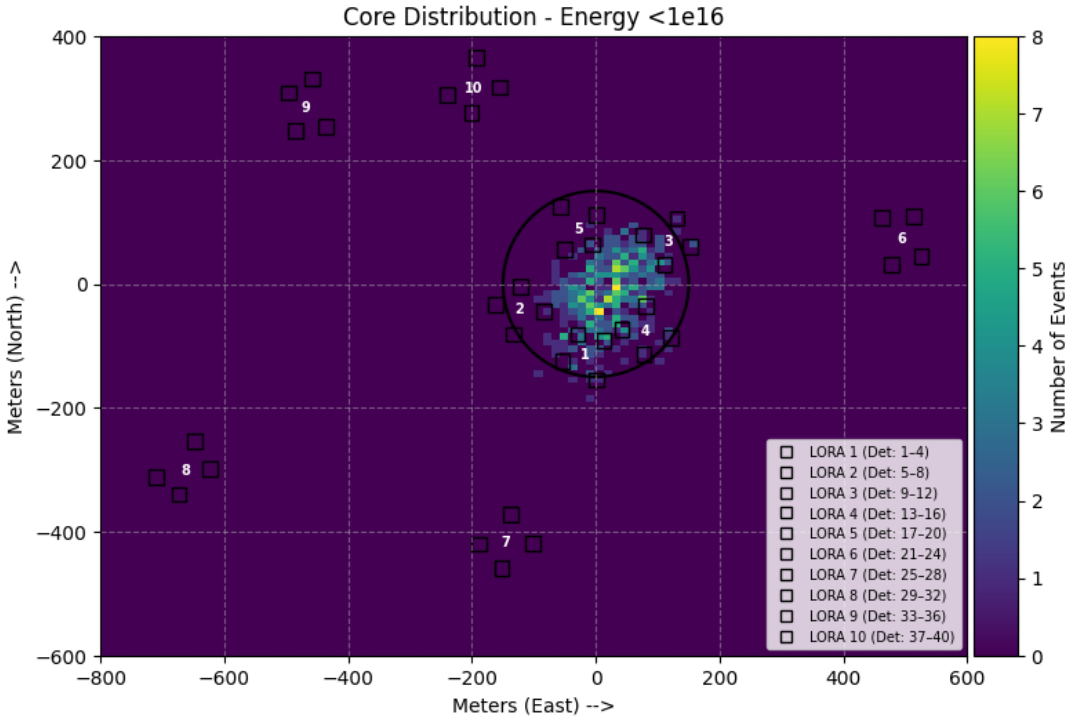

Figure 5.1: Core location distribution for May 2013 in the lowest energy bin ($E < 10^{16}$ eV), showing detector layout. Each black square denotes one detector. Four detectors comprise of 1 station denoted by LORAX, wher X = 1,2,..,10. The fiducial radius of 150m is denoted by the black circle in the centre. Distributions for higher energy bins are shown in figure B.4a, figure B.4b, and figure B.4c.

The detector array comprises multiple stations, each consisting of four scintillator detectors forming one station as shown in figure 5.1. Their known coordinates were used to verify the spatial location of each core relative to the deployed detectors.

The reconstructed cores were binned into four logarithmic energy intervals: below 10^{16} eV, 10^{16}–10^{17} eV, 10^{17}–10^{18} eV, and above 10^{18} eV for May and November of each year, ranging from 2011-2021. This allowed for an investigation of any potential energy dependence in the core location distribution. For visualization, two-dimensional histograms of core positions were generated for each energy bin. The detector positions were overlaid on these plots, together with a fiducial circle of 150 m radius, which defines the nominal region within which the reconstruction is expected to be reliable. Events falling significantly beyond this fiducial area were flagged for further inspection. These energy binned core histograms displayed no significant systematic displacement or clustering anomalies, indicating stable geometry and reconstruction behavior across the array.

Additionally, events reconstructed very close to a detector (< 10 m) were also identified, as these may be subject to systematic uncertainties. This systematic approach ensures that possible anomalies in the reconstruction, such as cores clustering near detector edges or far outside the array can be efficiently identified.

5.1.3 Cut Criteria and Efficiency

To ensure consistent event reconstruction and unbiased efficiency estimation, several quality and geometric cuts were applied to the dataset. These include constraints on the charged particle size and the lateral shower spread, as well as a radial cut on the core position of air showers. Figure 5.2 shows the core positions of the reconstructed showers before and after they pass the necessary cuts for this analysis

For each event, the shower core position (x, y), Molière radius r_M, primary energy E, and charged particle number N_{ch} were extracted from raw data. Events with unphysical values or missing fields were excluded. To suppress poorly reconstructed events and ensure stable lateral density fits, a cut of $\log_{10}(N_{\text{ch}}) > 6.25$ and 10 m $\leq r_M \leq$ 200 m was applied [14].

The core position distributions are divided into half decade bins as shown in figure 5.2:

$$\begin{cases} E < 1 \times 10^{16} \text{ eV}, \\ 1 \times 10^{16} \text{ eV} \leq E < 3.2 \times 10^{16} \text{ eV}, \\ 3.2 \times 10^{16} \text{ eV} \leq E < 1 \times 10^{17} \text{ eV}, \\ 1 \times 10^{17} \text{ eV} \leq E < 3.2 \times 10^{17} \text{ eV}, \\ 3.2 \times 10^{17} \text{ eV} \leq E < 1 \times 10^{18} \text{ eV}, \\ E \geq 1 \times 10^{18} \text{ eV}. \end{cases}$$

The radial distance from the array center for each shower is computed as $r = \sqrt{x^2 + y^2}$.

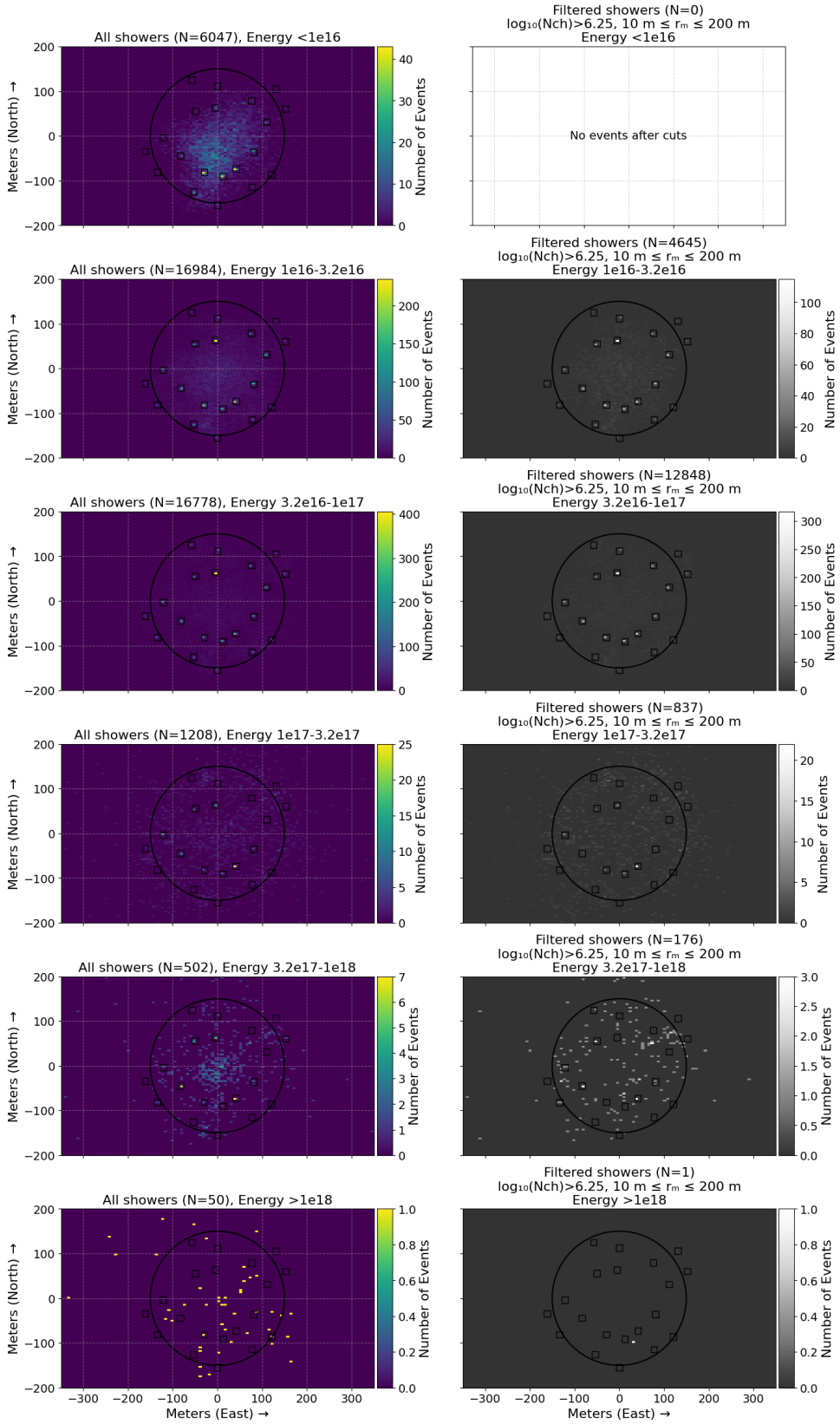

Figure 5.2: Left: all reconstructed shower cores in each energy bin, overlaid with the LORA detector layout (black squares) and the 150m fiducial circle.
Right: showers that satisfy $\log_{10}(N_{ch}) > 6.25$ and $10 \leq r_M \leq 200\,\text{m}$. Only one event passes the quality cuts in the highest energy.

Only events with reconstructed cores inside a maximum collection of 150 m fiducial radius are considered to define the region where the radial detection efficiency is evaluated. The radial core distances that pass these cuts are histogrammed in annular bins of 10 m width, up to the fiducial cut. The expected counts for a uniform core distribution are given by:

$$N_{\text{expected}}(r) = N_{\text{total}} \times \frac{A_{\text{bin}}}{A_{\text{total}}}, \quad A_{\text{bin}} = \pi(r_2^2 - r_1^2), \quad \epsilon(r) = \frac{N_{\text{observed}}(r)}{N_{\text{expected}}(r)}. \tag{5.1}$$

The ratio of observed to expected counts in each bin defines the radial detection efficiency as a function of core distance as shown in equation (5.1) and plotted in figure 5.3 and figure B.5

For all energy bins shown, $\epsilon(r)$ remains low, generally around 0.01–0.02 across all core distances up to about 150 m. There is no significant rise or fall with distance. Instead, the efficiency stays flat and close to zero within the statistical uncertainties. For the lowest energy bin ($< 10^{16}$ eV), no data passed the quality cuts. For the highest energy bin ($> 10^{18}$ eV), only one event passes the quality cuts resulting in large uncertainty due to poisson statistics.

Occasionally, the calculated efficiency slightly exceeds unity. This occurs because the expected counts $N_{\text{expected}}(r)$ are based on an idealized uniform exposure, assuming perfect geometrical acceptance. In practice, fluctuations in small sample sizes, reconstruction uncertainties, and local non-uniformities in the detector array can lead to more events being observed than expected in certain bins, especially at large radii or in high energy bins where statistics are low. Such values should be interpreted as consistent with 100% efficiency within statistical uncertainty.

Based on these results, choosing a cut at 150m therefore safely encompasses the region of highest trigger efficiency while avoiding regions where reconstruction quality and detector coverage begin to deteriorate. This ensures that only events with a reliably sampled core region are included in further analysis.

5.2 Comparative Analysis

All events are first subjected to a set of quality and geometrical cuts as discussed in section 5.1.3. This includes requiring $\log_{10}(N_{\text{ch}}) > 6.25$, a Molière radius in the range $10\,\text{m} \leq r_M \leq 200\,\text{m}$, and an additional zenith angle cut $\theta \leq 35°$.

The zenith cut ensures a more uniform detector response and limits the variation in atmospheric depth traversed by the shower, thereby reducing uncertainties related to shower development and energy reconstruction. These combined cuts preferentially select high energy, well reconstructed events with minimal variation in atmospheric path length.

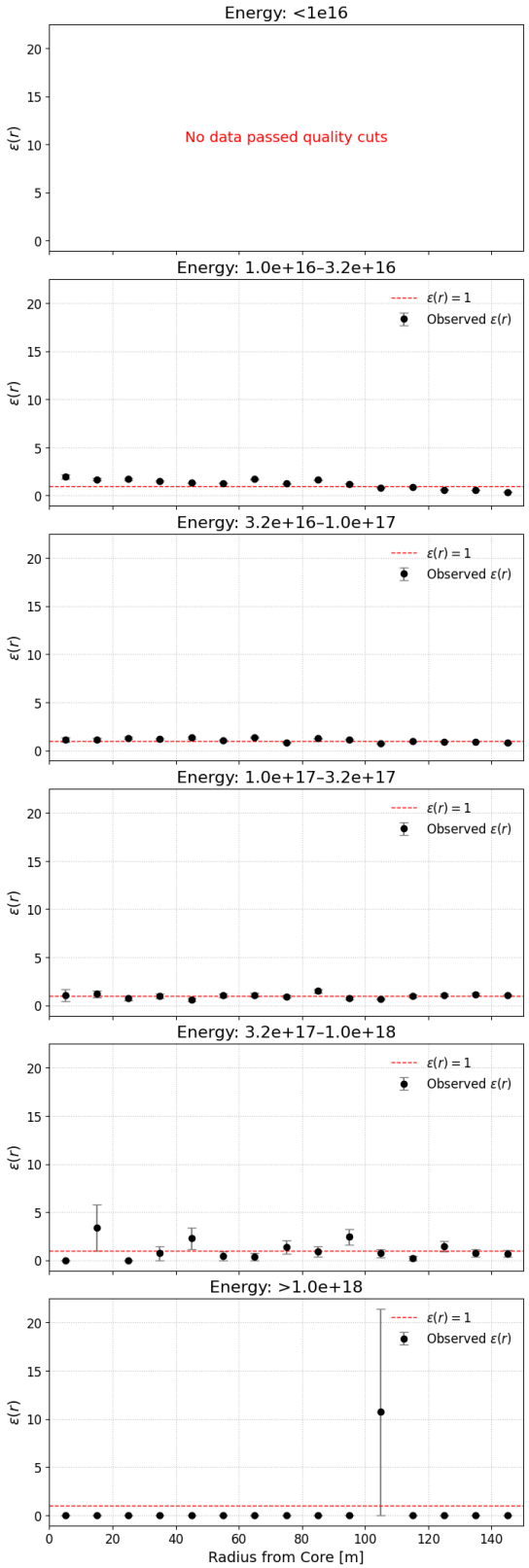

Figure 5.3: Radial detection efficiency $\epsilon(r)$ as defined in Eq. (5.1). The efficiency remains low ($\epsilon \sim 0.01$–0.02) across core distances up to the fiducial cut at 150 m, with no clear radial dependence. For $E < 10^{16}$ eV no data pass the quality cuts. At the highest energies, limited statistics cause large fluctuations yielding $\epsilon > 1$ due to Poisson uncertainties and the assumption of uniform exposure.

5.2.1 Energy Calibration

The relationship between the primary energy E and the shower size N_{ch} follows a power law, which becomes linear when expressed in logarithmic variables [35]:

$$\log_{10}(E) = a + b\,\log_{10}(N_{ch}), \tag{5.2}$$

where the fit parameters a (intercept) and b (slope) are obtained via least squares optimization to data. The fit covariance matrix yields the uncertainties σ_a and σ_b which is used to calculate the reconstructed energy E_R and its uncertainty is propagated from the calibration parameters as:

$$\sigma_{\log_{10}(E_R)} = \sqrt{\sigma_a^2 + (\log_{10} N_e)^2\,\sigma_b^2}, \tag{5.3}$$

thereby capturing the combined effect of both intercept and slope uncertainties on the reconstructed log-energy.

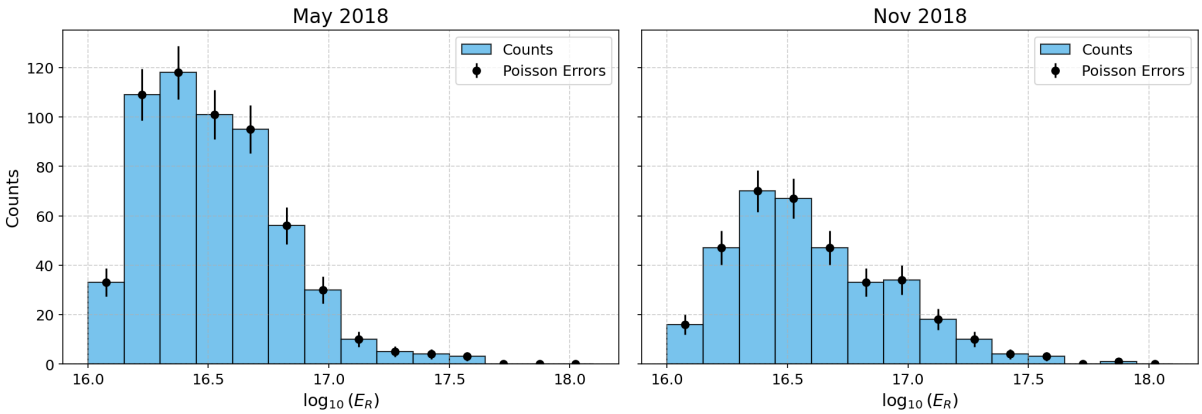

Figure 5.4: Histogram of reconstructed energy $\log_{10}(E_R)$ for LORA events with zenith angle $\theta \leq 35°$ from May and November 2018. The energy reconstruction is obtained by equation (5.2) and the bin widths in energies are determined by equation (5.4). The histogram bars represent event counts per energy bin, with Poisson error bars shown as black dots.

The reconstructed log-energies are histogrammed with bin width $\Delta \log_{10} E_R = 0.15$. Let N_i be the count in the i^{th} bin, and let the corresponding energy-bin edges be $E_{i-\frac{1}{2}}$ and $E_{i+\frac{1}{2}}$ in linear units. The bin width in energy is

$$\Delta E_i = E_{i+\frac{1}{2}} - E_{i-\frac{1}{2}}, \tag{5.4}$$

and the bin counts N_i as shown in figure 5.4 are assumed to follow Poisson statistics, yielding

$$\sigma_{N_i} = \sqrt{N_i} \tag{5.5}$$

5.2.2 Calculation of Differential Flux

The total acceptance A_i[2] is defined as the solid angle integrated effective area of the detector array, incorporating trigger and reconstruction efficiencies [14]:

$$A_i = \frac{\pi R_c^2}{2} \sum_k \epsilon_{\text{tot}}(E_i, \theta_k) \, (\cos 2\theta_k - \cos 2\theta_{k+1}) \,, \tag{5.6}$$

where $R_c = 150\,\text{m}$ is the fiducial radius of the array and $\epsilon_{\text{tot}}(E_i, \theta_k)$ is the total efficiency in zenith angle bins k covering $0°$ to $35°$. For each bin, the differential flux is then

$$\frac{\mathrm{d}I}{\mathrm{d}E}\Big|_i = \frac{N_i}{\Delta E_i \, A_i \, T_{\text{obs}}}, \tag{5.7}$$

where N_i is the number of events in an energy bin of width ΔE_i as computed in figure 5.4, and T_{obs} is the total live time. To present the spectrum in the conventional $E^3 \, \mathrm{d}I/\mathrm{d}E$ form, each bin's midpoint energy E_i is raised to the third power:

$$E_i^3 \, \frac{\mathrm{d}I}{\mathrm{d}E}\Big|_i = E_i^3 \times \frac{N_i}{\Delta E_i \, A_i \, T_{\text{obs}}}. \tag{5.8}$$

5.2.3 The Cosmic Ray Energy Spectrum

The monthly energy spectra for May and November from 2011 to 2021 are shown in a two-panel figure. The top panel displays the flux in the form $E^3 \, \mathrm{d}I/\mathrm{d}E$ versus energy on a log–log scale, with the Auger spectrum[3] overlaid for comparison. The Pierre Auger reference spectrum [42], is loaded from *cr_flux* utilities from NuRadioReco.

The bottom panel in figure 5.5 presents the ratio of the measured flux to the Auger reference:

$$R_i = \frac{(E_i^3 \, \mathrm{d}I/\mathrm{d}E)_{\text{det}}}{(E_i^3 \, \mathrm{d}I/\mathrm{d}E)_{\text{Auger}}}, \tag{5.9}$$

with associated statistical uncertainty given by:

$$\sigma(R_i) = R_i \sqrt{\left(\frac{\sigma_{\text{det}}}{(E_i^3 \, \mathrm{d}I/\mathrm{d}E)_{\text{det}}}\right)^2 + \left(\frac{\sigma_{\text{Auger}}}{(E_i^3 \, \mathrm{d}I/\mathrm{d}E)_{\text{Auger}}}\right)^2}. \tag{5.10}$$

[2] Acceptance values are taken from Figure 5 in [14], where they already include trigger and reconstruction efficiencies. At high energies the showers are always large enough to trigger the array and pass reconstruction, so the efficiency saturates at 100% and ϵ_{tot} can be taken as unity.

[3] Data measured by the Pierre Auger Observatory.[16]

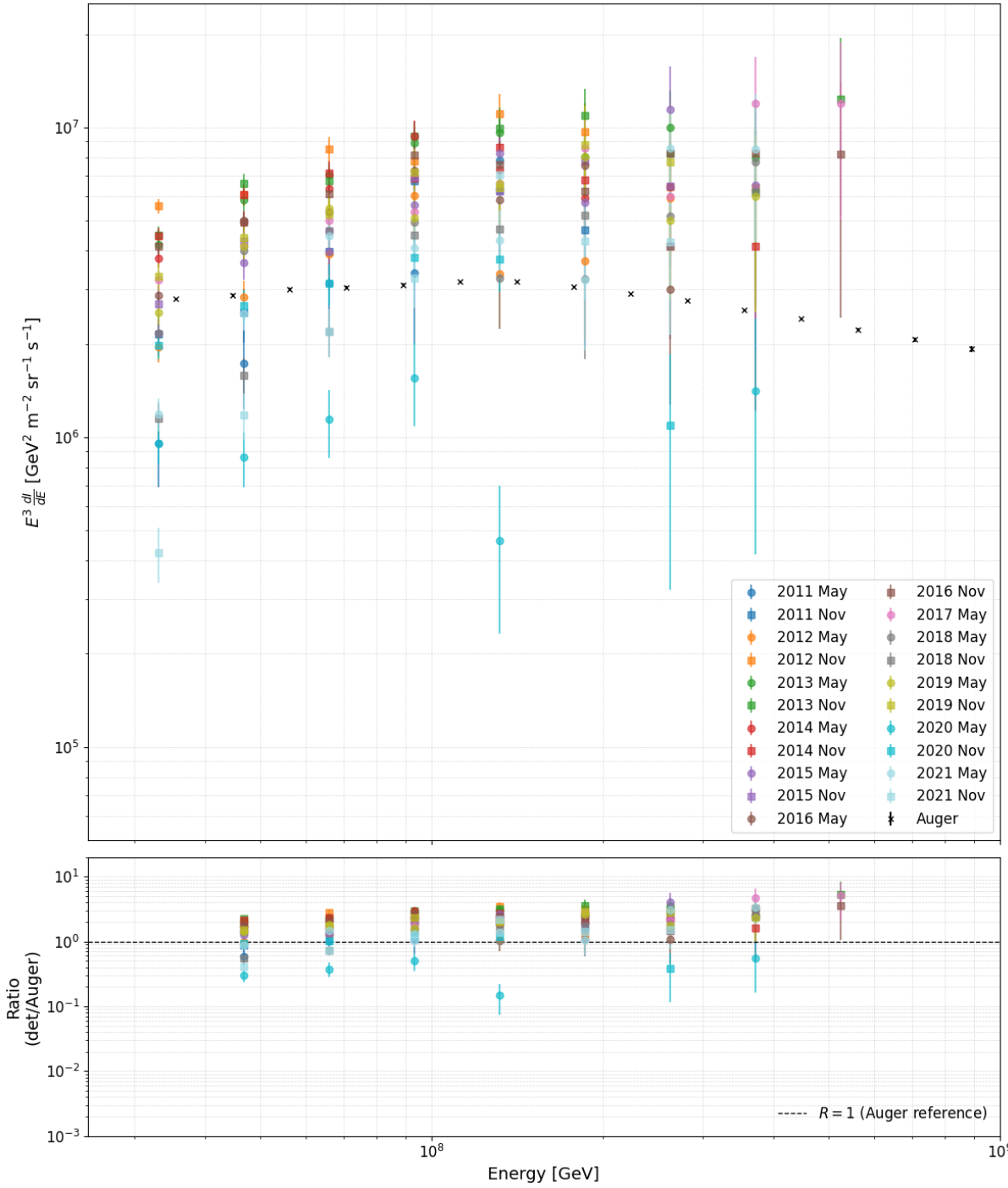

Figure 5.5: Top panel: Reconstructed spectra for May and November from 2011 to 2021 in [GeV]. Each point represents the flux in a logarithmic energy bin, scaled by E^3 to emphasize spectral features. Error bars denote statistical uncertainties. Auger reference spectrum is shown for comparison and it's data is taken from "The cosmic ray energy spectrum measured using the Pierre Auger Observatory" [42]. *For individual monthly histograms with Auger reference, see* figure B.6.
Bottom panel: Ratio of reconstructed spectra to Auger reference values. The dashed line at $R = 1$ indicates agreement. $R > 1$ indicates the detector measures more flux than Auger while $R < 1$ measures less flux.

A reference line at $R = 1$ in figure 5.5 marks agreement with the Auger data. Figure 5.6 shows the residuals $(R-1)$ as a function of time with it's respective statistical uncertainties, separately for May and November.

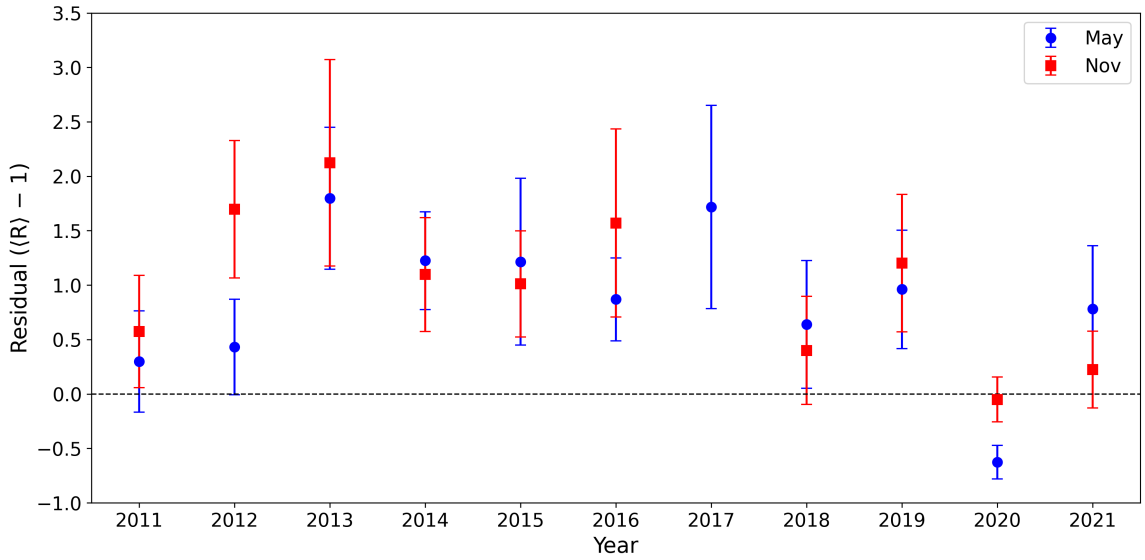

Figure 5.6: Residuals of the Auger-ratio, shown as $(R-1)$ versus year for May (blue circles) and November (red squares). The reference line at zero indicates agreement with the Auger flux. Positive residuals highlights the detector flux to be more than Auger while negative residuals means the detector flux is lower than Auger. Error bars represent the statistical uncertainties of the bin-averaged ratios. Fluctuations away from reference line reflect seasonal, systematic, or environmental effects, while the overall long-term behaviour remains broadly consistent with Auger.

The ratio R represents the measured flux of the detectors relative to that of Auger, serving as a benchmark for assessing the long-term stability of the detector system. As shown in figure 5.6 the residuals $(\langle R \rangle - 1)$ fluctuate around zero over the period 2011–2021, indicating overall consistency with Auger within uncertainties. In the early years (2011–2012), the May data remain close to good agreement with the reference measurements.

Between 2012 and 2017, the residuals exhibit a systematic excess with both May and November data. This suggests that the measured flux was consistently higher than Auger's benchmark during this interval, potentially due to seasonal effects, calibration drifts, or environmental influences affecting detector response. In 2018, the values gradually return closer to zero in figure 5.6. A notable exception occurs in 2020 with negative residuals, pointing to temporary operational or environmental factors.

Small yet noticeable seasonal differences between May and November are also visible across most years. This behavior indicates a possible seasonal or atmospheric contribution to the detector response, which may partially explain the observed long-term excess in residuals.

Overall, while year-to-year fluctuations are expected, the long-term behavior of R confirms that the detector system remains broadly stable relative to Auger. However the persistent tendency toward positive residuals combined with the small but noticeable seasonal differences, strongly suggests the presence of systematic effects beyond random statistical variation. These effects may arise from atmospheric conditions, seasonal influences, or calibration procedures. Identifying and correcting for these contributions will be crucial to further improving the long-term reliability and accuracy of the flux measurements.

To assess the overall agreement of LORA's reconstructed spectra with the Auger reference, all spectra from figure 5.5 were interpolated onto a common logarithmic energy grid. For each energy bin, the mean value and its 5–95% percentile envelope were computed across the full dataset. The Auger reference spectrum, with its corresponding uncertainties, was overlaid to facilitate direct comparison as shown in figure 5.7

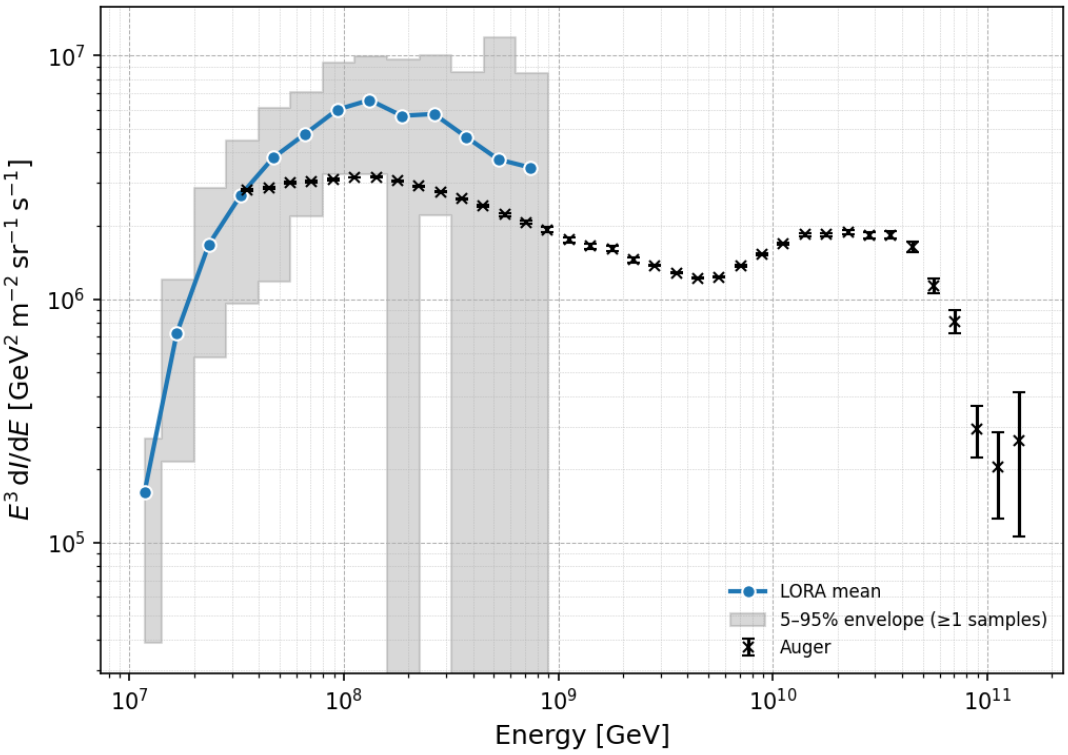

Figure 5.7: Mean LORA spectrum (blue) with 5–95% envelope (shaded grey) of all May/November samples from 2011–2021, plotted as $E^3\,\mathrm{d}I/\mathrm{d}E$ vs. energy (GeV). The grey envelope shows the spread of the data over the years. Black crosses show the Auger reference.

In figure 5.7, the mean LORA spectrum rises from $E^3\,\mathrm{d}I/\mathrm{d}E \approx 2 \times 10^5$ GeV^{2}m^{-2}sr^{-1}s^{-1} at 10^7 GeV to a maximum of $\sim 7 \times 10^6$ GeV^{2}m^{-2}sr^{-1}s^{-1} near 4×10^7 GeV, before turning over at higher energies. In the interval 10^7–10^8 GeV the LORA mean consistently lies 20–50% above the Auger reference (black crosses), yet remains encompassed by the 5–95% envelope (grey band).

Below 10^7 GeV and above 10^8 GeV, the envelope broadens or disappears entirely due to limited statistics. These results indicate that, over 2011–2021, the LORA mean spectrum lies around the Auger reference, reproducing the overall spectral shape.

A modest systematic excess of 20–50 % around the spectral peak (figure 5.7) falls within the 5–95 % uncertainty band, indicating that LORA accurately reproduces the spectrum's shape in comparison to Auger but shows small normalization differences. These may stem from residual calibration offsets of energy calibration parameters (a and b) in equation (5.2), uncorrected seasonal atmospheric variations, or minor acceptance mismatches. Future improvements such as time dependent recalibration of (a, b), real time atmospheric corrections, and cross checks with hybrid arrays will reduce these systematics and further confirm LORA's long-term stability.

5.3 Detection Efficiency Mapping

Another effective method to assess the long-term stability of the detector array is to compute and analyze annual efficiency maps over the period 2011–2021. These maps characterize spatial variations in detection probability across the array and help identify any systematic trends or degradations in performance over time. To ensure a consistent basis for comparison, the analysis is restricted to a fiducial region within 150 m of the array center, where detector response is expected to be most reliable. The procedure used to quantify and correct for non-uniformities in detector response within this region is described below.

To evaluate spatial variations in detector performance, the ground plane is divided into a grid of square bins, each measuring 20 m × 20 m. For each year, reconstructed shower core positions (x, y) from the months of May and November are assigned to these bins. Let N_{ij}^{obs} be the number of events observed in bin (i, j), whose center lies at a distance r_{ij} from the center of the detector array.

To assess how uniformly the detector responds across this area, the observed distribution is compared to an idealized flat (i.e., uniform) distribution, where each bin inside a circular fiducial region of radius $R = 150$ m is expected to receive an equal share of the total event count. The expected number of events in each bin under this assumption is given by:

$$N_{ij}^{\text{exp}} = \frac{\mathbb{I}[r_{ij} < R]}{\sum_{r_{kl}<R} \mathbb{I}[r_{kl} < R]} \sum_{r_{mn}<R} N_{mn}^{\text{obs}}, \tag{5.11}$$

where $\mathbb{I}[r < R]$ is an indicator function that equals 1 if the bin center is within the fiducial circle (i.e., $r < R$) and 0 otherwise. The denominator simply counts how many bins fall within this circle, and the numerator scales the total observed counts within the circle evenly among them.

The efficiency η_{ij} in each bin is then defined as the ratio of observed to expected counts:

$$\eta_{ij} = \frac{N_{ij}^{\text{obs}}}{N_{ij}^{\text{exp}}}, \qquad \eta_{ij} \leq 1, \quad \eta_{ij} = 0 \text{ for } r_{ij} \geq R. \tag{5.12}$$

This per-bin efficiency quantifies how well each part of the detector performs relative to a uniform detector. Values close to 1 indicate bins that behave as expected, while lower values reveal inefficiencies due to detector geometry, edge effects, or reconstruction quality. Outside the fiducial radius, bins are excluded from analysis and assigned zero efficiency.

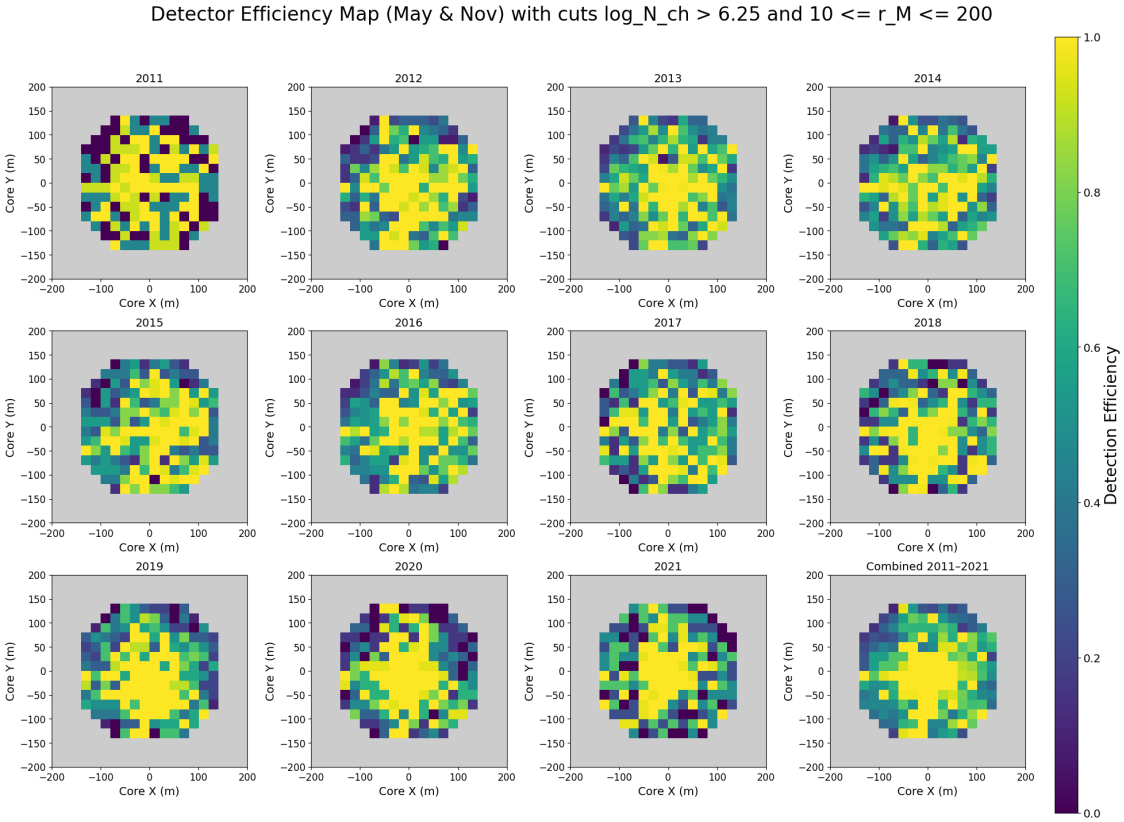

Figure 5.8: Annual detection efficiency maps on a 20 m × 20 m grid within the 150 m fiducial circle, combining May and November core positions from 2011–2021. This data is plotted after applying quality cuts ($\log_{10} N_{ch} > 6.25$, $10 \leq r_M \leq 200$ m). Efficiency η_{ij} is defined as the ratio of observed to expected counts, normalized to a uniform distribution. Since the expected counts sum to the observed total, the raw mean of η_{ij} would always be unity by definition. To make the mean efficiency sensitive to spatial variations, bins with $\eta_{ij} > 1$ are capped at one, so only deficits reduce the average. Central bins routinely exceed $\eta > 0.8$, while bins near the edge approach $\eta \approx 0$ where statistics vanish. From 2011 to 2013 the array quickly stabilizes (mean η rising from ~ 0.5 to ~ 0.75), remains uniform through 2017, dips in 2018 when fewer showers passed cuts, then recovers by 2020 before a slight decline in 2021. The combined 2011–2021 map (bottom right) confirms a remarkably uniform spatial response with no significant 'dead' regions after cuts.

Efficiency maps with and without the event quality cuts ($\log_{10} N_{ch} > 6.25$, $10 \leq r_M \leq 200$ m) are shown in figure 5.8 and figure B.7, respectively. The maps without cuts exhibit broader regions of reduced efficiency near the edges of the fiducial circle, indicating contributions from low-quality reconstructions and marginal triggers. Applying the cuts yields a more uniform efficiency distribution. In figure 5.9, the mean detection efficiency within 150 m after applying cuts is shown as a function of year (May and Nov) data, with their average plotted as a line.

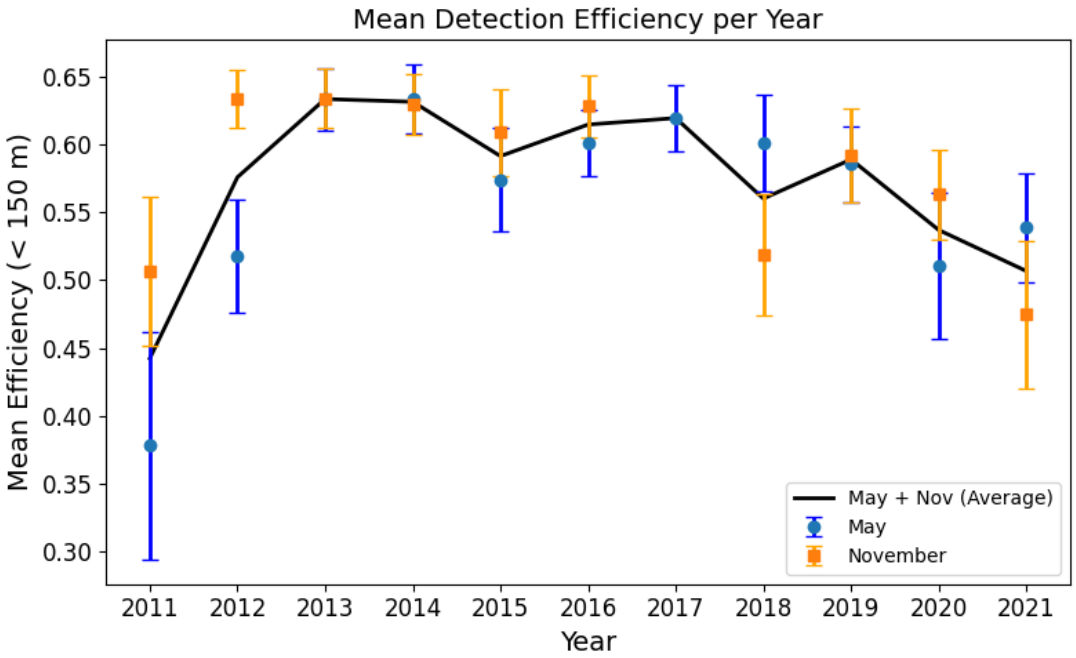

Figure 5.9: Annual mean detection efficiency within 150 m after quality cuts, shown separately for May and November samples from 2011–2021.

A rapid increase in efficiency is observed from 2011 to 2013, rising from approximately 0.44 to above 0.63. All datasets from 2011–2021 have been processed with the same reconstruction pipeline and calibration procedure, so the increase is not due to changes in analysis. Instead, it likely reflects the detector's early commissioning phase. During 2011–2012 for some detectors the data taking uptime was lower as mentioned in section 5.1.1, which reduced the fraction of well-reconstructed events within the fiducial radius.

By 2013, the array operated with higher stability and more consistently active stations, leading to improved efficiency. Since our efficiency metric is normalized to the number of triggered events, differences in global uptime do not directly bias the values shown in figure 5.9, but reduced stability in the earliest years would be highlighted as lower efficiency.

From 2013 to 2017, the efficiency remains high and stable, with inter-annual variations within 5% and May–November differences ≤ 0.03. This indicates reliable detector performance over these years. After 2017, the efficiency gradually declines from ~ 0.63 to 0.50 by 2021, suggesting possible aging effects or changes in data quality.

5.4 Statistical Analysis

5.4.1 Obtaining Trigger Counts from GPS Timestamps

As part of a broader statistical validation, GPS triggered event data from the LORA array were analyzed for the years 2011 to 2021 by processing the ROOT files to extract GPS timestamps associated with detector triggers. This was accomplished by reading the *Tree_event* structure present in each file up until 2019. In the updated ROOT file structure used for the 2020–2021 data, GPS timestamps corresponding to triggered events are stored in a centralized event tree labeled *Tree_Event* as discussed in section 4.1. Each entry in this tree contains two key components: the *GPS_Time_Stamp*, representing the absolute time of the event in Unix epoch format, and the *Detector* identifier, indicating which detector unit registered the trigger.

Unlike older formats where GPS data is spread across individual detector branches (e.g., *Det1*, *Det2*, ..., *Det40*), the modern structure consolidates this information into a single array. Each trigger event is associated with both a timestamp and a detector ID, which can be extracted and binned to create daily activity histograms for each detector.

5.4.2 Histograms for Trigger Counts Per Day

To visualize daily activity and assess the operational consistency of each detector, the collected GPS timestamps were converted into daily trigger counts. This was done by dividing the full calendar year into daily intervals and computing the number of triggers falling within each bin.Figure B.8 shows the daily raw counts for LORA ranging from 2011-2021.

Histograms were plotted for each detector, showing the number of triggers per day over the course of the year as shown in figure 5.10 and figure B.9 for a total of 20 and 40 detectors respectively. These plots provide an intuitive way to inspect the temporal structure of the data, revealing patterns, gaps, or abrupt changes in activity. The histograms serve as an effective tool for identifying periods of normal operation as well as potential anomalies.

5.4.3 Identifying and Dealing with Problematic Days in the Data

Upon inspection of the daily trigger histograms, certain days exhibit significant spikes in trigger rates that deviate from typical detector behavior. These anomalies can arise from various causes, such as hardware malfunctions, environmental noise, or configuration errors. By inspecting these anomalies, it becomes possible to determine whether a given spike is the result of a real physical event or an artifact of the detection system. This step is crucial for ensuring data quality and reliability for subsequent scientific analyses.

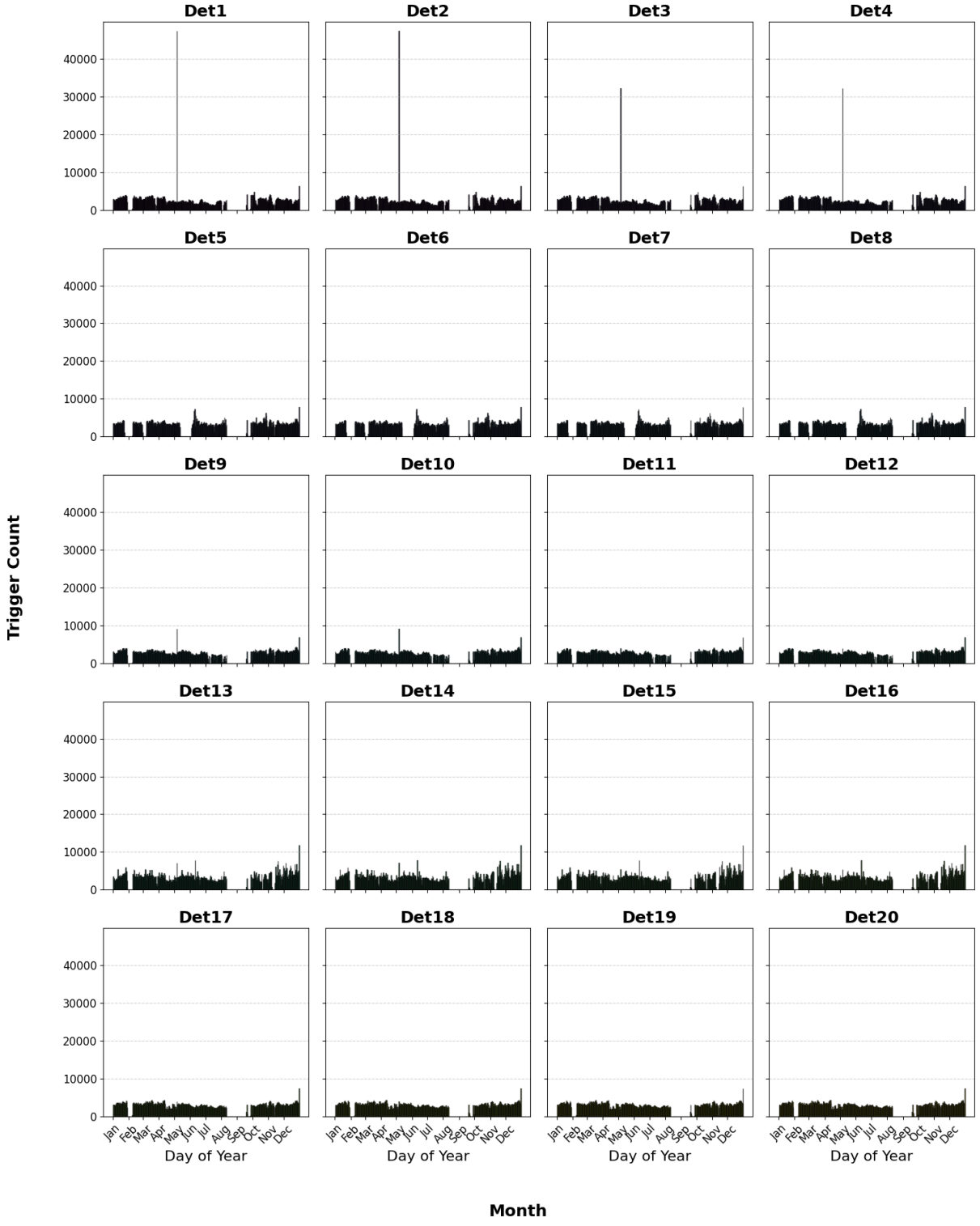

Figure 5.10: Daily trigger count histograms for Detectors 1–20 of the LORA array for the year 2013. Each subplot corresponds to a single detector and shows the number of triggers recorded per day throughout the year. The x-axis represents time in months (January to December), while the y-axis indicates the daily trigger count. Most detectors display consistent rates, suggesting stable operation. However, distinct high spikes are visible in detectors such as Det1, Det2, Det3, and Det4 indicating anomalous behavior.

Additionally, the cleaned trigger count data were stored in structured text files for future reference and quantitative comparison. This includes a review of the trigger configuration during the affected period, analysis of waveform traces, and evaluation of air shower reconstruction quality using Nishimura–Kamata–Greisen (NKG) fits.

ADC Traces

To study trigger events on flagged days, ADC traces are extracted from raw detector data and stored in *.h5* files as 2D arrays (*counts*), with rows as time indices and columns as detector channels. These traces show the time-resolved voltage recorded after each trigger, and are plotted with vertical offsets to compare pulse shapes and timing across detectors.

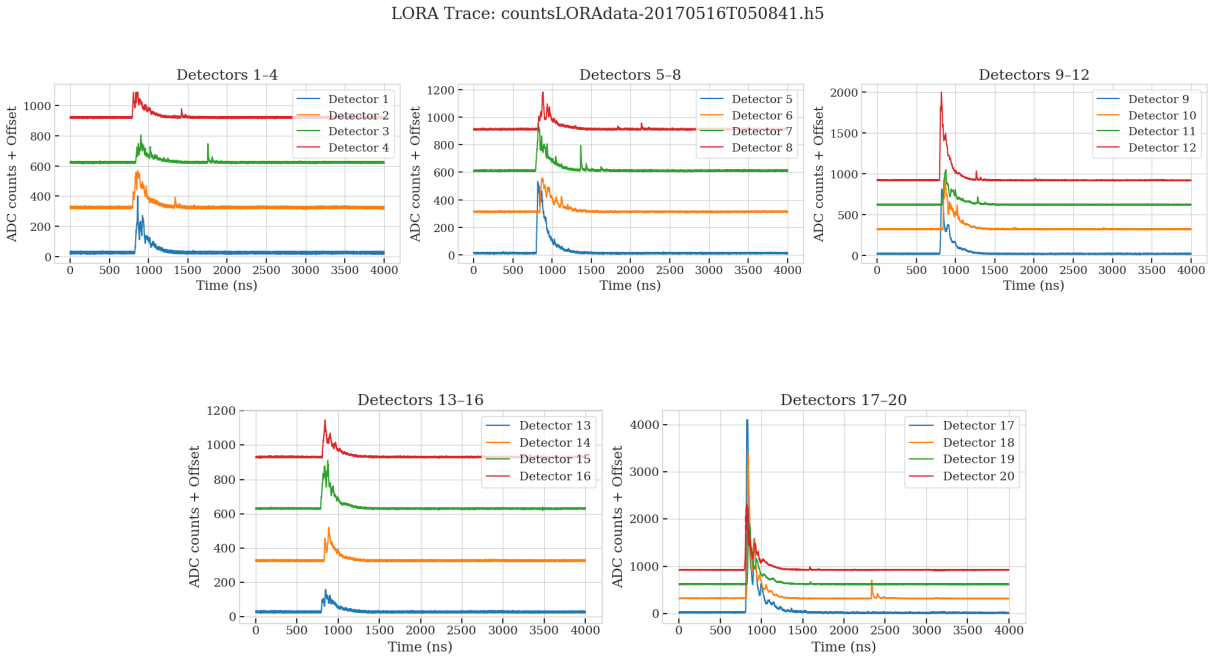

Figure 5.11: ADC traces for all 20 detectors of the LORA array corresponding to a well-reconstructed air shower event with their offset for visualization. Each subplot shows the time-dependent signal (in counts) for a single detector, with the x-axis representing the time index and the y-axis indicating ADC counts. A sharp peak followed by an exponential decay is visible in nearly all detectors. This is a characteristic of a typical particle-induced signal. The timing of the peaks is consistent across detectors, reflecting a coherent air shower front passing through the array. The absence of saturation, excessive noise, or clipped baselines indicates nominal detector performance and confirms this event as a reliable physical trigger.

A good air shower event typically displays a clear, narrow peak followed by an exponential decay which is a signature of particle arrival and signal shaping in the electronics. This characteristic is evident in the example shown in figure 5.11, where all 20 detectors exhibit coherent and

structured responses with consistent timing and amplitude differences. In contrast, the event illustrated in figure 5.12 shows irregular or excessively high signal levels in several detectors. The origin of such signal behavior remains unclear and needs further investigation.

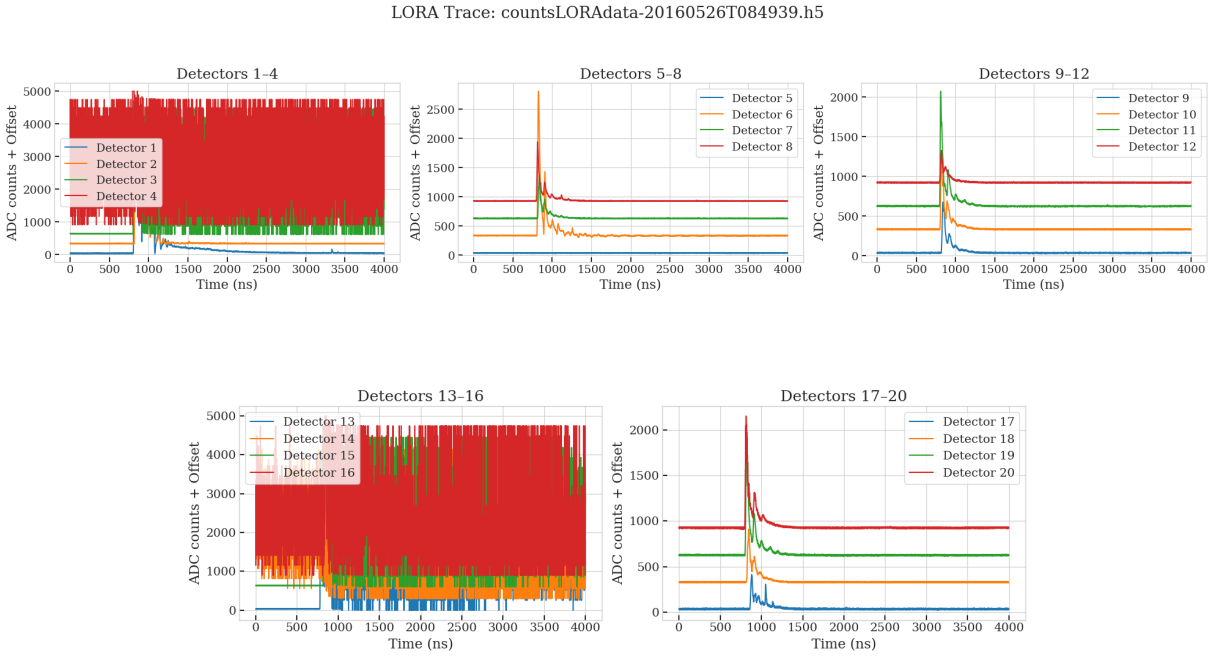

Figure 5.12: Example of a problematic ADC trace event with offset for visualization, across the 20 LORA detectors. While some stations (e.g., Detectors 5-8, 9–12, 17–20) show relatively clean traces, others (e.g., Detectors 1-4 and 13-16) exhibit abnormally high noise, saturation, or flat and unstable baselines. These anomalies manifest as excessive fluctuations, constant high counts, or complete loss of pulse shape, suggesting data corruption or readout instability. The precise cause of these distortions remains unclear.

NKG Fits

To further validate whether the detected events are physically consistent with extensive air showers, the lateral distribution of particle densities is fitted using the Nishimura–Kamata–Greisen (NKG) function with a fixed age parameter $s = 1.7$. For each event, the core position (x_{core}, y_{core}), particle densities ρ_i and detector positions (x_i, y_i) are read from the output files, and the radial distances $r_i = \sqrt{(x_i - x_{core})^2 + (y_i - y_{core})^2}$ are computed.

The fit function [14],

$$\rho(r) \;=\; N_{ch}\, C_s \left(\frac{r}{r_m}\right)^{s-2} \left(1 + \frac{r}{r_m}\right)^{-(4.5-s)},$$

with the normalization constant

$$C_s = \frac{\Gamma(4.5 - s)}{2\pi\, r_m^2\, \Gamma(s)\, \Gamma(4.5 - 2s)},$$

The fit is performed with a nonlinear least-squares algorithm (*scipy.optimize.curve_fit*) to find the shower size N_{ch} and Molière radius r_m. The fit parameters are kept within realistic limits by introducing bounds ($10\text{ m} \leq r_m \leq 300\text{ m}$, $10^3 \leq N_{ch} \leq 10^8$). If the solution lands exactly on one of these bounds, the event is flagged for possible bias. Events with fewer than four detectors that contribute valid data are discarded.

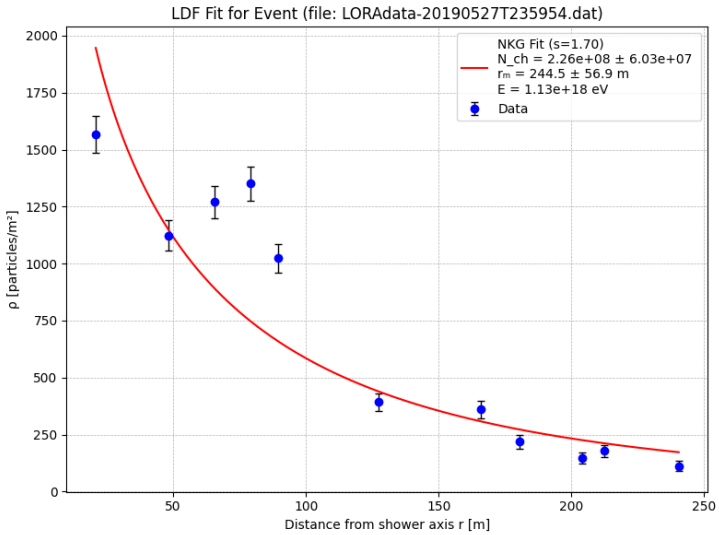

Figure 5.13: NKG fit to the lateral distribution for the highest energy event. Blue dots represent measured particle densities, and the red curve is the NKG model fit with a fixed age parameter s. The resulting fit parameters are shown in the legend.

An individual example of the NKG lateral distribution fit is shown in figure 5.13, based on the event file **LORAdata-20190527T235954.dat**. This is the highest energy event of $E \geq 1 \times 10^{18}$ eV, obtained after the cuts as shown in figure 5.2. For this analysis, the age parameter was fixed at $s = 1.7$, and the Molière radius r_m was left unconstrained to test the model's natural convergence behavior. The high particle count and relatively large r_m are consistent with expectations for ultra-high-energy cosmic rays. The large r_m value suggests the shower may be undersampled near the core.

To validate the accuracy of the core reconstruction, figure 5.14 shows the detector footprint for the same highest energy event. The reconstructed core (red star) lies within the densest part of the triggered detector array. Out of 40 total detectors in the full LORA layout, 12 were triggered for this event. The core is well-localized relative to the triggered detectors, indicating that the reconstruction is trustworthy and not biased by extreme peripheral detections. This supports the physical reliability of the large fitted r_m in the NKG profile.

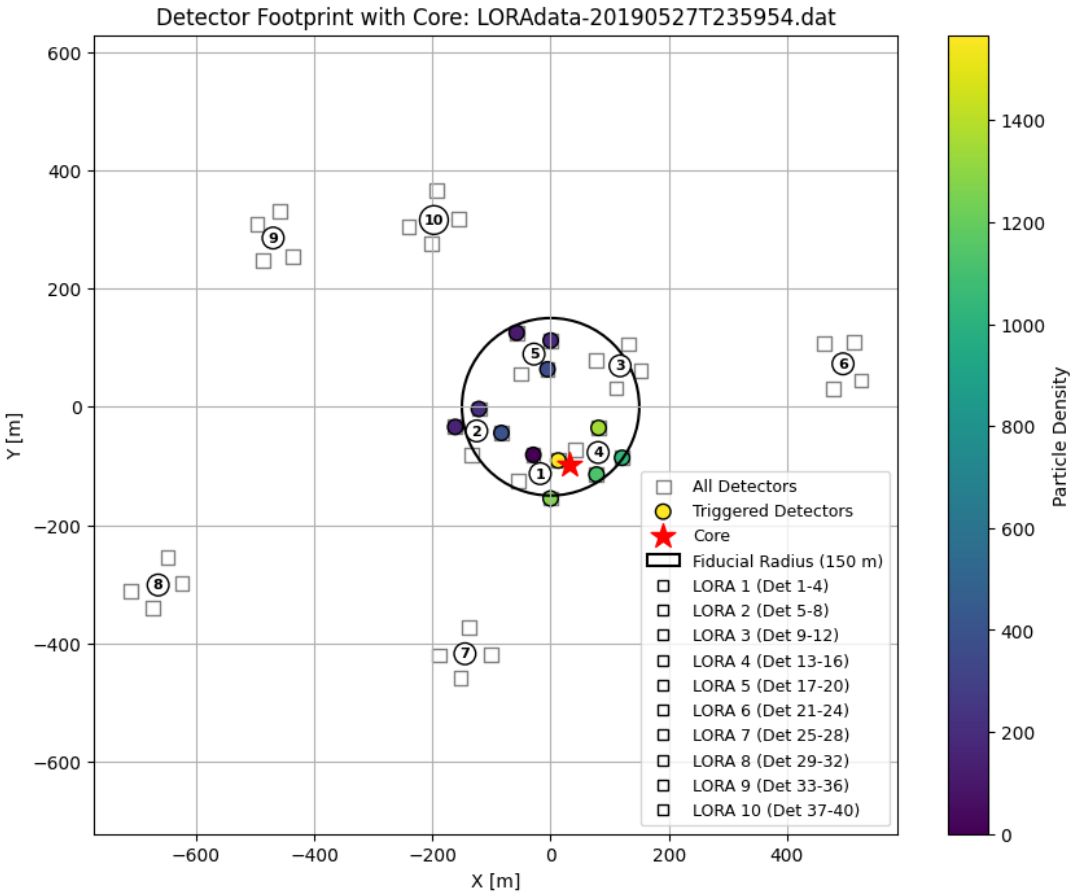

Figure 5.14: Detector footprint for the highest energy event. All 40 LORA detectors are shown as open gray squares. Colored circles indicate triggered detectors, with the color representing the measured particle density. The red star marks the reconstructed shower core. The black circle marks a fiducial radius of 150 m centered at the origin.

The multi-panel figure 5.15 illustrates that higher energy showers are characterized by larger particle counts and more compact lateral distributions. At $E \gtrsim 5 \times 10^{17}\,\mathrm{eV}$, the fits yield $\log_{10} N_{\mathrm{ch}} \approx 7.2$–$7.3$ with $r_m \approx 10$–$20\,\mathrm{m}$. At lower energies, both $\log_{10} N_{\mathrm{ch}}$ and shower compactness decrease, while r_m spans a broader range from $\sim 10\,\mathrm{m}$ up to $\sim 230\,\mathrm{m}$. Events with large r_m are typically associated with cores located farther from the instrumented region, leading to undersampling near the shower axis. Several fits, particularly at intermediate energies hit the lower r_m bound. This behavior is consistent with the statistics in table A.8, which indicate that ~ 20–25% of events overall (and up to ~ 40–50% in 2020–21) reach parameter boundaries. The table also shows that only $\sim 10\%$ of reconstructed cores fall within $10\,\mathrm{m}$ of a detector, reinforcing that core location and sparse sampling strongly influence NKG fit quality. A possible correlation between r_m and primary energy is suggested by these trends, though a more detailed future study (e.g. two-dimensional distributions of E vs. r_m or formal correlation tests) would be needed to quantify it.

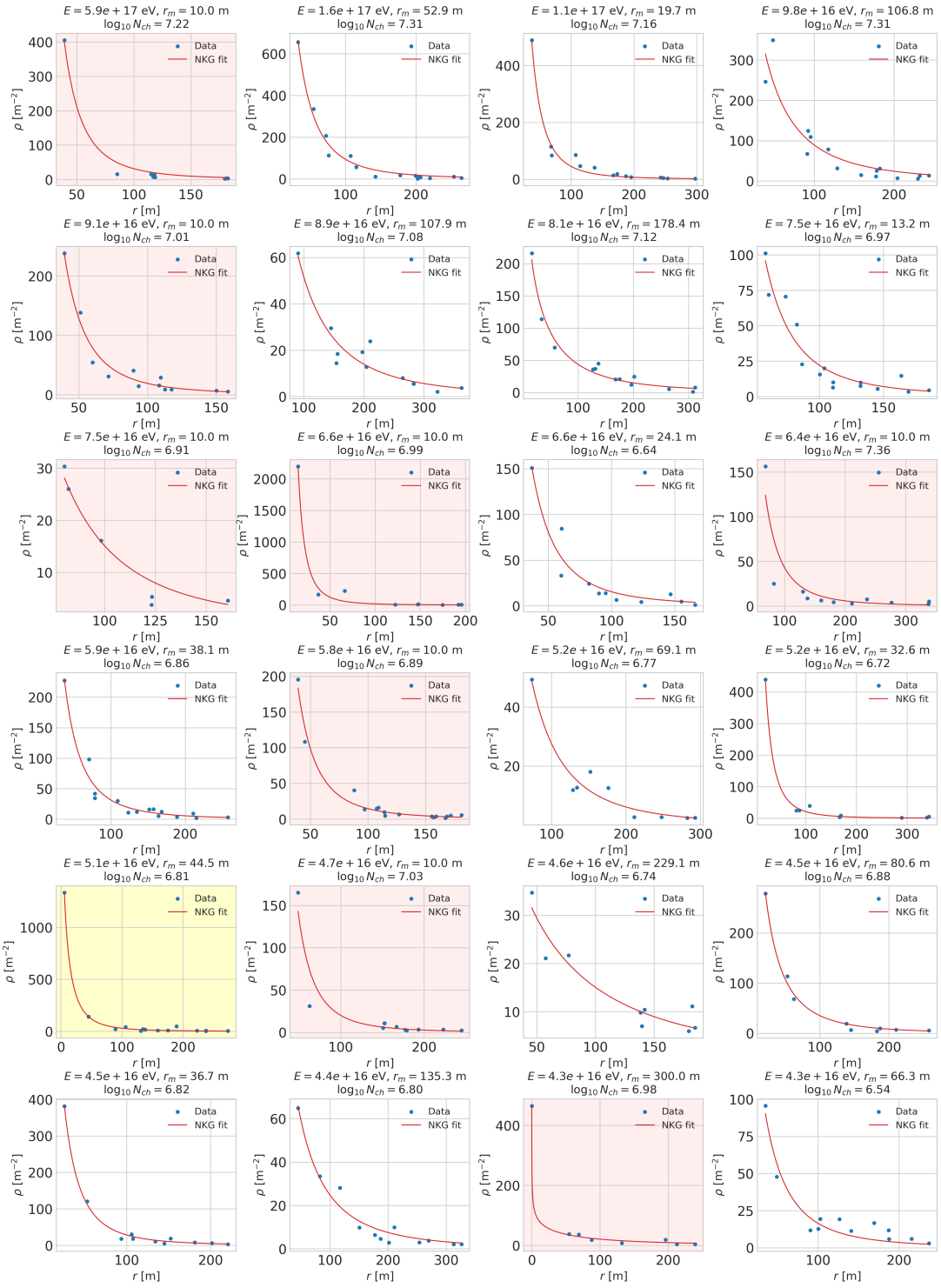

Figure 5.15: NKG fits to measured lateral density distributions for the 24 highest-energy air shower events recorded on 2012.11.04 (sorted by reconstructed primary energy, descending left to right, top to bottom). Each panel shows the measured particle density $\rho(r)$ versus core distance r with the best NKG fit (red curve). Titles report reconstructed primary energy E, fitted Molière radius r_m, and $\log_{10} N_{\mathrm{ch}}$. A red background indicates convergence at a fit boundary, while yellow marks events with a detector within 10 m of the core, signaling potential under-sampling at small r.

5.4.4 Annual Trigger Rate Distributions per Detector

In addition to the daily trigger count analysis shown in section 5.4.2, the detector performance was also evaluated using daily *trigger rates* (in Hz) over several years. While figure 5.10 and figure B.9 show the total number of triggers per day, this section focuses on the rate of triggers per second. The trigger rate for each day is calculated by dividing the number of recorded triggers by the total number of seconds in a day (86,400 s). This gives a normalized measure of detector activity that can be used to monitor stability and compare performance across different detectors and time periods.

Using the calculated daily trigger rates, histograms were made for each detector. Figure 5.16 shows the trigger rate distributions for Detectors 1 to 20 during the year 2011. In each panel, the red dashed line marks the average trigger rate for that detector, helping to spot any unusual behavior. These histograms make it easy to identify problems like noisy detectors, shifting thresholds, or irregular operation. Most detectors show stable and consistent rates throughout the year, with values grouped closely around the average. This suggests that the array was functioning reliably during this time.

Figure B.10 shows the trigger rate distributions for 2016. Compared to 2011, the rates remain mostly stable, with clear peaks around the mean and few signs of excessive noise or missing data. However, some detectors (such as Det5–Det8) show slightly broader distributions and higher means, suggesting mild threshold shifts or environmental influences. Overall, this indicates that the array's performance during the mid-decade period was still consistent and reliable, with only minor deviations that can be monitored and corrected.

While the majority of detectors in 2011 and 2016 were active and showed clean, Gaussian-like trigger distributions, the 2021 data exhibits more irregularities as shown in figure B.11. Several detectors (e.g., Det1–Det4, Det9–Det12) had no data, and others show broader or more asymmetric distributions. This reflects a decline in uniform operation, possibly due to aging hardware, reduced maintenance, or environmental factors over the decade. Nonetheless, some detectors, such as Det6–Det8 and Det13–Det20, still show relatively stable performance, allowing for continued scientific use with appropriate data quality checks. To complement this histogram based analysis of daily trigger rates, a detailed statistical summary for each detector is provided in Appendix A. This chapter compiles yearly metrics from 2011 to 2021, including the mean trigger rate, standard deviation, skewness, kurtosis, and coefficient of variation (CV).

The coefficient of variation (CV) was computed from daily trigger rates as:

$$\mathrm{CV}_{d,y} = \frac{\sigma}{\mu} \tag{5.13}$$

for detector d in year y, where μ is the arithmetic mean of the N daily rates and σ is the corresponding standard deviation. These CV values are then plotted over time.

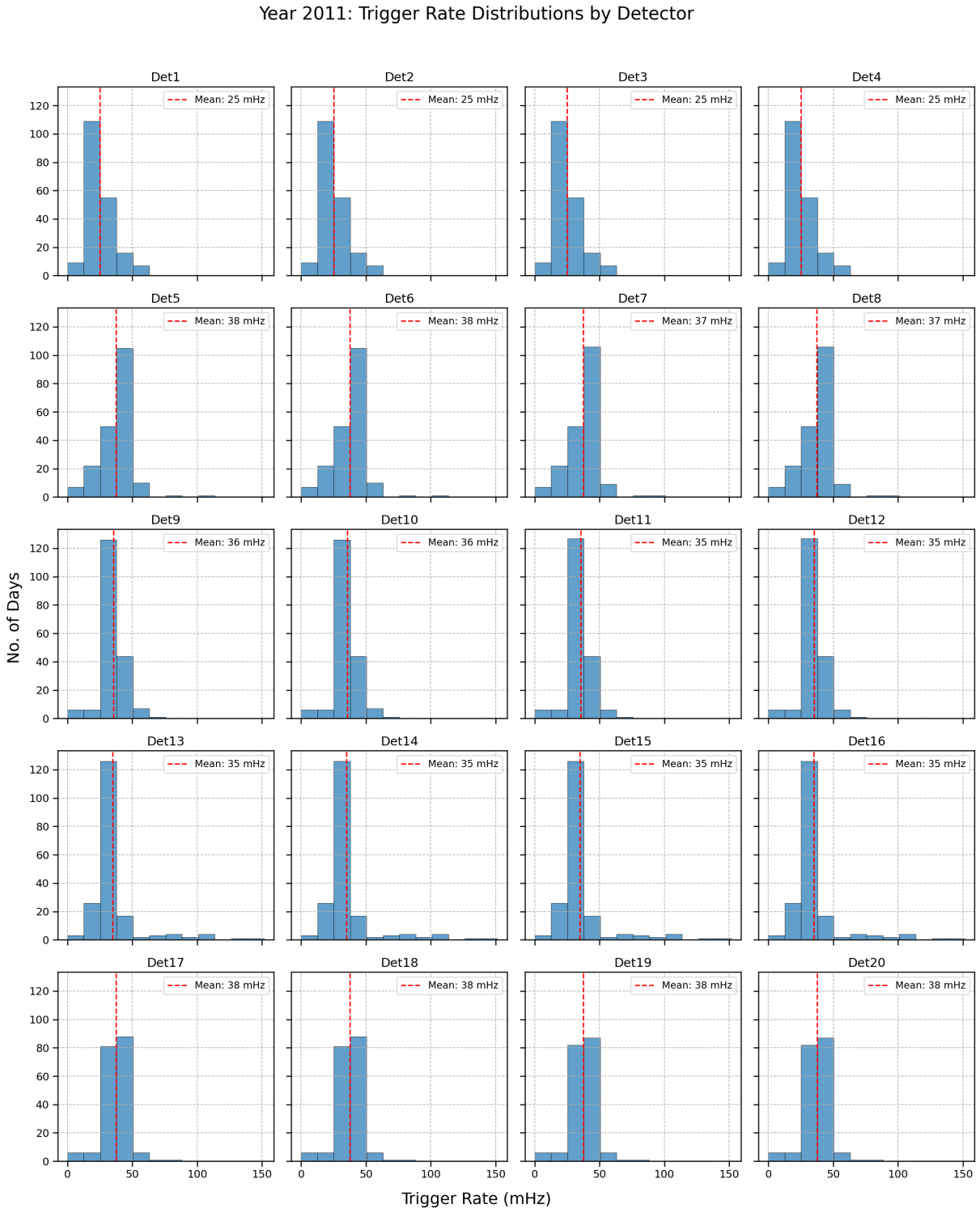

Figure 5.16: Trigger rate distributions for Detectors 1–20 during the year 2011. Each panel shows a histogram of daily trigger rates (in mHz) for one detector, computed from daily event counts. The red dashed line indicates the average rate over the year. Mean rate for each detector is marked in their respective legends (in mHz). Slight asymmetries or extended tails in some detectors may indicate occasional noise bursts or calibration drift.

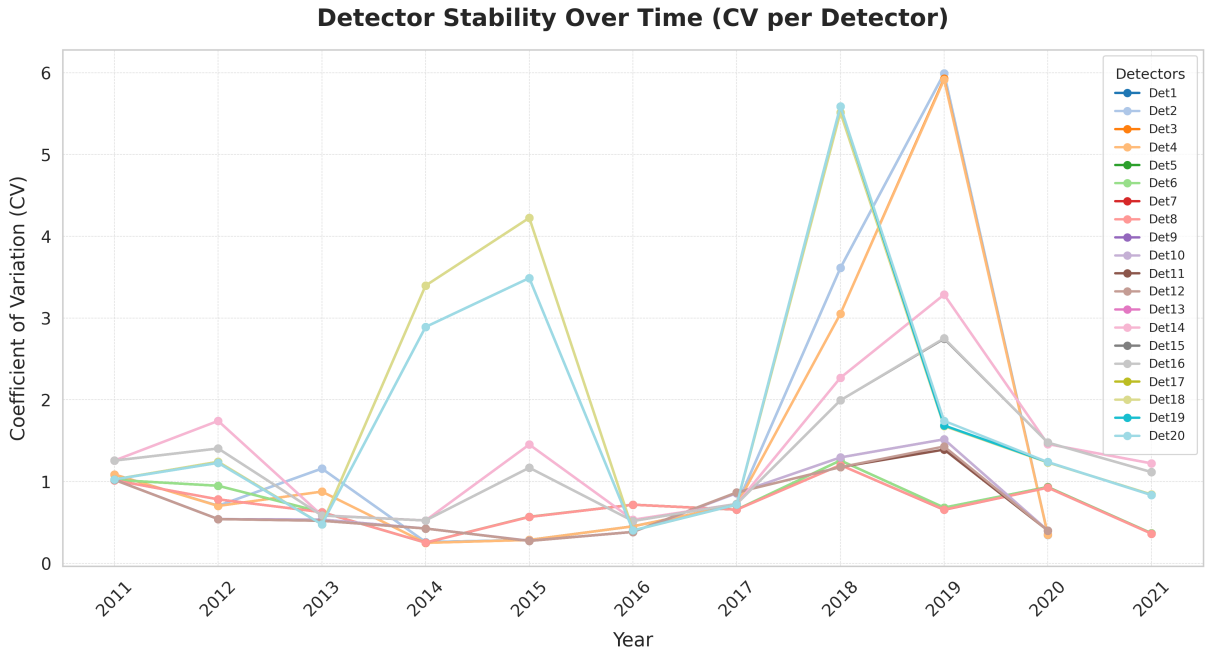

Figure 5.17: Trends in the coefficient of variation (CV) for 20 LORA signal detectors from 2011 to 2021. Each line represents the annual CV for a specific detector, indicating measurement stability over time. These CV plots help visualize and understand detector variability across the years at a glance.

Figure 5.17 shows the annual coefficient of variation (CV) for each detector from 2011 to 2021. For most detectors, the CV remains below 1 indicating stable and consistent daily trigger rates over time. However, certain detectors (e.g., Det1, Det2, Det3, Det18, Det19) exhibit pronounced spikes in CV in specific years, notably around 2014–2015 and 2018–2019. A detailed view of these CV trends for each individual detector is provided in figure B.12.

Detectors exceeding CV > 1 is mainly because low mean rates make the CV highly sensitive to occasional bad days (e.g. zero count periods or short bursts) that inflate the standard deviation. To separate such artifacts from genuine long-term variability, days with $Rate\_Hz = 0$ were removed and extreme outliers beyond [mean $\pm$ 3σ] excluded. The procedure is illustrated in figure 5.18, where the comparison of raw and cleaned CV clearly shows that the apparent spikes are driven by a few extreme days. The same analysis was applied to all years, with results shown in figure B.13.

This comparison demonstrates that the high CV values in the raw analysis are almost entirely driven by a few extreme days rather than true detector instabilities. After cleaning nearly all detectors exhibit CV < 1, confirming stable and consistent daily trigger rates over time.

Only in 2020 and 2021, a few detectors still show cleaned CV > 1, which suggests genuine long-term variability, likely related to hardware differences or calibration issues introduced during the expansion of the array from 20 to 40 detectors.

Together, these statistical checks for LORA data over 2011-2021 provide a comprehensive assessment of detector stability. Although some variations were observed, the overall performance of the array has remained stable over the long term. This decade-long consistency ensures that the cosmic-ray measurements obtained with LORA can be interpreted with confidence.

In addition, the systematic stability monitoring establishes a framework that can highlight underperforming or problematic detectors in future analyses. This is particularly important for hybrid studies with LOFAR's radio data and for composition analysis, where reliable detector performance is essential to distinguish genuine physical effects from instrumental artifacts. The robustness of the array operation therefore provides a solid foundation for the detailed conclusions presented in the next chapter.

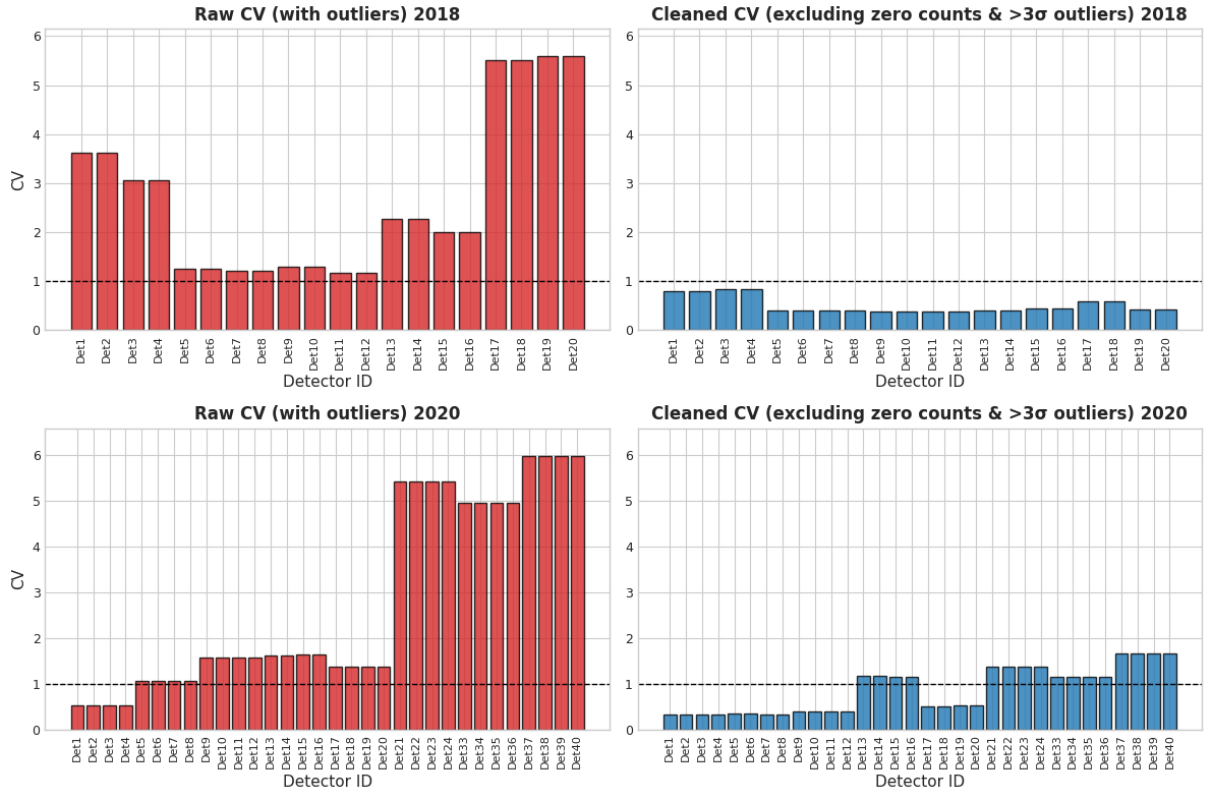

Figure 5.18: Illustration of the coefficient of variation (CV) for each detector in 2018 and 2020. For each year, the left panel shows the raw CV including all days, where several detectors exceed CV > 1 due to low mean rates and occasional outlier days (zeros or bursts). The right panel shows the cleaned CV after removing days with $Rate\_Hz = 0$ and excluding extreme outliers beyond [mean $\pm$ 3σ], demonstrating that most apparent instabilities are artifacts of a few extreme days. A few detectors still show cleaned CV > 1 in 2020, which suggests genuine long-term variability, likely related to hardware differences or calibration issues.

6 Discussion and Conclusion

This study evaluated the long-term performance and stability of the LOfar Radboud Air Shower Array (LORA), which is part of the Low-Frequency Array (LOFAR). The analysis covers LORA's detection of cosmic ray air showers over the period 2011 to 2021. By analyzing more than a decade of event data, this study assesses how the array's reconstruction capabilities evolved under varying seasonal and operational conditions.

To isolate intrinsic detector behavior from environmental effects, May and November were selected as representative summer and winter months (see section 5.1.1). Uniform selection criteria and energy binning minimized the impact of external variables like temperature and pressure. Data after 2021 were excluded due to increasing hardware degradation and firmware inconsistencies, preserving the dataset's reliability.

Radial detection efficiency $\epsilon(r)$ studies supported the use of a 150 m radial cut, beyond which detector performance declined. Within this range, $\epsilon(r)$ remained flat and low (0.01-0.02) with no significant trend across core distances (figure 5.3) or energy bins (figure 5.2). Occasional efficiency values go above 100% which are attributed to statistical fluctuations and idealized exposure models.

Energy calibration used a log-linear relation between shower size and primary energy (equation (5.2)), fitted empirically to account for detector aging and gain drifts. Because N_{ch} represents only the charged particle content at ground level, an empirical conversion is obtained by fitting the parameters a and b to data. The resulting parameter covariances were propagated to the reconstructed energy histograms (figure 5.4). A bin width of $\Delta \log_{10} E_R = 0.15$ balanced spectral resolution with statistical robustness.

Consistent quality cuts on charged particle count, core distance, and zenith angle ensured reliable energy reconstruction and flux estimates (section 5.1.3). The differential flux calculation (equation (5.8)) showed good agreement with the Pierre Auger reference spectrum, as quantified by the reconstructed-to-reference ratio and residual ratio plots (figure 5.5, figure 5.6).

Efficiency mapping revealed a commissioning phase rise in mean detection efficiency from $\sim$0.44 to $\sim$0.63 (2011–2013), followed by a stable plateau (2013–2017) with $< 2\%$ annual variation and < 0.03 seasonal spread (figure 5.9). A transient dip in 2018 reflects low statistics under strict cuts, while a gradual decline to $\sim$0.50 by 2021 indicates PMT gain drift and scintillator aging.

Daily trigger histograms exposed nominal operation and rare anomalies. Pronounced spikes in certain detectors (e.g., Det1–Det4 in 2013) were flagged as potential high-multiplicity showers or artifacts from electronic noise and environmental disturbances. Good and bad ADC traces are illustrated in figure 5.11 and figure 5.12, respectively.

Lateral distribution fits using the Nishimura–Kamata–Greisen (NKG) function were generally stable (table A.8). The age parameter is fixed to 1.7 to represent a stable shower stage beyond its maximum development, simplifying the analysis by reducing uncertainties in the lateral distribution fit. Events with cores reconstructed near detectors were flagged. Their exclusion produced negligible changes in the reconstructed cosmic-ray energy spectrum (figure 5.5).

The coefficient of variation (CV) of daily trigger rates was used to assess detector variability from 2011 to 2021. While raw CV values occasionally exceeded 1 due to zero-count periods or outlier days, cleaning the data (removing zeros and extreme outliers) showed that nearly all detectors maintained CV < 1, confirming stable long-term performance. Only a few detectors in 2020–2021 retained higher CV values after removing zeros and extreme outliers as seen in figure B.13, likely reflecting genuine variability introduced during the array expansion.

These CVs were not compared against any statistical model. Although a Poisson distribution is a natural choice for count data, the observed over-dispersion [1] of data violates its assumptions. A more sophisticated framework (e.g. negative binomial modelling) could accommodate this feature, but falls outside the present scope. Instead, the CV plots alone serve to identify detectors that may require maintenance or recalibration. A closer look at the annual statistics tables in Appendix A reveals notable patterns in detector stability over 2011–2021. A decadal overview of detector statistics confirmed three performance phases:

- **2011–2013:** Higher variability during commissioning (table A.1, table A.2),
- **2014–2017:** Operational stability with low CVs (table A.3, table A.4),
- **2018–2021:** Gradual decline due to aging and occasional data gaps (table A.5, table A.6, table A.7).

[1] Over-dispersion occurs when the variance of the data exceeds its mean, indicating more variability than expected under a Poisson model.

Final Remarks

This study demonstrates that the LOfar Radboud Air Shower Array (LORA) is a reliable and effective particle detection mechanism to study cosmic rays. For over more than ten years of operation, LORA delivered stable reconstruction of air shower parameters and reproducible flux estimates, even under seasonal and operational variations.

At the same time, this study shows some important limitations. The reconstructed LORA spectrum is consistently higher than the Pierre Auger reference (figure 5.7). This is expected, because LORA is a much smaller array that uses plastic scintillators, while Auger combines a very large array of water-Cherenkov detectors with fluorescence telescopes. These different methods of detection and calibration naturally lead to differences in the measured flux. In addition, LORA's long-term stability is affected by photomultiplier gain drift and scintillator aging, which need to be corrected to see true astrophysical signals.

Looking ahead, the integration of LORA's particle data with LOFAR's radio measurements offers the greatest potential for new discoveries. This combination can give much better information about the energy and composition of cosmic rays. The framework developed in this thesis already provides a solid starting point for such hybrid studies, and it can also be used for long-term monitoring of detector stability. For future composition analyses, it will be important to focus on the years when LORA worked at its best, to take into account problems in the particle data (such as bad traces or systematic offsets), and to use the detector variability statistics.

So far, detailed comparisons with Monte Carlo simulations were only carried out for the original 20 detectors before the 2019 upgrade. The additional 20 detectors installed afterwards have not yet been studied in this way. Extending the simulation-based validation to the full upgraded array is therefore an important task for future work.

In short, a particle detection array like LORA does work, but one has to be careful. Its scientific potential is best realized only when environmental effects, detector aging, and statistical uncertainties are explicitly taken into account. This thesis demonstrates both the strengths and the limitations of the array and provides a foundation on which the next generation of cosmic-ray studies like LOFAR2.0 and Square Kilometre Array (SKA) telescope can be confidently built.

A - Appendix

The tables below summarize key statistics for each detector by year to assess stability and outliers. The **Mean** is the average rate while **Std dev** (standard deviation) reflects typical fluctuations. The **CV**, coefficient of variation = (Std dev/Mean) normalizes variation where low CV (e.g. < 0.3) suggests stability while high CV (e.g. > 1) suggests instability. The **Median**, compared to the mean, shows skew. **Skewness** quantifies asymmetry. Positive values indicate occasional spikes while negative ones, rare dips. **Kurtosis** measures tail heaviness. Values near 3 match a normal distribution, whereas kurtosis $\gg 3$ reveals heavy tails and infrequent extreme values. **Min and Max rate** show the full range observed. Together, these metrics profile each detector's yearly performance rates and variability.

Table A.1: Detector Statistics for Year 2011

Year	Detector	Mean	Std dev	CV	Median	Skewness	Kurtosis	Min rate	Max rate
2011	Det1	0.0252	0.0104	0.4115	0.0216	1.1546	1.7074	0.0001	0.0624
2011	Det2	0.0252	0.0104	0.4115	0.0216	1.1546	1.7074	0.0001	0.0624
2011	Det3	0.0251	0.0103	0.4112	0.0216	1.1507	1.6945	0.0001	0.0623
2011	Det4	0.0251	0.0103	0.4112	0.0216	1.1507	1.6945	0.0001	0.0623
2011	Det5	0.0376	0.0116	0.3083	0.0393	0.3428	6.6945	0.0002	0.1014
2011	Det6	0.0376	0.0116	0.3083	0.0393	0.3428	6.6945	0.0002	0.1014
2011	Det7	0.0375	0.0112	0.3000	0.0392	0.0491	5.9965	0.0002	0.0998
2011	Det8	0.0375	0.0112	0.3000	0.0392	0.0491	5.9965	0.0002	0.0998
2011	Det9	0.0355	0.0089	0.2503	0.0354	−0.2612	4.5214	0.0002	0.0756
2011	Det10	0.0355	0.0089	0.2503	0.0354	−0.2612	4.5214	0.0002	0.0756
2011	Det11	0.0355	0.0088	0.2479	0.0354	−0.3269	4.6520	0.0002	0.0756
2011	Det12	0.0355	0.0088	0.2479	0.0354	−0.3269	4.6520	0.0002	0.0756
2011	Det13	0.0350	0.0203	0.5792	0.0293	3.0884	11.1216	0.0001	0.1516
2011	Det14	0.0350	0.0203	0.5792	0.0293	3.0884	11.1216	0.0001	0.1516
2011	Det15	0.0349	0.0202	0.5783	0.0293	3.1054	11.2691	0.0001	0.1515
2011	Det16	0.0349	0.0202	0.5783	0.0293	3.1054	11.2691	0.0001	0.1515
2011	Det17	0.0376	0.0093	0.2482	0.0382	−0.4378	6.8887	0.0000	0.0849
2011	Det18	0.0376	0.0093	0.2482	0.0382	−0.4378	6.8887	0.0000	0.0849
2011	Det19	0.0376	0.0093	0.2480	0.0382	−0.4410	6.9451	0.0000	0.0849
2011	Det20	0.0376	0.0093	0.2480	0.0382	−0.4410	6.9451	0.0000	0.0849

(a) Year 2011: Detectors with CV 0.25–0.30 show moderate stability, whereas CV 0.58–0.58 (e.g. Det 13–16) indicates higher variability. Positive **skewness** implies occasional high-rate outliers elevating the mean, while negative **skewness** (e.g. Det 17–20) signals rare low-rate dips. High kurtosis (> 3) means there are occasional extreme rate fluctuations beyond what a normal distribution would predict, likely due to intermittent noise or environmental effects.

Table A.2: Detector Statistics for Years 2012 and 2013

Year	Detector	Mean	Std dev	CV	Median	Skewness	Kurtosis	Min rate	Max rate
2012	Det1	0.0313	0.0099	0.3173	0.0326	1.8673	11.5525	0.0031	0.0949
2012	Det2	0.0313	0.0099	0.3173	0.0326	1.8673	11.5525	0.0031	0.0949
2012	Det3	0.0313	0.0098	0.3134	0.0326	1.7195	10.5034	0.0031	0.0919
2012	Det4	0.0313	0.0098	0.3134	0.0326	1.7195	10.5034	0.0031	0.0919
2012	Det5	0.0418	0.0317	0.7585	0.0405	15.2488	252.2633	0.0030	0.5704
2012	Det6	0.0418	0.0317	0.7585	0.0405	15.2488	252.2633	0.0030	0.5704
2012	Det7	0.0412	0.0238	0.5775	0.0405	13.8139	221.4951	0.0030	0.4256
2012	Det8	0.0412	0.0238	0.5775	0.0405	13.8139	221.4951	0.0030	0.4256
2012	Det9	0.0332	0.0081	0.2436	0.0344	−0.4275	3.5375	0.0044	0.0756
2012	Det10	0.0332	0.0081	0.2436	0.0344	−0.4275	3.5375	0.0044	0.0756
2012	Det11	0.0332	0.0081	0.2435	0.0344	−0.4290	3.5440	0.0044	0.0755
2012	Det12	0.0332	0.0081	0.2435	0.0344	−0.4290	3.5440	0.0044	0.0755
2012	Det13	0.0376	0.0536	1.4266	0.0296	9.2175	92.9972	0.0000	0.6668
2012	Det14	0.0376	0.0536	1.4266	0.0296	9.2175	92.9972	0.0000	0.6668
2012	Det15	0.0363	0.0399	1.0983	0.0297	8.8352	88.5614	0.0040	0.4894
2012	Det16	0.0363	0.0399	1.0983	0.0297	8.8352	88.5614	0.0040	0.4894
2012	Det17	0.0429	0.0262	0.6096	0.0392	4.4405	31.2911	0.0002	0.2737
2012	Det18	0.0429	0.0262	0.6096	0.0392	4.4405	31.2911	0.0002	0.2737
2012	Det19	0.0426	0.0256	0.6001	0.0391	4.0284	26.3217	0.0000	0.2577
2012	Det20	0.0426	0.0256	0.6001	0.0391	4.0284	26.3217	0.0000	0.2577

(a) Year 2012: CV values around 0.24–0.31 (e.g. Det 9–12) imply stable detectors, whereas Det 13–16 (CV > 1.0) show high volatility. High skewness and kurtosis across several detectors point to irregular spikes or drops in rates.

Year	Detector	Mean	Std dev	CV	Median	Skewness	Kurtosis	Min rate	Max rate
2013	Det1	0.0314	0.0310	0.9884	0.0298	15.1536	250.6423	0.0006	0.5489
2013	Det2	0.0314	0.0310	0.9884	0.0298	15.1536	250.6423	0.0006	0.5489
2013	Det3	0.0308	0.0216	0.7018	0.0298	12.8307	200.6959	0.0006	0.3722
2013	Det4	0.0308	0.0216	0.7018	0.0298	12.8307	200.6959	0.0006	0.3722
2013	Det5	0.0408	0.0102	0.2506	0.0409	−0.3044	6.5000	0.0017	0.0893
2013	Det6	0.0408	0.0102	0.2506	0.0409	−0.3044	6.5000	0.0017	0.0893
2013	Det7	0.0407	0.0102	0.2504	0.0408	−0.3177	6.4840	0.0017	0.0893
2013	Det8	0.0407	0.0102	0.2504	0.0408	−0.3177	6.4840	0.0017	0.0893
2013	Det9	0.0329	0.0098	0.2982	0.0343	0.6136	11.5221	0.0011	0.1044
2013	Det10	0.0329	0.0098	0.2982	0.0343	0.6136	11.5221	0.0011	0.1044
2013	Det11	0.0327	0.0089	0.2737	0.0343	−0.7836	4.5645	0.0011	0.0797
2013	Det12	0.0327	0.0089	0.2737	0.0343	−0.7836	4.5645	0.0011	0.0797
2013	Det13	0.0408	0.0147	0.3604	0.0400	1.1542	6.3213	0.0010	0.1362
2013	Det14	0.0408	0.0147	0.3604	0.0400	1.1542	6.3213	0.0010	0.1362
2013	Det15	0.0407	0.0146	0.3576	0.0400	1.1397	6.5289	0.0010	0.1362
2013	Det16	0.0407	0.0146	0.3576	0.0400	1.1397	6.5289	0.0010	0.1362
2013	Det17	0.0353	0.0080	0.2261	0.0362	−0.4338	7.4562	0.0012	0.0846
2013	Det18	0.0353	0.0080	0.2261	0.0362	−0.4338	7.4562	0.0012	0.0846
2013	Det19	0.0352	0.0080	0.2271	0.0361	−0.4271	7.3748	0.0012	0.0846
2013	Det20	0.0352	0.0080	0.2271	0.0361	−0.4271	7.3748	0.0012	0.0846

(b) Year 2013: Detectors 5–8 and 17–20 show strong stability (CV ≤ 0.25). Detectors 1–4 have high CV and extreme kurtosis/skewness, indicating volatility. Skewness near zero (e.g. Det 5–8) suggests symmetric rate distributions.

Table A.3: Detector Statistics for Years 2014 and 2015

Year	Detector	Mean	Std dev	CV	Median	Skewness	Kurtosis	Min rate	Max rate
2014	Det1	0.0321	0.0084	0.2601	0.0321	5.4429	75.8679	0.0000	0.1399
2014	Det2	0.0321	0.0084	0.2601	0.0321	5.4429	75.8679	0.0000	0.1399
2014	Det3	0.0321	0.0080	0.2499	0.0321	4.5196	61.7608	0.0000	0.1302
2014	Det4	0.0321	0.0080	0.2499	0.0321	4.5196	61.7608	0.0000	0.1302
2014	Det5	0.0371	0.0092	0.2468	0.0385	−1.2773	2.3614	0.0001	0.0567
2014	Det6	0.0371	0.0092	0.2468	0.0385	−1.2773	2.3614	0.0001	0.0567
2014	Det7	0.0371	0.0092	0.2468	0.0385	−1.2766	2.3592	0.0001	0.0567
2014	Det8	0.0371	0.0092	0.2468	0.0385	−1.2766	2.3592	0.0001	0.0567
2014	Det9	0.0330	0.0088	0.2661	0.0327	0.3362	3.7854	0.0000	0.0783
2014	Det10	0.0330	0.0088	0.2661	0.0327	0.3362	3.7854	0.0000	0.0783
2014	Det11	0.0330	0.0088	0.2658	0.0325	0.3211	3.6855	0.0000	0.0776
2014	Det12	0.0330	0.0088	0.2658	0.0325	0.3211	3.6855	0.0000	0.0776
2014	Det13	0.0384	0.0201	0.5236	0.0337	1.0262	0.8664	0.0007	0.1153
2014	Det14	0.0384	0.0201	0.5236	0.0337	1.0262	0.8664	0.0007	0.1153
2014	Det15	0.0384	0.0201	0.5237	0.0337	1.0263	0.8659	0.0007	0.1153
2014	Det16	0.0384	0.0201	0.5237	0.0337	1.0263	0.8659	0.0007	0.1153
2014	Det17	0.0453	0.1535	3.3912	0.0347	17.0817	304.9812	0.0000	2.8464
2014	Det18	0.0453	0.1535	3.3912	0.0347	17.0817	304.9812	0.0000	2.8464
2014	Det19	0.0433	0.1249	2.8862	0.0347	16.9074	299.9787	0.0000	2.3125
2014	Det20	0.0433	0.1249	2.8862	0.0347	16.9074	299.9787	0.0000	2.3125

(a) Year 2014: Det1–Det12 show high stability (CV $\approx$ 0.25–0.27) with moderate skewness/kurtosis. Det13–Det16 are moderately variable (CV $\approx$ 0.52) but low kurtosis. Det17–Det20 exhibit extreme variability (CV $>$ 2.8) and heavy tails (kurtosis $>$ 299), indicating instability or rare outliers.

Year	Detector	Mean	Std dev	CV	Median	Skewness	Kurtosis	Min rate	Max rate
2015	Det1	0.0290	0.0081	0.2802	0.0293	2.2061	16.2992	0.0000	0.0896
2015	Det2	0.0290	0.0081	0.2802	0.0293	2.2061	16.2992	0.0000	0.0896
2015	Det3	0.0290	0.0081	0.2803	0.0293	2.2060	16.2942	0.0000	0.0896
2015	Det4	0.0290	0.0081	0.2803	0.0293	2.2060	16.2942	0.0000	0.0896
2015	Det5	0.0530	0.0286	0.5394	0.0641	0.0894	0.8787	0.0009	0.2028
2015	Det6	0.0530	0.0286	0.5394	0.0641	0.0894	0.8787	0.0009	0.2028
2015	Det7	0.0529	0.0284	0.5371	0.0641	0.0257	0.5120	0.0009	0.1947
2015	Det8	0.0529	0.0284	0.5371	0.0641	0.0257	0.5120	0.0009	0.1947
2015	Det9	0.0311	0.0084	0.2699	0.0309	1.9749	12.7438	0.0000	0.0906
2015	Det10	0.0311	0.0084	0.2699	0.0309	1.9749	12.7438	0.0000	0.0906
2015	Det11	0.0311	0.0083	0.2680	0.0309	1.9966	13.2621	0.0000	0.0906
2015	Det12	0.0311	0.0083	0.2680	0.0309	1.9966	13.2621	0.0000	0.0906
2015	Det13	0.0358	0.0518	1.4466	0.0308	13.4610	193.8684	0.0102	0.8541
2015	Det14	0.0358	0.0518	1.4466	0.0308	13.4610	193.8684	0.0102	0.8541
2015	Det15	0.0349	0.0407	1.1637	0.0308	13.2139	192.2005	0.0102	0.6810
2015	Det16	0.0349	0.0407	1.1637	0.0308	13.2139	192.2005	0.0102	0.6810
2015	Det17	0.0484	0.2030	4.1947	0.0277	13.1201	192.2829	0.0005	3.3065
2015	Det18	0.0484	0.2030	4.1947	0.0277	13.1201	192.2829	0.0005	3.3065
2015	Det19	0.0433	0.1501	3.4631	0.0277	12.9933	190.2456	0.0000	2.4506
2015	Det20	0.0433	0.1501	3.4631	0.0277	12.9933	190.2456	0.0000	2.4506

(b) Year 2015: Det1–Det4 remain stable (CV $\approx$ 0.28). Det5–Det8 show moderate variability (CV $\approx$ 0.54). Det13–Det16 are unstable (CV $>$ 1.1, heavy tails). Det17–Det20 exhibit extreme fluctuations (CV $>$ 3.4, high kurtosis), indicating rare bursts or outliers.

Table A.4: Detector Statistics for Years 2016 and 2017

Year	Detector	Mean	Std dev	CV	Median	Skewness	Kurtosis	Min rate	Max rate
2016	Det1	0.0303	0.0059	0.1961	0.0302	−0.4982	9.2318	0.0000	0.0666
2016	Det2	0.0303	0.0059	0.1961	0.0302	−0.4982	9.2318	0.0000	0.0666
2016	Det3	0.0304	0.0057	0.1876	0.0302	−0.1407	8.9630	0.0001	0.0666
2016	Det4	0.0304	0.0057	0.1876	0.0302	−0.1407	8.9630	0.0001	0.0666
2016	Det5	0.0361	0.0209	0.5800	0.0340	1.0092	0.3656	0.0002	0.0936
2016	Det6	0.0361	0.0209	0.5800	0.0340	1.0092	0.3656	0.0002	0.0936
2016	Det7	0.0361	0.0209	0.5800	0.0340	1.0088	0.3646	0.0002	0.0936
2016	Det8	0.0361	0.0209	0.5800	0.0340	1.0088	0.3646	0.0002	0.0936
2016	Det9	0.0296	0.0068	0.2307	0.0300	0.0499	4.4471	0.0001	0.0691
2016	Det10	0.0296	0.0068	0.2307	0.0300	0.0499	4.4471	0.0001	0.0691
2016	Det11	0.0296	0.0068	0.2307	0.0300	0.0517	4.4539	0.0001	0.0691
2016	Det12	0.0296	0.0068	0.2307	0.0300	0.0517	4.4539	0.0001	0.0691
2016	Det13	0.0304	0.0118	0.3882	0.0284	1.3878	6.1627	0.0001	0.1103
2016	Det14	0.0304	0.0118	0.3882	0.0284	1.3878	6.1627	0.0001	0.1103
2016	Det15	0.0302	0.0111	0.3681	0.0284	0.8276	2.1997	0.0001	0.0891
2016	Det16	0.0302	0.0111	0.3681	0.0284	0.8276	2.1997	0.0001	0.0891
2016	Det17	0.0273	0.0051	0.1859	0.0269	−0.3338	6.6493	0.0009	0.0566
2016	Det18	0.0273	0.0051	0.1859	0.0269	−0.3338	6.6493	0.0009	0.0566
2016	Det19	0.0273	0.0051	0.1860	0.0269	−0.3341	6.6429	0.0009	0.0566
2016	Det20	0.0273	0.0051	0.1860	0.0269	−0.3341	6.6429	0.0009	0.0566

(a) Year 2016: Det1–Det4 and Det17–Det20 show excellent stability (CV ≈0.19), slight negative skew. Det9–Det12 are also stable (CV ≈0.23). Det5–Det8 have moderate variability (CV ≈0.58) with nearly symmetric distributions. Det13–Det16 show moderate CV (≈0.37–0.39) and occasional high-rate outliers (skewness >0).

Year	Detector	Mean	Std dev	CV	Median	Skewness	Kurtosis	Min rate	Max rate
2017	Det1	0.0286	0.0061	0.2128	0.0282	−1.2894	5.4837	0.0000	0.0433
2017	Det2	0.0286	0.0061	0.2128	0.0282	−1.2894	5.4837	0.0000	0.0433
2017	Det3	0.0286	0.0061	0.2127	0.0282	−1.2916	5.4982	0.0000	0.0433
2017	Det4	0.0286	0.0061	0.2127	0.0282	−1.2916	5.4982	0.0000	0.0433
2017	Det5	0.0353	0.0069	0.1948	0.0358	−2.2517	8.3699	0.0001	0.0525
2017	Det6	0.0353	0.0069	0.1948	0.0358	−2.2517	8.3699	0.0001	0.0525
2017	Det7	0.0353	0.0069	0.1948	0.0358	−2.2518	8.3701	0.0001	0.0525
2017	Det8	0.0353	0.0069	0.1948	0.0358	−2.2518	8.3701	0.0001	0.0525
2017	Det9	0.0273	0.0124	0.4549	0.0276	4.1643	41.7755	0.0001	0.1542
2017	Det10	0.0273	0.0124	0.4549	0.0276	4.1643	41.7755	0.0001	0.1542
2017	Det11	0.0270	0.0126	0.4669	0.0271	4.0190	39.6684	0.0001	0.1541
2017	Det12	0.0270	0.0126	0.4669	0.0271	4.0190	39.6684	0.0001	0.1541
2017	Det13	0.0234	0.0077	0.3281	0.0228	0.0029	0.3420	0.0000	0.0449
2017	Det14	0.0234	0.0077	0.3281	0.0228	0.0029	0.3420	0.0000	0.0449
2017	Det15	0.0229	0.0075	0.3286	0.0221	0.1306	0.5541	0.0000	0.0449
2017	Det16	0.0229	0.0075	0.3286	0.0221	0.1306	0.5541	0.0000	0.0449
2017	Det17	0.0237	0.0065	0.2729	0.0233	0.5761	5.6154	0.0001	0.0636
2017	Det18	0.0237	0.0065	0.2729	0.0233	0.5761	5.6154	0.0001	0.0636
2017	Det19	0.0237	0.0065	0.2730	0.0233	0.5688	5.5697	0.0001	0.0635
2017	Det20	0.0237	0.0065	0.2730	0.0233	0.5688	5.5697	0.0001	0.0635

(b) Year 2017: Det1–Det8 show excellent stability (CV ≤0.21) with negative skew. Det17–Det20 remain stable (CV ≈0.27). Det9–Det12 are variable (CV >0.45) with heavy tails (kurtosis >39). Det13–Det16 have moderate CV (≈0.33) and near-symmetric distributions.

Table A.5: Detector Statistics for Years 2018 and 2019

Year	Detector	Mean	Std dev	CV	Median	Skewness	Kurtosis	Min rate	Max rate
2018	Det1	0.0535	0.1252	2.3417	0.0284	6.2390	42.5273	0.0000	1.1371
2018	Det2	0.0535	0.1252	2.3417	0.0284	6.2390	42.5273	0.0000	1.1371
2018	Det3	0.0435	0.0837	1.9238	0.0284	7.1331	55.8178	0.0003	0.8228
2018	Det4	0.0435	0.0837	1.9238	0.0284	7.1331	55.8178	0.0003	0.8228
2018	Det5	0.0387	0.0467	1.2066	0.0354	9.6338	102.3461	0.0000	0.6168
2018	Det6	0.0387	0.0467	1.2066	0.0354	9.6338	102.3461	0.0000	0.6168
2018	Det7	0.0381	0.0440	1.1562	0.0353	9.6184	103.2124	0.0002	0.5867
2018	Det8	0.0381	0.0440	1.1562	0.0353	9.6184	103.2124	0.0002	0.5867
2018	Det9	0.0277	0.0151	0.5455	0.0281	5.1341	48.9538	0.0001	0.1745
2018	Det10	0.0277	0.0151	0.5455	0.0281	5.1341	48.9538	0.0001	0.1745
2018	Det11	0.0270	0.0106	0.3933	0.0281	0.0579	0.5013	0.0000	0.0645
2018	Det12	0.0270	0.0106	0.3933	0.0281	0.0579	0.5013	0.0000	0.0645
2018	Det13	0.0310	0.0675	2.1785	0.0250	11.8687	157.7211	0.0003	1.0369
2018	Det14	0.0310	0.0675	2.1785	0.0250	11.8687	157.7211	0.0003	1.0369
2018	Det15	0.0301	0.0575	1.9099	0.0250	11.9614	163.4858	0.0003	0.9013
2018	Det16	0.0301	0.0575	1.9099	0.0250	11.9614	163.4858	0.0003	0.9013
2018	Det17	0.0434	0.2334	5.3741	0.0255	15.5533	253.6684	0.0001	4.0423
2018	Det18	0.0434	0.2334	5.3741	0.0255	15.5533	253.6684	0.0001	4.0423
2018	Det19	0.0428	0.2332	5.4460	0.0254	15.6090	254.9593	0.0001	4.0426
2018	Det20	0.0428	0.2332	5.4460	0.0254	15.6090	254.9593	0.0001	4.0426

(a) Year 2018: Det1–Det4 and Det13–Det16 show high variability (CV >1.9), indicating unstable readings. Det5–Det8 are moderately unstable (CV ≈1.15–1.21). Det9–Det12 have moderate stability (CV ≈0.39–0.55). Det17–Det20 exhibit extreme fluctuations (CV >5.3) with heavy tails (kurtosis >250), suggesting rare but large bursts.

Year	Detector	Mean	Std dev	CV	Median	Skewness	Kurtosis	Min rate	Max rate
2019	Det1	0.1346	0.7752	5.7578	0.0257	9.3985	99.2938	0.0000	10.0741
2019	Det2	0.1346	0.7752	5.7578	0.0257	9.3985	99.2938	0.0000	10.0741
2019	Det3	0.1270	0.7245	5.7057	0.0258	9.6981	106.9470	0.0000	9.6792
2019	Det4	0.1270	0.7245	5.7057	0.0258	9.6981	106.9470	0.0000	9.6792
2019	Det5	0.0324	0.0123	0.3801	0.0333	3.9593	45.4984	0.0001	0.1613
2019	Det6	0.0324	0.0123	0.3801	0.0333	3.9593	45.4984	0.0001	0.1613
2019	Det7	0.0321	0.0107	0.3323	0.0332	0.6726	10.9923	0.0000	0.1095
2019	Det8	0.0321	0.0107	0.3323	0.0332	0.6726	10.9923	0.0000	0.1095
2019	Det9	0.0211	0.0199	0.9437	0.0180	5.0251	40.5443	0.0002	0.1946
2019	Det10	0.0211	0.0199	0.9437	0.0180	5.0251	40.5443	0.0002	0.1946
2019	Det11	0.0200	0.0158	0.7899	0.0179	2.1381	10.2706	0.0000	0.1199
2019	Det12	0.0200	0.0158	0.7899	0.0179	2.1381	10.2706	0.0000	0.1199
2019	Det13	0.0312	0.1064	3.4066	0.0227	17.2203	300.5320	0.0000	1.9054
2019	Det14	0.0312	0.1064	3.4066	0.0227	17.2203	300.5320	0.0000	1.9054
2019	Det15	0.0281	0.0545	1.9369	0.0228	15.9816	270.1776	0.0000	0.9623
2019	Det16	0.0281	0.0545	1.9369	0.0228	15.9816	270.1776	0.0000	0.9623
2019	Det17	0.0266	0.0449	1.6907	0.0243	15.4057	252.6127	0.0001	0.7781
2019	Det18	0.0266	0.0449	1.6907	0.0243	15.4057	252.6127	0.0001	0.7781
2019	Det19	0.0257	0.0435	1.6949	0.0242	16.7219	286.4066	0.0000	0.7781
2019	Det20	0.0257	0.0435	1.6949	0.0242	16.7219	286.4066	0.0000	0.7781

(b) Year 2019: Det1–Det4 are highly unstable (CV ≈5.7). Det5–Det8 show good stability (CV ≈0.33–0.38). Det9–Det12 moderate instability (CV ≈0.79–0.94). Det13–Det16 and Det17–Det20 exhibit high variability (CV >1.6) with heavy tails, indicating irregular spikes or rare bursts.

Table A.6: Detector Statistics for Year 2020

Year	Detector	Mean	Std dev	CV	Median	Skewness	Kurtosis	Min rate	Max rate
2020	Det1	0.0238	0.0083	0.3483	0.0247	0.2205	9.0739	0.0008	0.0836
2020	Det2	0.0238	0.0083	0.3483	0.0247	0.2205	9.0739	0.0008	0.0836
2020	Det3	0.0236	0.0083	0.3513	0.0247	0.0601	8.1061	0.0000	0.0817
2020	Det4	0.0236	0.0083	0.3513	0.0247	0.0601	8.1061	0.0000	0.0817
2020	Det5	0.0369	0.0345	0.9331	0.0354	7.4975	62.6346	0.0001	0.3762
2020	Det6	0.0369	0.0344	0.9315	0.0354	7.4900	62.5240	0.0001	0.3750
2020	Det7	0.0367	0.0339	0.9252	0.0354	7.5268	63.1705	0.0001	0.3719
2020	Det8	0.0367	0.0339	0.9253	0.0354	7.5271	63.1730	0.0001	0.3719
2020	Det9	0.0270	0.0108	0.4012	0.0285	−0.5762	1.2174	0.0010	0.0645
2020	Det10	0.0270	0.0108	0.4011	0.0285	−0.5790	1.2096	0.0010	0.0644
2020	Det11	0.0267	0.0107	0.4005	0.0284	−0.6412	1.0704	0.0010	0.0633
2020	Det12	0.0267	0.0107	0.4005	0.0284	−0.6405	1.0723	0.0010	0.0634
2020	Det13	0.0531	0.0775	1.4579	0.0279	2.9316	8.0525	0.0001	0.4286
2020	Det14	0.0531	0.0775	1.4577	0.0279	2.9317	8.0547	0.0001	0.4285
2020	Det15	0.0499	0.0737	1.4766	0.0276	3.1512	9.5958	0.0000	0.4255
2020	Det16	0.0499	0.0737	1.4766	0.0276	3.1512	9.5956	0.0000	0.4255
2020	Det17	0.0268	0.0330	1.2333	0.0225	8.4325	82.9517	0.0009	0.3904
2020	Det18	0.0268	0.0330	1.2333	0.0225	8.4325	82.9517	0.0009	0.3904
2020	Det19	0.0267	0.0330	1.2380	0.0225	8.4354	82.9781	0.0009	0.3904
2020	Det20	0.0267	0.0330	1.2380	0.0225	8.4354	82.9781	0.0009	0.3904
2020	Det21	0.0169	0.0260	1.5432	0.0074	2.4948	5.0206	0.0000	0.1078
2020	Det22	0.0169	0.0260	1.5432	0.0074	2.4948	5.0206	0.0000	0.1078
2020	Det23	0.0169	0.0260	1.5432	0.0074	2.4948	5.0206	0.0000	0.1078
2020	Det24	0.0169	0.0260	1.5432	0.0074	2.4948	5.0206	0.0000	0.1078
2020	Det33	0.0129	0.0171	1.3282	0.0067	2.4203	4.6079	0.0004	0.0685
2020	Det34	0.0129	0.0171	1.3282	0.0067	2.4203	4.6079	0.0004	0.0685
2020	Det35	0.0129	0.0171	1.3282	0.0067	2.4203	4.6079	0.0004	0.0685
2020	Det36	0.0129	0.0171	1.3282	0.0067	2.4203	4.6079	0.0004	0.0685
2020	Det37	0.0218	0.0384	1.7569	0.0072	2.5017	5.0487	0.0000	0.1589
2020	Det38	0.0218	0.0384	1.7569	0.0072	2.5017	5.0487	0.0000	0.1589
2020	Det39	0.0218	0.0384	1.7569	0.0072	2.5017	5.0487	0.0000	0.1589
2020	Det40	0.0218	0.0384	1.7569	0.0072	2.5017	5.0487	0.0000	0.1589

(a) Year 2020: Det1–Det4 exhibit moderate stability (CV ≈0.35). Det9–Det12 are similarly stable (CV ≈0.40) but slightly negatively skewed. Det5–Det8 show high variability (CV ≈0.93) with frequent outliers. Det13–Det16 and Det17–Det20 have CVs >1.2, indicating unstable measurements. The downstream detectors (Det21–Det24, Det33–Det36, Det37–Det40) show even higher CVs (1.33–1.76), reflecting significant variability and occasional extreme bursts.

Table A.7: Detector Statistics for Year 2021

Year	Detector	Mean	Std dev	CV	Median	Skewness	Kurtosis	Min rate	Max rate
2021	Det5	0.0348	0.0128	0.3675	0.0345	3.2773	26.4993	0.0021	0.1389
2021	Det6	0.0347	0.0128	0.3670	0.0345	3.2557	26.2773	0.0021	0.1384
2021	Det7	0.0347	0.0126	0.3622	0.0345	3.0674	24.4159	0.0021	0.1345
2021	Det8	0.0347	0.0126	0.3622	0.0345	3.0681	24.4245	0.0021	0.1346
2021	Det13	0.0315	0.0385	1.2222	0.0241	5.5058	30.8182	0.0000	0.2967
2021	Det14	0.0315	0.0385	1.2209	0.0241	5.5054	30.8223	0.0000	0.2966
2021	Det15	0.0310	0.0345	1.1154	0.0242	5.4662	30.9250	0.0013	0.2762
2021	Det16	0.0310	0.0345	1.1154	0.0242	5.4665	30.9283	0.0013	0.2762
2021	Det17	0.0251	0.0211	0.8410	0.0246	11.7758	151.8398	0.0000	0.3007
2021	Det18	0.0251	0.0211	0.8410	0.0246	11.7758	151.8398	0.0000	0.3007
2021	Det19	0.0253	0.0211	0.8343	0.0247	11.8626	152.9560	0.0016	0.3002
2021	Det20	0.0253	0.0211	0.8343	0.0247	11.8626	152.9560	0.0016	0.3002
2021	Det21	0.0166	0.0302	1.8197	0.0014	2.1052	3.3164	0.0000	0.1116
2021	Det22	0.0166	0.0302	1.8197	0.0014	2.1052	3.3164	0.0000	0.1116
2021	Det23	0.0166	0.0302	1.8197	0.0014	2.1052	3.3164	0.0000	0.1116
2021	Det24	0.0166	0.0302	1.8197	0.0014	2.1052	3.3164	0.0000	0.1116
2021	Det25	0.0210	0.0325	1.5455	0.0150	2.6864	5.8830	0.0000	0.1312
2021	Det26	0.0210	0.0325	1.5455	0.0150	2.6864	5.8830	0.0000	0.1312
2021	Det27	0.0210	0.0325	1.5455	0.0150	2.6864	5.8830	0.0000	0.1312
2021	Det28	0.0210	0.0325	1.5455	0.0150	2.6864	5.8830	0.0000	0.1312
2021	Det29	0.0686	0.0504	0.7352	0.0829	−0.3330	−1.6397	0.0000	0.1210
2021	Det30	0.0686	0.0504	0.7352	0.0829	−0.3330	−1.6397	0.0000	0.1210
2021	Det31	0.0686	0.0504	0.7352	0.0829	−0.3330	−1.6397	0.0000	0.1210
2021	Det32	0.0686	0.0504	0.7352	0.0829	−0.3330	−1.6397	0.0000	0.1210
2021	Det33	0.0384	0.0455	1.1840	0.0111	1.1768	−0.2894	0.0000	0.1341
2021	Det34	0.0384	0.0455	1.1840	0.0111	1.1768	−0.2894	0.0000	0.1341
2021	Det35	0.0384	0.0455	1.1840	0.0111	1.1768	−0.2894	0.0000	0.1341
2021	Det36	0.0384	0.0455	1.1840	0.0111	1.1768	−0.2894	0.0000	0.1341
2021	Det37	0.1138	0.0819	0.7198	0.1605	−0.3295	−1.6967	0.0001	0.2028
2021	Det38	0.1138	0.0819	0.7198	0.1605	−0.3295	−1.6967	0.0001	0.2028
2021	Det39	0.1138	0.0819	0.7198	0.1605	−0.3295	−1.6967	0.0001	0.2028
2021	Det40	0.1138	0.0819	0.7198	0.1605	−0.3295	−1.6967	0.0001	0.2028

(a) Year 2021: Det5–Det8 show moderate stability (CV ≈0.36). Det13–Det16 and Det17–Det20 exhibit moderate to high variability (CV >0.83), with Det17–20 showing heavy tails (kurtosis >150). Det21–Det28 are highly variable (CV >1.5). Det29–Det32 are relatively stable (CV ≈0.74) with negative skew. Det33–Det36 and Det37–Det40 show mixed stability (CV ≈0.72–1.18) and near-symmetric distributions.

To produce table A.8, each shower event was first inspected to determine its lateral distribution of particle densities around the reconstructed core. A standard NKG profile (with fixed age) was fitted to these densities, and any fit that converged on the minimum or maximum allowed Molière radius was marked as "hit boundary." In parallel, the distance from the core to the nearest triggered detector was measured, and events with distances less than 10 m were flagged as "core too close." Finally, the events were grouped by year and by the months of May and November, and for each period the total event count, the percentage of boundary hit fits, and the percentage of core too close cases were computed to generate the summary table.

Table A.8: Summary of NKG Fit Outcomes by Year and Month. The table lists the total number of events used in each period, the fraction of fits that hit parameter boundaries, and the fraction with reconstructed cores located within 10 m of a detector. Periods with no data are indicated by "–".

Year	Month	Total Events	% Hit Boundary	% Core < 10m
2011	May	161	24.8%	13.0%
2011	Nov	427	25.1%	10.3%
2012	May	924	22.7%	11.5%
2012	Nov	3863	19.4%	11.6%
2013	May	3299	21.1%	10.8%
2013	Nov	3579	20.4%	11.3%
2014	May	2633	19.4%	11.0%
2014	Nov	3481	19.4%	10.9%
2015	May	1031	20.6%	10.8%
2015	Nov	1602	22.2%	9.8%
2016	May	2340	17.4%	12.6%
2016	Nov	3186	20.8%	10.0%
2017	May	2818	22.6%	10.6%
2017	Nov	–	–	–
2018	May	1230	20.2%	10.1%
2018	Nov	746	23.5%	9.9%
2019	May	2262	23.3%	10.3%
2019	Nov	1663	22.9%	11.3%
2020	May	614	37.9%	9.6%
2020	Nov	1554	34.5%	10.6%
2021	May	763	22.9%	11.1%
2021	Nov	768	47.7%	17.8%

B - Appendix

Figure B.1: Structure of the *Tree_event* in the old ROOT data format. Each detector (Det1 to Det20) is represented as a separate branch containing subfields such as GPS timestamps and detector-specific measurements.[38]

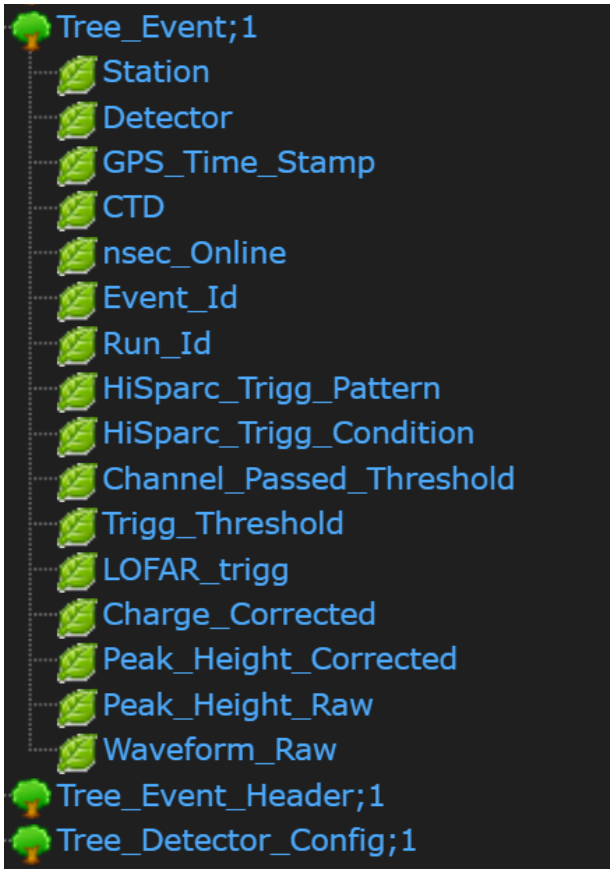

Figure B.2: Structure of the *Tree_Event* in the new ROOT data format.Unlike the old ROOT structure, the new ROOT structure does not comprise of Det1, Det2,...Det20.

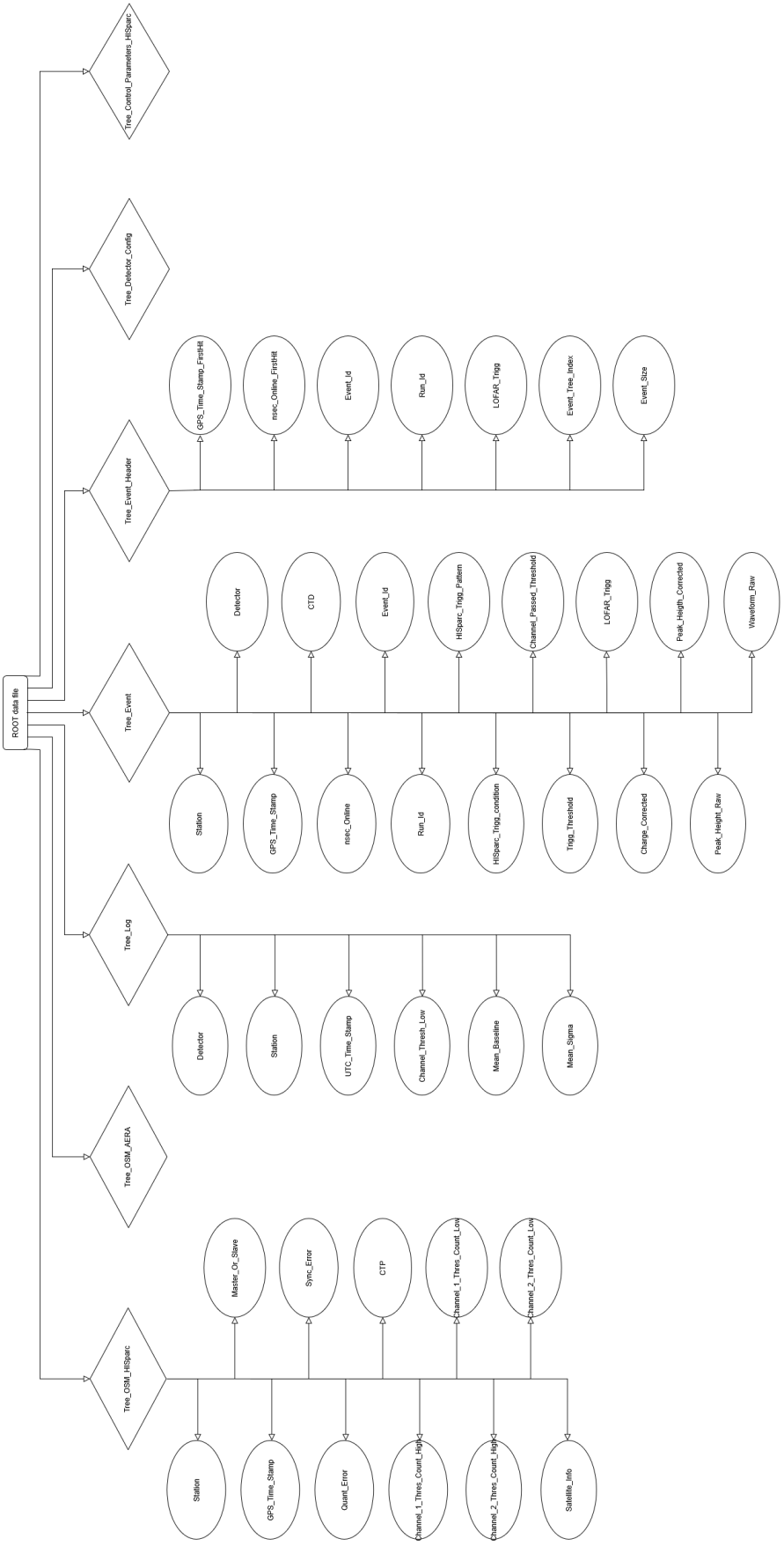

Figure B.3: ROOT file structure of raw LORA files. This figure was created by Lucas van Dongen from Radboud University, Netherlands, for his master's thesis.

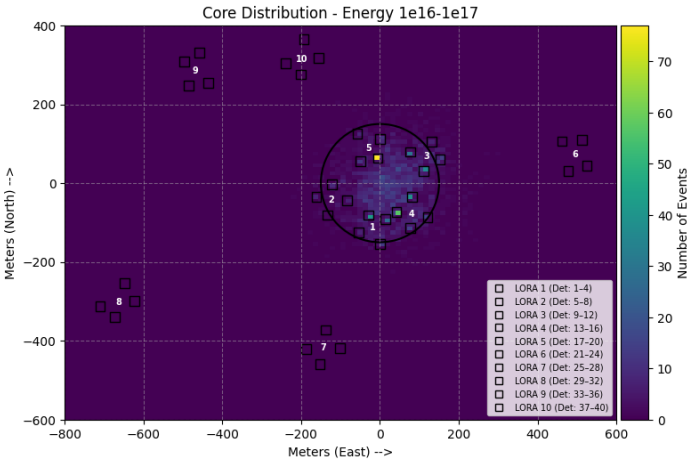

(a) $10^{16} \leq E < 10^{17}$ eV

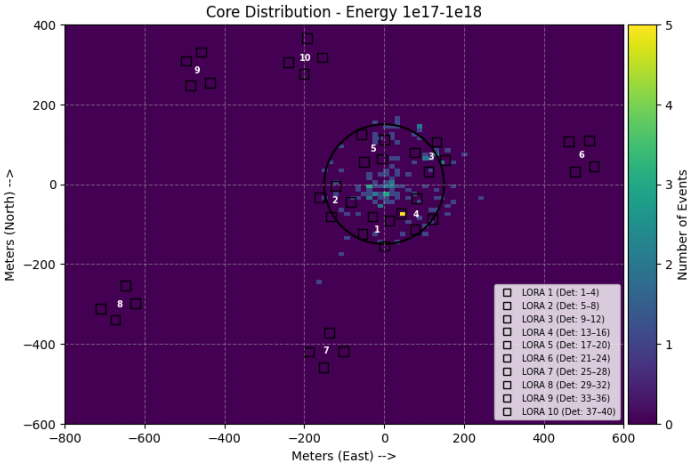

(b) $10^{17} \leq E < 10^{18}$ eV

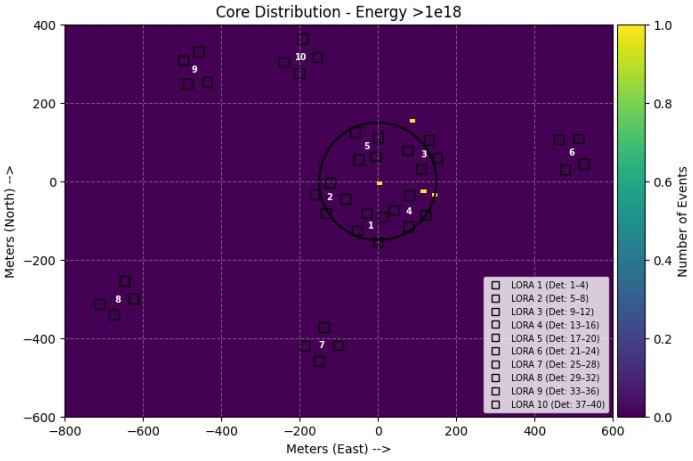

(c) $E \geq 10^{18}$ eV

Figure B.4: Core location distributions of May 2013 for higher energy bins: $10^{16} \leq E < 10^{17}$ eV, $10^{17} \leq E < 10^{18}$ eV, and $E \geq 10^{18}$ eV. Each square denotes a detector and four detectors comprise of one station denoted by LORAX, wher x = 1,2,...,10. The black circle in the centre in the fiducial radius of 150m. One can observe a significant decrease of events in highest energies.

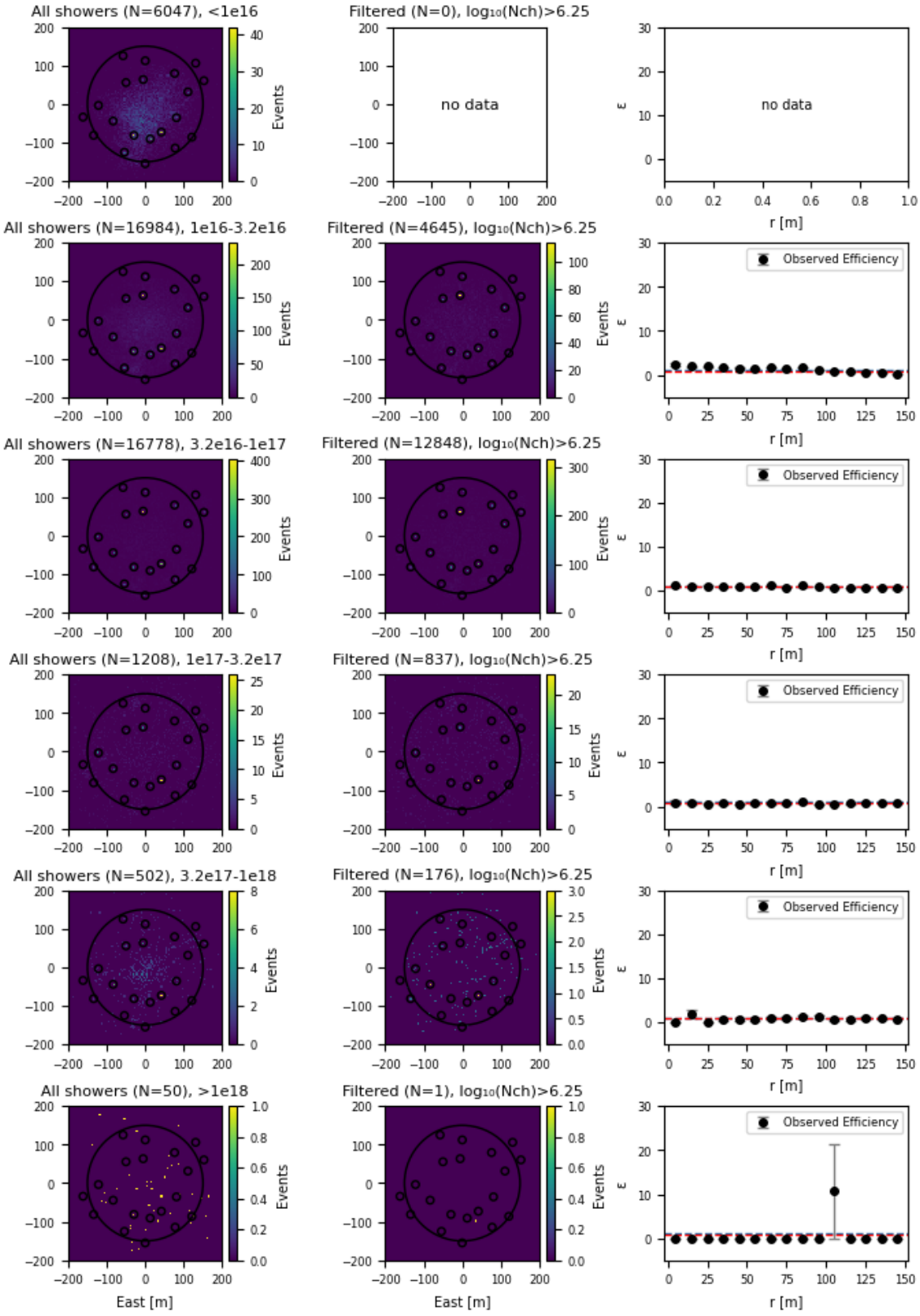

Figure B.5: Each row corresponds to a different primary energy bin. The first two columns denote all showers and the showers that pass the cut, respectively, as discussed in figure 5.2. The third column interprets radial detection efficiency $\varepsilon(r)$ as a function of core distance $r = \sqrt{x^2 + y^2}$, with Poisson-error bars and 90% efficiency threshold (red dashed line).

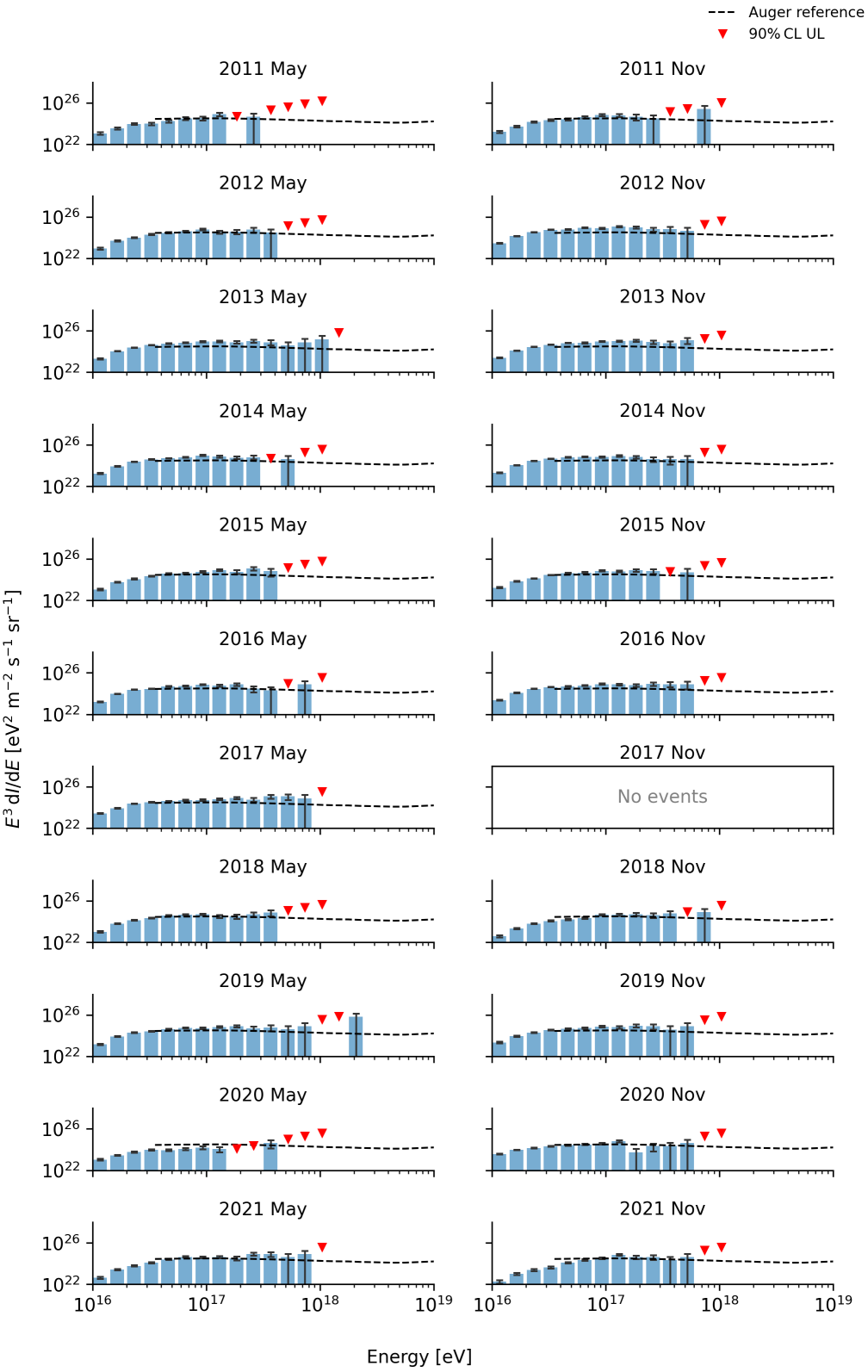

Figure B.6: Measured cosmic-ray energy spectrum $E^3\,\mathrm{d}I/\mathrm{d}E$ as a function of energy [eV], using LORA data for May (left) and November (right), aggregated over 11 years. Histogram bars are corrected for detector acceptance and live time. Error bars represent statistical uncertainties. Red downward triangles denote 90% confidence level upper limits for energy bins with zero observed events. The dashed black line shows the Pierre Auger reference spectrum for comparison.

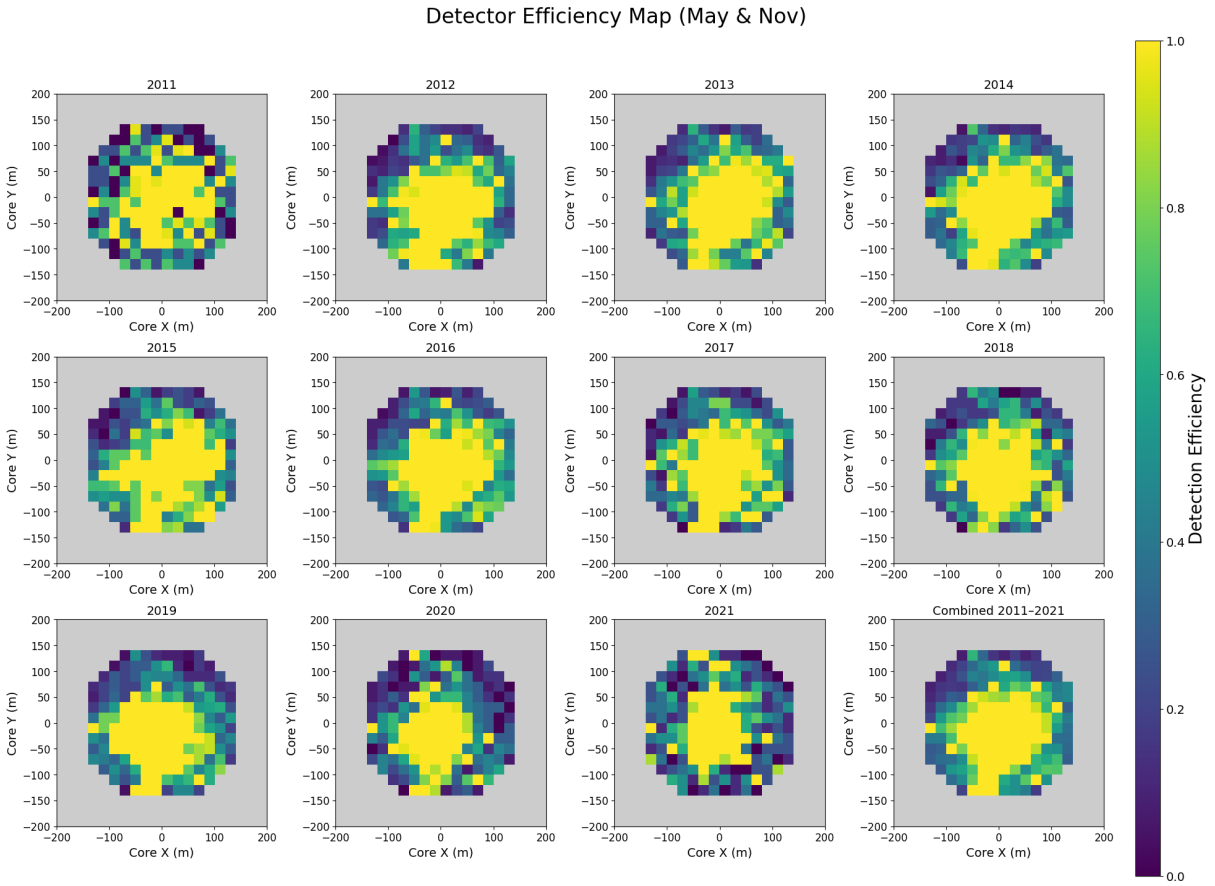

Figure B.7: Detection efficiency map within a 150 m fiducial radius, computed on a 20 m × 20 m grid using core positions from May and November over 2011–2021, shown without event quality cuts. In this case, lower-efficiency regions appear near the edges due to marginally triggered or poorly reconstructed events. After applying quality cuts ($\log_{10}(N_{ch}) > 6.25$, $10 \leq r_M \leq 200$ m), the efficiency distribution becomes more uniform, and the core positions are more spread out as shown in figure 5.8. This is because the cuts preferentially select higher-energy events, which can be reliably reconstructed even at larger distances from the array center.

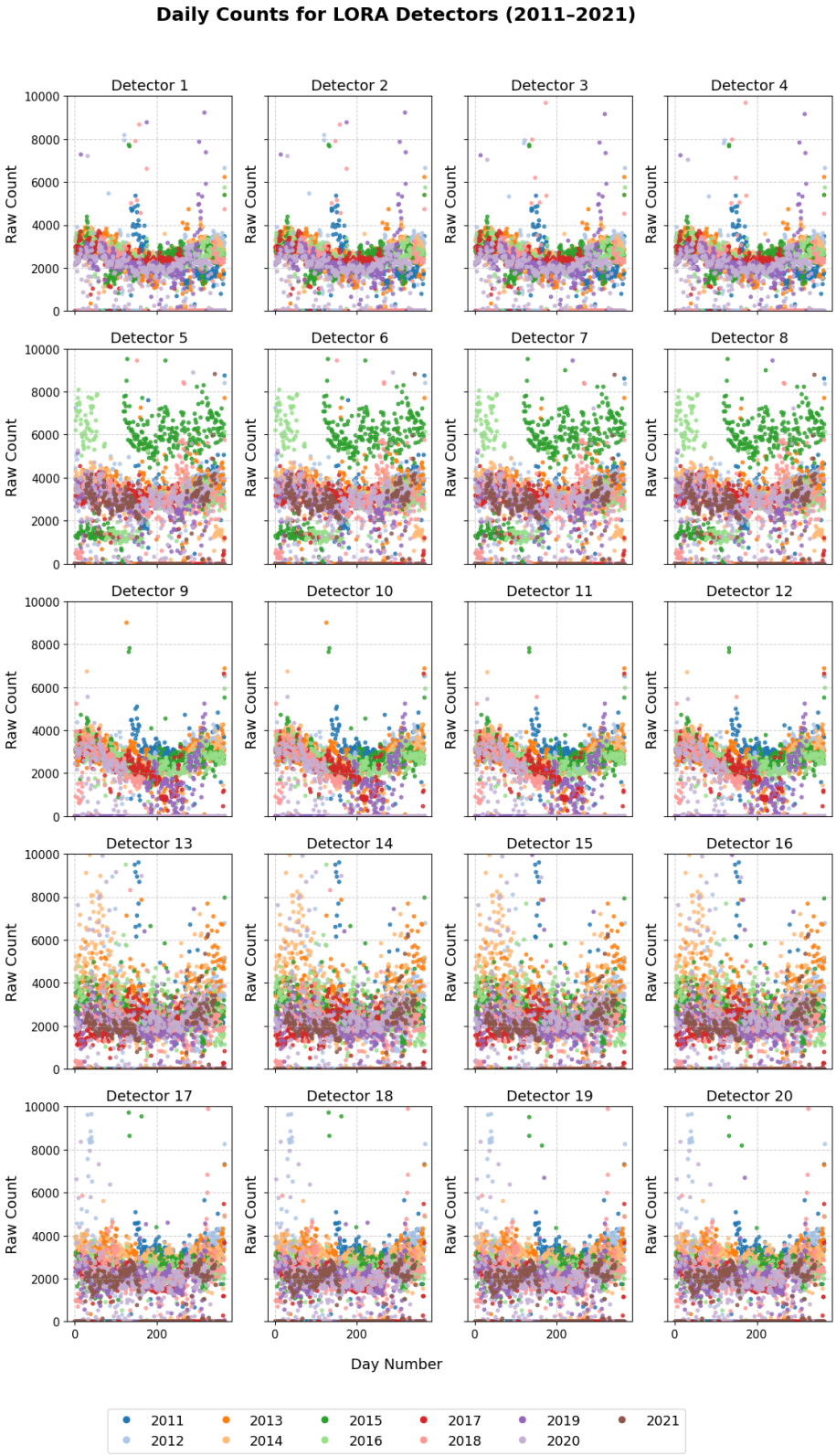

Figure B.8: Daily raw counts for 20 LORA detectors over the period 2011–2021, plotted as individual scatter points for each calendar day of each year. Despite the scatter, a parabolic trend emerges with count rates being elevated at the beginning and end of the year and reach a minimum around mid year. This reflects rise in atmospheric temperature and amplifier heating during summers.

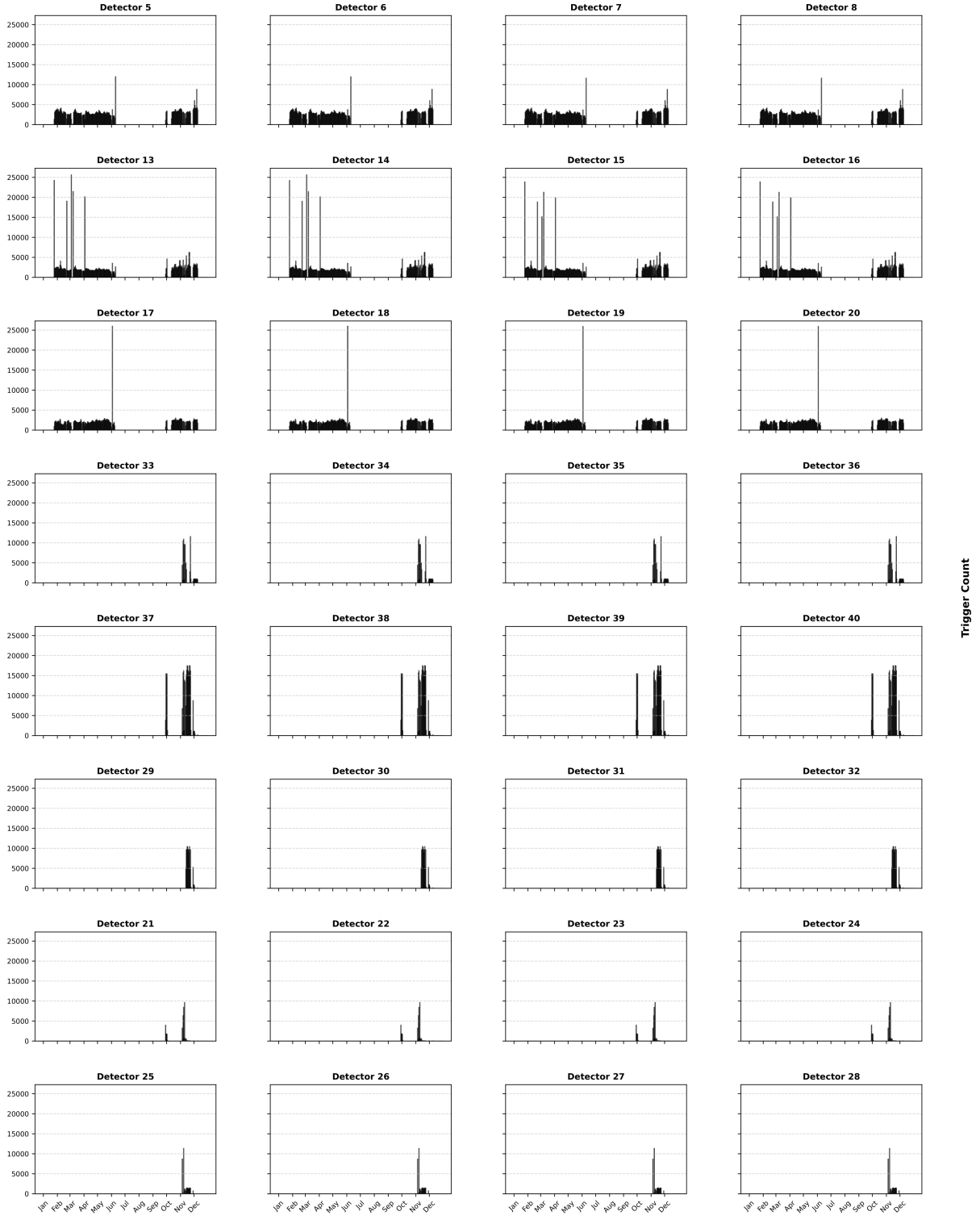

Figure B.9: Daily trigger count histograms for Detectors the LORA array for the year 2021. Each subplot corresponds to a single detector and shows the number of triggers recorded per day throughout the year. The x-axis represents time in months (January to December), while the y-axis indicates the daily trigger count. Detectors that did not record any data during the year do not appear in the plot. This visualization aids in diagnosing operational stability, identifying potential outliers.

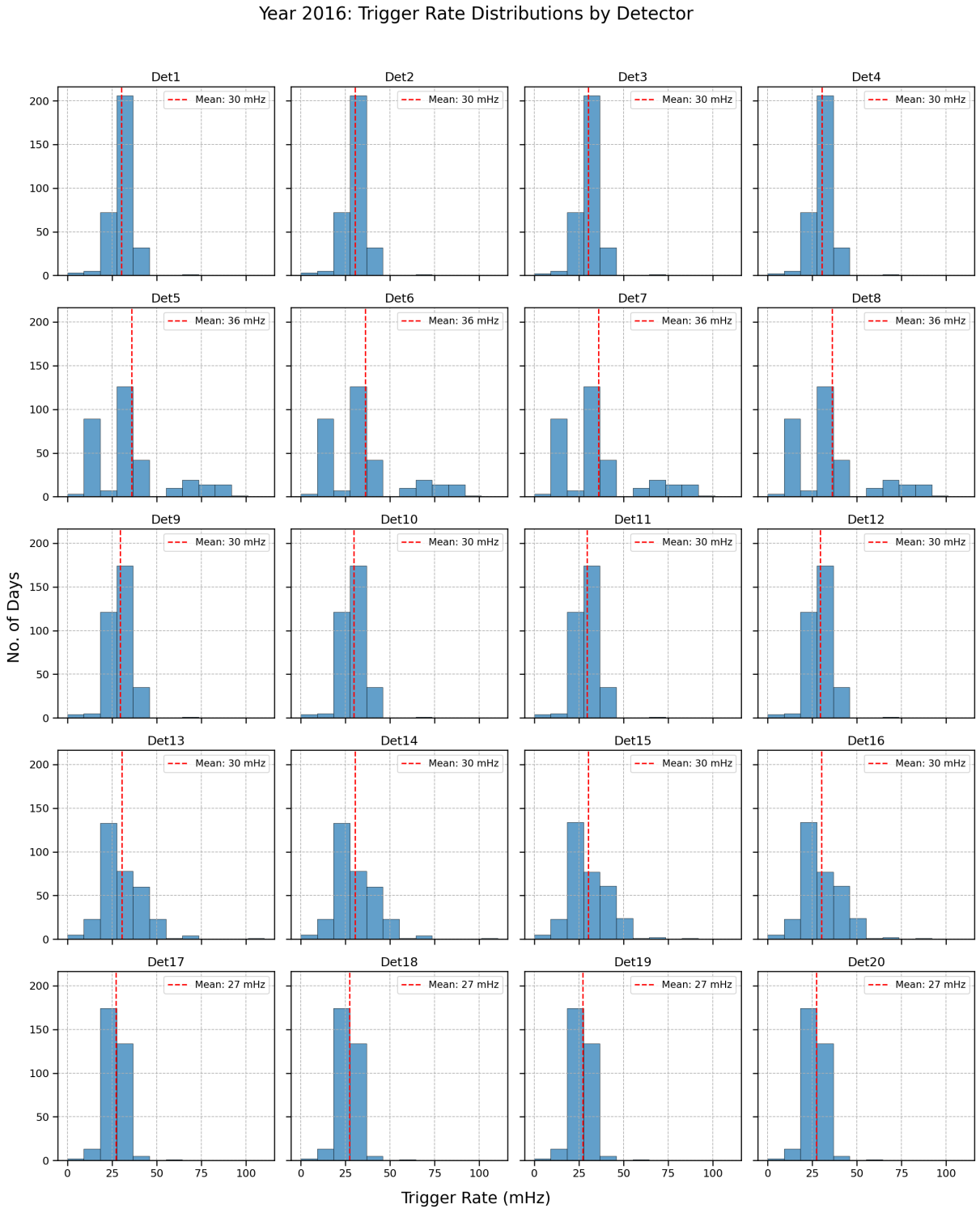

Figure B.10: Daily trigger rate distributions for LORA Detectors 1–20 during the year 2016. In each of the 20 panels, the blue bars represent the number of days with a given trigger rate and the red dashed line indicates the mean daily trigger rate for that detector. Mean rate for each detector is marked in their respective legends (in mHz). Most detectors exhibit tight, Gaussian-like distributions demonstrating stable performance throughout the mid-decade period. Detectors 5–8 show slightly broader distributions and marginally higher means, hinting at minor threshold shifts or environmental variations, but no sustained irregularities are observed across the array.

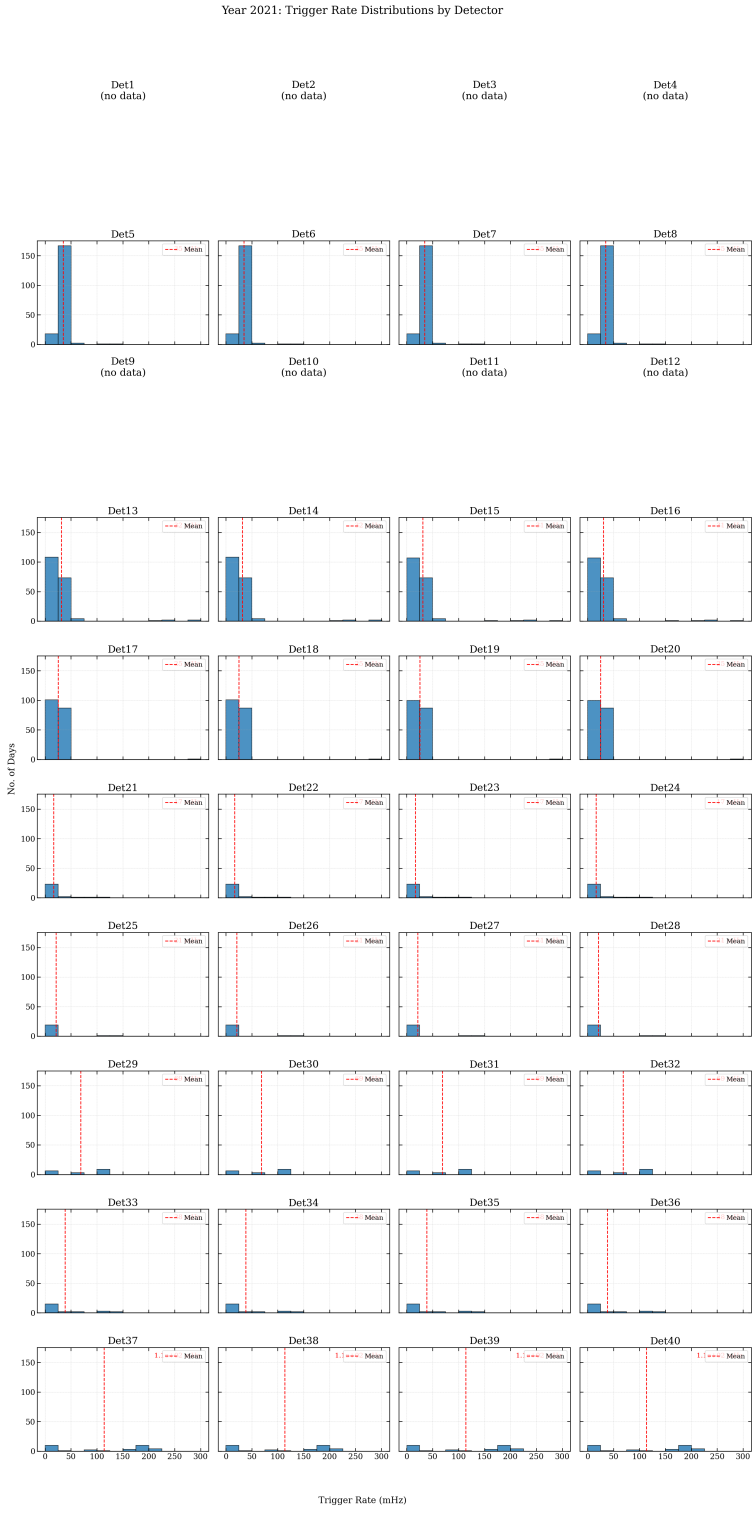

Figure B.11: Daily trigger rate distributions for each of the 40 LORA detectors during 2021. Histograms are arranged in detector order (Det 1–Det 40), with the red dashed line in each panel indicating the mean trigger rate. Empty panels (Det 1–4, Det 9–12) denote detectors with no recorded triggers. Compared to 2011, many detectors now exhibit broader, asymmetric rate distributions and intermittent operation, reflecting long-term hardware aging and varying environmental/threshold conditions. A subset of detectors (e.g., Det 6–8, Det 13–20) continue to demonstrate relatively stable performance despite the overall decline in uniformity.

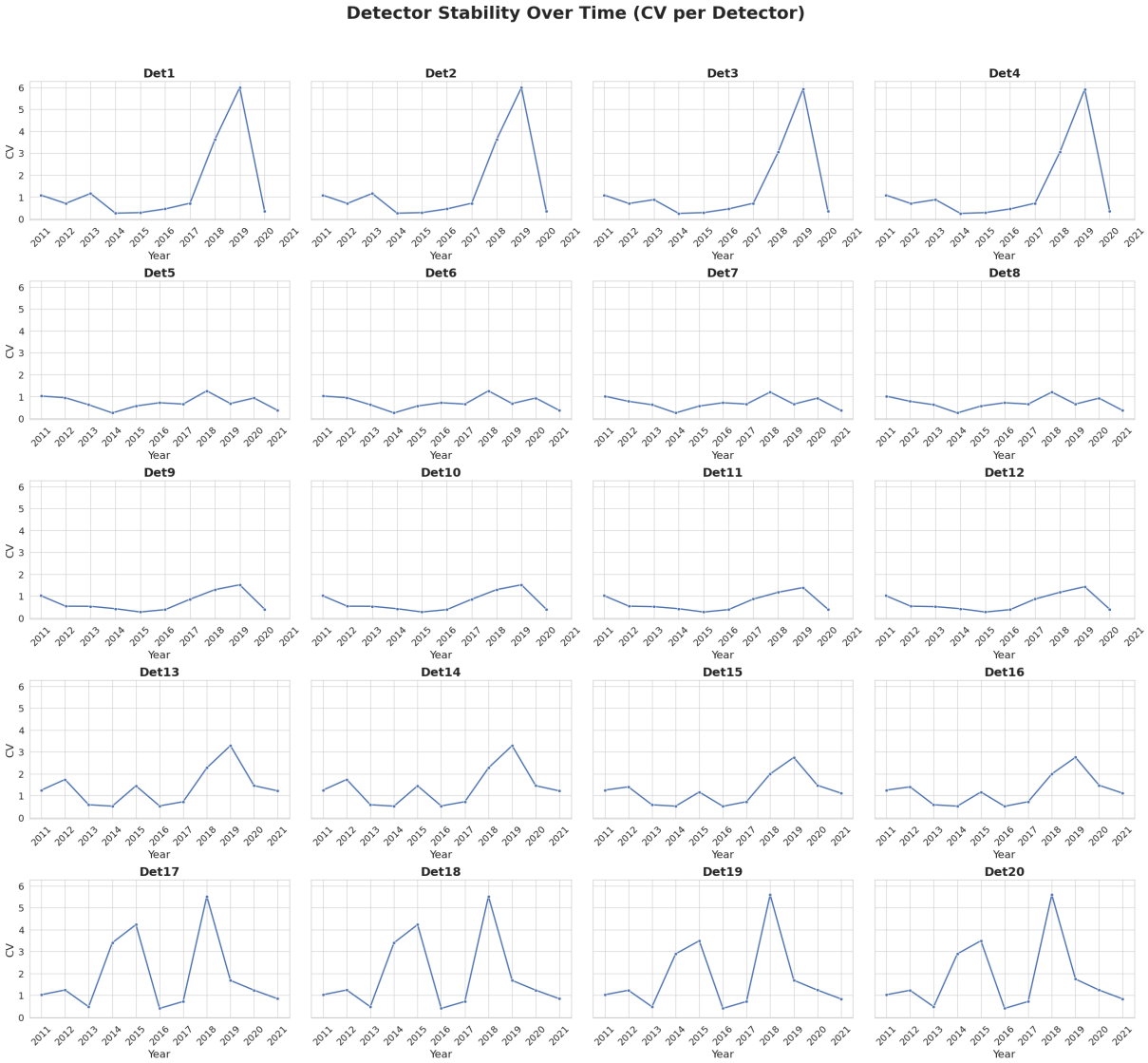

Figure B.12: Coefficient of variation (CV) trends from 2011 to 2021 for individual LORA detectors (Det1–Det20). Each subplot displays the yearly CV for a specific detector, illustrating its signal stability over time.

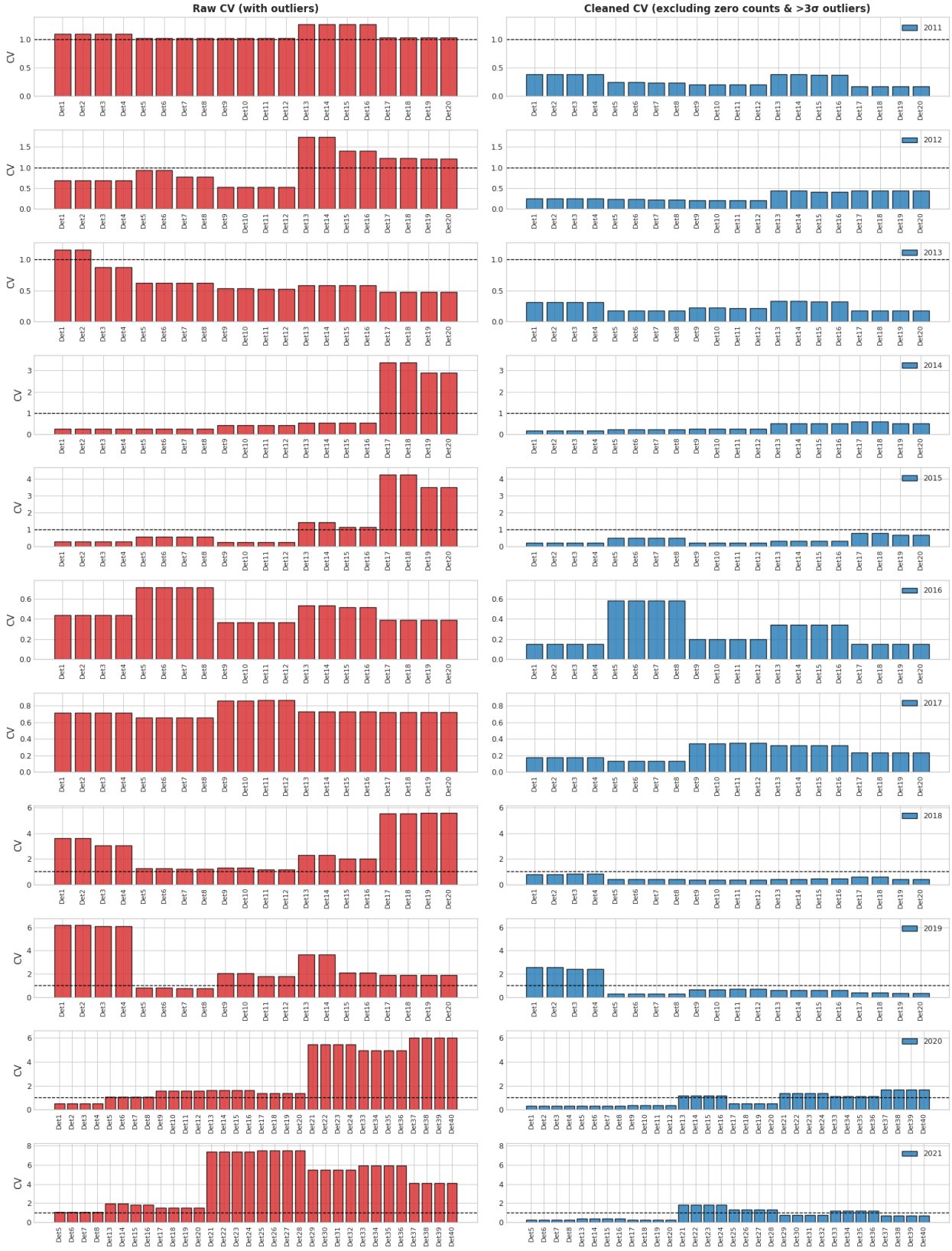

Figure B.13: Coefficient of variation (CV) of detector count rates are plotted against detector IDs. Each row represents the CV values for one year ranging from 2011-2021. The left panels (red) show raw CV values including outliers, while the right panels (blue) display CV values after excluding zero-count days and $> 3\sigma$ outliers. Horizontal dashed lines indicate the reference CV = 1 threshold.

Bibliography

[1] A. De Angelis and M. Pimenta, *Introduction to Particle and Astroparticle Physics*, Undergraduate Lecture Notes in Physics. Springer, 2018, 10.1007/978-3-319-78181-5.

[2] C. Glaser, A. Nelles, I. Plaisier et al., *NuRadioReco: A reconstruction framework for radio neutrino detectors*, *The European Physical Journal C* **79** (2019) .

[3] K. Terveer, "Proceedings of the 39th international cosmic ray conference (icrc2025)." Preprint available at `https://pos.sissa.it/501/413/pdf`, not yet published, 2025.

[4] Square Kilometre Array Observatory, "SKAO – Square Kilometre Array Observatory." `https://www.skao.int/en`, 2025.

[5] K. Kotera and A. V. Olinto, *The astrophysics of ultrahigh-energy cosmic rays*, *Annual Review of Astronomy and Astrophysics* **49** (2011) 119–153.

[6] F. G. Schröder, *Radio detection of cosmic-ray air showers and high-energy neutrinos*, *Progress in Particle and Nuclear Physics* **93** (2017) 1.

[7] S. Navas, C. Amsler, T. Gutsche et al., *Review of particle physics*, *Phys. Rev. D* **110** (2024) 030001.

[8] A. W. Strong, I. V. Moskalenko and V. S. Ptuskin, *Cosmic-ray propagation and interactions in the galaxy*, *Annual Review of Nuclear and Particle Science* **57** (2007) 285–327.

[9] S. Fukui, H. Hasegawa and T. e. a. Matano, *A study on the structure of the extensive air shower*, *Progress of Theoretical Physics Supplement* **16** (1960) 1.

[10] P. K. F. Grieder, *Extensive Air Showers: High Energy Phenomena and Astrophysical Aspects: A Tutorial, Reference Manual and Data Book*. Springer, 2010.

[11] S. Kawanomoto, M. Koike, F. Bradfield et al., *Observing cosmic-ray extensive air showers with a silicon imaging detector*, *Scientific Reports* **13** (2023) 16091.

[12] J. Hubbell, *Electron–positron pair production by photons: A historical overview*, *Radiation Physics and Chemistry* **75** (2006) 614.

[13] A. Haungs, J. Blumer, B. Fuchs et al., *KCDC - the kascade cosmic-ray data centre*, *Journal of Physics: Conference Series* **632** (2015) .

[14] S. Thoudam, S. Buitink, A. Corstanje and et al., *Measurement of the cosmic-ray energy spectrum above* 10^{16} *eV with the LOFAR Radboud Air Shower Array*, *Astroparticle Physics* **73** (2016) 34–43.

[15] CERN, "Victor Hess discovers cosmic rays." https://timeline.web.cern.ch/victor-hess-discovers-cosmic-rays-0, 2012.

[16] The Pierre Auger Collaboration, "The Pierre Auger Observatory." https://www.auger.org/, 2024.

[17] T. Abu-Zayyad, R. Aida, M. Allen et al., *The surface detector array of the Telescope Array experiment*, *Nucl. Instrum. Meth. A* **689** (2012) 87.

[18] T. Antoni, W. D. Apel, F. Badea et al., *The cosmic-ray experiment KASCADE*, *Nucl. Instrum. Meth. A* **513** (2003) 490.

[19] E. Atkin, V. Bulatov, V. Dorokhov et al., *The NUCLEON experiment. results of the first year of data acquisition*, *Astroparticle Physics* **90** (2017) 69.

[20] M. Amenomori, X. J. Bi, D. Chen et al., *The all-particle spectrum of primary cosmic rays in the wide energy range from* 10^{14} *eV to* 10^{17} *eV observed with the Tibet-III air-shower array*, *Astrophys. J.* **678** (2008) 1165.

[21] A. U. Abeysekara, A. Albert, R. Alfaro et al., *Observation of the Crab Nebula with the HAWC Gamma-Ray Observatory*, *Astrophys. J.* **843** (2017) 39.

[22] M. G. Aartsen, M. Ackermann, J. Adams et al., *The IceCube Neutrino Observatory: Instrumentation and Online Systems*, *JINST* **12** (2017) P03012.

[23] N. Budnev, I. Astapov, N. Barbashina et al., *The TAIGA experiment: From cosmic-ray to gamma-ray astronomy in the Tunka valley*, *Nucl. Instrum. Meth. A* **845** (2017) 330.

[24] W. D. Apel, J. C. Arteaga, A. F. Badea et al., *The KASCADE-Grande experiment*, *Nucl. Instrum. Meth. A* **620** (2010) 202.

[25] A. D. Supanitsky, *Determination of the cosmic-ray chemical composition: Open issues and prospects*, *Galaxies* **10** (2022) .

[26] C. Evoli, *The cosmic-ray energy spectrum*, Dec., 2020. 10.5281/zenodo.4396125.

[27] T. K. Gaisser, R. Engel and E. Resconi, *Cosmic Rays and Particle Physics*. Cambridge University Press, 2 ed., 2016.

[28] S. Recchia and S. Gabici, *Origin of the spectral features observed in the cosmic-ray spectrum*, *Astronomy amp; Astrophysics* **692** (2024) A20.

[29] CERN, "The Large Hadron Collider." https://home.cern/science/accelerators/large-hadron-collider, 2025.

[30] ASTRON, "Key science projects of LOFAR." https://science.astron.nl/telescopes/lofar/science-with-lofar/key-science-projects/, 2025.

[31] P. Schellart, A. Nelles, S. Buitink et al., *Detecting cosmic rays with the LOFAR radio telescope*, *Astronomy amp; Astrophysics* **560** (2013) A98.

[32] P. Schellart, S. Buitink, A. Corstanje et al., *Polarized radio emission from extensive air showers measured with LOFAR*, *Journal of Cosmology and Astroparticle Physics* **2014** (2014) 014–014.

[33] M. Haarlem, *LOFAR: The Low Frequency Array*, *EAS Publications Series* **15** (2005) 431 .

[34] K. Mulrey et al., *Extension of the LOFAR Radboud Air Shower Array*, *PoS* **ICRC2019** (2020) 363.

[35] S. Thoudam, S. Buitink, A. Corstanje et al., *LORA: A scintillator array for LOFAR to measure extensive air showers*, *Nuclear Instruments and Methods in Physics Research Section A: Accelerators, Spectrometers, Detectors and Associated Equipment* **767** (2014) 339–346.

[36] R. Brun and F. Rademakers, *ROOT — an object oriented data analysis framework*, *Nuclear Instruments and Methods in Physics Research Section A: Accelerators, Spectrometers, Detectors and Associated Equipment* **389** (1997) 81.

[37] S. Oosthoek, "Hardware servers." https://cncz.science.ru.nl/en/howto/hardware-servers/, Aug., 2025.

[38] S. Linev, "JavaScript ROOT." https://root.cern/js/, 2015.

[39] LOFAR CR Collaboration, "Lofar Cosmic Ray Project." Private communication, repository accessible only to collaborators. Accessed: 2025-08-30.

[40] NuRadio-Collaboration, "NuRadioMC: A monte carlo simulation package for radio neutrino detectors." https://github.com/nu-radio/NuRadioMC/tree/develop, 2025.

[41] S. Sharma, "Stability-lora-array-2011-2021." https://github.com/stuti0sharma/Stability-LORA-array-2011-2021, 2025.

[42] F. Fenu, *The cosmic ray energy spectrum measured with the Pierre Auger Observatory*, *Advances in Space Research* **72** (2023) 3531.